REVIEW ARTICLE

A Review of Transparent and Artificial Boundary Conditions Techniques for Linear and Nonlinear Schrödinger Equations

Xavier Antoine[1], Anton Arnold[2], Christophe Besse[3], Matthias Ehrhardt[4],[*] and Achim Schädle[5]

[1] *Institut Elie Cartan Nancy (IECN), Université Henri Poincaré Nancy 1, UMR 7502, INRIA Corida, Nancy-Université, France.*
[2] *Institut für Analysis und Scientific Computing, Technische Universität Wien, Wiedner Hauptstr. 8, 1040 Wien, Austria.*
[3] *Project-Team SIMPAF INRIA Lille Nord Europe Research Centre, Laboratoire Paul Painlevé U.M.R CNRS 8524*
Université des Sciences et Technologies de Lille, France.
[4] *Weierstrass Institute for Applied Analysis and Stochastics, Mohrenstr. 39, 10117 Berlin, Germany.*
[5] *Zuse-Institut Berlin, Takustrasse 7, 14195 Berlin, Germany.*

Abstract. In this review article we discuss different techniques to solve numerically the time-dependent Schrödinger equation on unbounded domains. We present in detail the most recent approaches and describe briefly alternative ideas pointing out the relations between these works. We conclude with several numerical examples from different application areas to compare the presented techniques. We mainly focus on the one-dimensional problem but also touch upon the situation in two space dimensions and the cubic nonlinear case.

---

[*]Corresponding author. *Email addresses:* `Xavier.Antoine@iecn.u-nancy.fr` (X. Antoine), `anton.arnold@tuwien.ac.at` (A. Arnold), `Christophe.Besse@math.univ-lille1.fr` (C. Besse), `ehrhardt@wias-berlin.de` (M. Ehrhardt), `schaedle@zib.de` (A. Schädle)

Contents

1   Introduction

The equation under consideration is the 1D Schrödinger equation

$$
\begin{aligned}
&i\partial_t u = -\partial_x^2 u + V(x,t)u, \quad x\in\mathcal{R}, \ t>0, \\
&\lim_{|x|\to\infty} u(x,t)=0, \\
&u(x,0)=u^I(x),
\end{aligned}
\tag{1.1}
$$

where V denotes a given real potential. We assume that the initial data is compactly supported, i.e., $\mathrm{supp}(u^I)\subset[x_l,x_r]$. Furthermore, we assume that V is constant outside an interval $[x_l,x_r]$, i.e., $V(x)=V_l$ for $x<x_l$, $V(x)=V_r$ for $x>x_r$ (t-dependent exterior potentials will be discussed in Remark 2.5).

Eq. (1.1) is one of the basic equations of quantum mechanics and it arises in many areas of physical and technological interest, e.g. in quantum semiconductors [28], in electromagnetic wave propagation [87], and in seismic migration [33]. The Schrödinger equation is also the lowest order one-way approximation (*paraxial wave equation*) to the Helmholtz equation and is called *Fresnel equation* in optics [112], or *standard parabolic equation* in underwater acoustics [129]. We will return to these applications in the numerical examples of Section 6.

The solution to (1.1) is defined on the unbounded domain $\Omega=\{(x,t)\in\mathcal{R}\times\mathcal{R}^+\}$. If one wants to solve such a whole space evolution problem numerically, one has to restrict the computational (interior) domain $\Omega_{int}=\{(x,t)\in]x_l,x_r[\times\mathcal{R}^+\}$ by introducing artificial boundary conditions or absorbing layers [81, 105]. Note that the method of "exterior complex scaling" [95] belongs also to this last mentioned class. Alternative methods are infinite element methods (IEM) [45].

We remark that in some cases the original whole space problem can be transformed into a differential equation on a finite domain. However, this *coordinate transform technique* is restricted to special cases and yields quite complicated differential equations. This

method was introduced by Grosch and Orszag in [66] and applied to the Schrödinger equation by Ladouceur in [83].

Artificial boundary conditions are constructed with the objective to approximate the exact solution of the whole-space problem, restricted to Ω_{int}. Such BCs are called *absorbing boundary conditions* (ABCs) if they yield a well-posed initial boundary value problem (IBVP), where some "energy" is absorbed at the boundary. If this approximate solution actually coincides on Ω_{int} with the exact solution of the whole-space problem, one refers to these BCs as *transparent boundary conditions* (TBCs). While TBCs for the Schrödinger equation are nonlocal in time (and space for multi-dimensional cases), it is often desirable to construct ABCs that are *local* in space and/or time to allow for an efficient numerical implementation [67,120,121].

In this review article we describe and compare different approaches of constructing and discretizing TBCs for the Schrödinger equation in 1D. There already exists a couple of review articles concerning transparent boundary conditions, e.g. Givoli [62–64], Hagstrom [67], Tsynkov [130]. But to the authors knowledge there is only one short comparison paper by Yevick, Friese, and Schmidt [131] on the Schrödinger equation, comparing the two schemes in [112] and [21] and a second article from Carjan, Rizea, and Strottman [29] that compares a few approaches in a physical application of quantum mechanics. Moreover, there is a concise description of the underlying problem from a physics view point by Frensley [60].

We remark that the key ideas presented here for the Schrödinger equation can also be generalized to other types of partial differential equations like parabolic problems, where the TBCs have a similar form [47].

This paper is organized as follows. In Section 2 we will sketch some techniques for solving the one-dimensional Schrödinger equation and derive several versions of *exact* transparent boundary conditions. Their efficient implementation by appropriate discretizations and/or approximations to obtain fast algorithms will be discussed in Section 3. In Section 4 we describe briefly how the obtained results can be generalized to two space dimensions and in Section 5 we give an outlook on how artificial boundary conditions can be derived for the Schrödinger equation with a cubic nonlinearity. Finally, several numerical examples in Section 6 illustrate the behaviour of the different approaches in 1D. Two appendices contain useful basic results related to fractional calculus and the $\mathcal{Z}$-transformation, which are used all along the paper.

2 Transparent boundary conditions for the Schrödinger equation

Let us set $\mathcal{R}^{\pm} = \{\pm\, x > 0\}$ and $\mathcal{R}_0^+ = \{x \ge 0\}$. It is well-known that (1.1) is well-posed in $L^2(\mathcal{R})$ (see, e.g., [102,104]):

Theorem 2.1. *Let $u^I \in L^2(\mathcal{R})$ and $V \in C([0,\infty[,L^\infty(\mathcal{R}))$. Then the system* (1.1) *has a unique*

solution $u \in C(\mathcal{R}_0^+, L^2(\mathcal{R}))$. Moreover, the "mass" is preserved, i.e.,

$$\|u(t)\|_{L^2(\mathcal{R})} = \|u^I\|_{L^2(\mathcal{R})}, \quad \forall t \geq 0.$$

In this section we sketch the different ways of deriving transparent boundary conditions (TBCs). We start with the classical derivation of the *continuous* TBC for the IVP (1.1) and give a reformulation, the pole condition. Secondly, we shall mimic this procedure for the time-discrete Schrödinger equation. This way we derive temporally discrete TBCs. Thirdly, we shall consider *spatially discrete TBCs*, and finally we shall review the *fully discrete TBCs*.

2.1 Continuous transparent boundary conditions

Continuous TBCs for the Schrödinger equation (1.1) were independently derived by several authors from various application fields (cf. [21,37,75,99,100], inhomogeneous extensions are analyzed in [17,22]) and generalization to linear, periodic potentials or piecewise constant potentials can be found in [55,56,61,86,101,134]. Such TBCs are non-local in t and connect $\partial_x v(x_{l,r}, t)$ with $v(x_{l,r}, t)$. As a Dirichlet-to-Neumann (DtN) map they read

$$\partial_{\mathbf{n}} v(x,t) = -\frac{e^{-\frac{\pi}{4}i}}{\sqrt{\pi}} e^{-iV_{l,r}t} \frac{d}{dt} \int_0^t \frac{v(x,\tau)e^{iV_{l,r}\tau}}{\sqrt{t-\tau}} d\tau \quad \text{at } x = x_l, x_r, \qquad (2.1)$$

where $\mathbf{n}$ denotes the outwardly unit normal vector at x_l, x_r.

Remark 2.1. Since the Schrödinger equation has (formally) a similar structure as the heat equation, analogous DtN-maps for the heat equation were already given by Carslaw and Jaeger in 1959 [30].

These boundary conditions may be derived from Eq. (1.1) as follows: With the decomposition $L^2(\mathcal{R}) = L^2(\Omega) \oplus L^2(\Omega_r \cup \Omega_l)$ for $\Omega =]x_l, x_r[$, $\Omega_l =]-\infty, x_l]$, and $\Omega_r = [x_r, \infty[$, Eq. (1.1) is equivalent to the coupled system

$$\begin{cases} (i\partial_t + \partial_x^2)v = V(x,t)v, & (x,t) \in \Omega \times \mathcal{R}^+, \\ \partial_x v(x,t) = \partial_x w(x,t), & x = x_{l,r}, \ t > 0, \\ v(x,0) = u^I(x), & x \in \Omega, \end{cases} \qquad (2.2)$$

$$\begin{cases} (i\partial_t + \partial_x^2)w = V_{l,r}w, & (x,t) \in (\Omega_l \cup \Omega_r) \times \mathcal{R}^+, \\ w(x,t) = v(x,t), & x = x_{l,r}, \ t > 0, \\ \lim_{|x| \to \infty} w(x,t) = 0, & t > 0, \\ w(x,0) = 0, & x \in \Omega_l \cup \Omega_r. \end{cases} \qquad (2.3)$$

Fig. 1 explains this splitting of the spatial domain $\mathcal{R}$ into interior and exterior problems and shows the basic idea of constructing the TBCs.
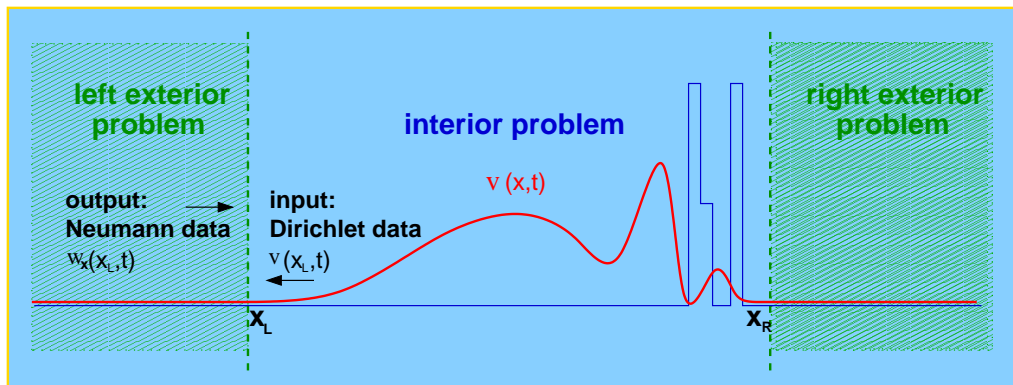
Figure 1: Decomposition of the domain and basic idea of the construction of the TBCs.

Next we apply a Laplace transformation in t to the exterior problems (2.3). The Laplace transformation with respect to the time variable t is defined by

$$\hat{w}(s) := \mathcal{L}(w)(s) := \int_{\mathcal{R}^+} w(t) e^{-st} dt, \tag{2.4}$$

where s is the time covariable.

In the following we focus on the derivation of the right TBC at x_r. The Laplace transformation of (2.3) (on Ω_r) reads

$$is\hat{w} + \partial_x^2 \hat{w} = V_r \hat{w}, \quad x \in \Omega_r. \tag{2.5}$$

The solution to this ordinary differential equation can be written as

$$\hat{w}(x,s) = A^+(s) e^{\sqrt[+]{-is+V_r} x} + A^-(s) e^{-\sqrt[+]{-is+V_r} x}, \quad x > x_r, \tag{2.6}$$

where the branch of the square root $\sqrt[+]{\ }$ is taken such that the real part is positive. However, since the solution must be in $L^2(\Omega_r)$, the coefficient A^+ must vanish. Using the Dirichlet data at the artificial boundary yields

$$\hat{w}(x,s) = e^{-\sqrt[+]{-is+V_r}(x-x_r)} \mathcal{L}(v(x_r,\cdot))(s),$$

and hence

$$\partial_x \hat{w}(x,s)|_{x=x_r} = -\sqrt[+]{-is+V_r}\, \hat{w}(x,s)|_{x=x_r}. \tag{2.7}$$

The analogous condition at the left boundary is

$$-\partial_x \hat{w}(x,s)|_{x=x_l} = -\sqrt[+]{-is+V_l}\, \hat{w}(x,s)|_{x=x_l}.$$

Inserting its inverse Laplace transformation into (2.2) yields

$$
\begin{aligned}
(i\partial_t + \partial_x^2)v &= V(x,t)v, \quad (x,t) \in \Omega \times \mathcal{R}^+, \\
\partial_\mathbf{n} v(x,t) &= \mathcal{L}^{-1}\left(-\sqrt[+]{-i\cdot + V_{l,r}}\,\hat{v}(x,\cdot)\right)(t) \\
&= \int_0^t f(t-\tau)v(x,\tau)d\tau, \quad x = x_{l,r}, \ t > 0, \\
v(x,0) &= u^I(x), \quad x \in \Omega,
\end{aligned}
\tag{2.8}
$$

where

$$
\mathcal{L}(f)(s) = F(s) = -\sqrt[+]{-is + V_{l,r}}
$$

and $\partial_\mathbf{n}$ is the outwardly directed normal derivative. By construction u coincides with v on Ω.

For a constant potential $V = V_r$ the Schrödinger equation can formally be factorized into left and right traveling waves (cf. [21]):

$$
\left(\partial_x - e^{-i\frac{\pi}{4}}\sqrt[+]{\partial_t + iV_r}\right)\left(\partial_x + e^{-i\frac{\pi}{4}}\sqrt[+]{\partial_t + iV_r}\right)u = 0, \quad x > x_r.
\tag{2.9}
$$

In the potential-free case ($V_r = 0$) the term $\sqrt{\partial_t} = \partial_t^{1/2}$ can be interpreted as a fractional 1/2-time derivative (cf. (A.2)). Allowing at $x = x_r$ only for outgoing waves one recovers formally the right TBC (2.1).

Remark 2.2 (Impedance Boundary Condition). A simple calculation shows that (2.1) is equivalent to the *impedance boundary condition* [99]

$$
u(x,t) = -\frac{e^{i\frac{\pi}{4}}}{\sqrt{\pi}}\int_0^t \frac{\partial_\mathbf{n} u(x,\tau)e^{-iV_{l,r}(t-\tau)}}{\sqrt{t-\tau}}d\tau, \quad \text{at} \ x = x_{l,r},
\tag{2.10}
$$

in the form of a Neumann-to-Dirichlet (NtD) map.

Remark 2.3 (Inhomogeneous TBC). The (homogeneous) TBC (2.1) was derived for the situation where an initial wave function is supported in the computational domain $]x_l, x_r[$, and it is leaving this domain without being reflected back. If an *incoming wave function* $u_{in}(t)$ is given at the right boundary (e.g. a left traveling plane wave), the inhomogeneous TBC

$$
\partial_x\big(u(x_r,t) - u_{in}(x_r,t)\big) = -\frac{e^{-i\frac{\pi}{4}}}{\sqrt{\pi}}e^{-iV_r t}\frac{d}{dt}\int_0^t \frac{(u(x_r,\tau) - u_{in}(x_r,\tau))e^{iV_r\tau}}{\sqrt{t-\tau}}d\tau,
\tag{2.11}
$$

has to be prescribed at $x = x_r$ (cf. [17, 22] for details).

Remark 2.4 (Noncompactly supported initial data). If the initial data $u^I(x)$ is not compactly supported inside the computational domain $]x_l,x_r[$, Levy derived a TBC [85], which has applications in radio wave propagation [87]. Assuming that the initial function $u^I(x)$ is continuous and $\partial_x u^I(x)$ is integrable for $x > x_r$, the *right TBC* reads

$$\partial_x u(x_r,t) = -\frac{e^{-\frac{\pi}{4}i}}{\sqrt{\pi}}\frac{d}{dt}\int_0^t \frac{u(x_r,\tau)}{\sqrt{t-\tau}}d\tau + \frac{e^{-\frac{\pi}{4}i}}{\sqrt{\pi t}}\int_{x_r}^\infty u_x^I(x)e^{\frac{i(x-x_r)^2}{t}}dx \qquad (2.12)$$

in the potential-free situation. Clearly, if $u^I(x) = 0$ for $x > x_r$ then (2.12) reduces to the previously obtained right TBC (2.1) in the potential-free case.

Remark 2.5 (Time-dependent exterior potential). Consider the Schrödinger equation with exterior potentials that only depend on time, i.e., $V(x,t)|_{\Omega_{l,r}} = V_{l,r}(t)$. The following *gauge change* in (1.1) then reduces this case to zero exterior potential [9]:

$$\psi_{l,r} = e^{i\mathcal{V}_{l,r}(t)}u_{l,r}, \quad \text{with} \quad \mathcal{V}_{l,r}(t) = \int_0^t V_{l,r}(s)ds, \ \forall t > 0.$$

The resulting TBC is then given by

$$\partial_{\mathbf{n}}u + e^{-i(\pi/4 - \mathcal{V}_{l,r}(t))}\partial_t^{1/2}(e^{-i\mathcal{V}_{l,r}(t)}u) = 0, \quad x = x_{l,r}. \qquad (2.13)$$

Remark 2.6 (Space- and time-dependent exterior potential). In the case of a space and time varying potential, the situation is much more complicated. There is no easy way for deriving the TBC. A direction investigated in [11] is to use the theory of fractional pseudo-differential operators. Based on these techniques, families of approximate artificial boundary conditions can be derived. A first-order approximation is obtained by using the BC (2.13) with the definition

$$\mathcal{V}_{l,r}(t) = \int_0^t V(x_{l,r},s)ds, \ \forall t > 0.$$

A second-order approximation yields

$$\begin{aligned}\partial_{\mathbf{n}}u &+ e^{-i(\pi/4 - \mathcal{V}_{l,r}(t))}\partial_t^{1/2}(e^{-i\mathcal{V}_{l,r}(t)}u) \\ &+ \frac{i}{4}\partial_x V|_{x=x_{l,r}}e^{i\mathcal{V}_{l,r}(t)}I_t(e^{-i\mathcal{V}_{l,r}(t)}u) = 0,\end{aligned} \qquad (2.14)$$

with I_t the integration operator over $[0,t]$. Higher-order approximations to the TBC can be derived by computing additional correction terms in the asymptotic expansion.

We summarize the procedure to derive the continuous TBC:

> 1. Split original problem into coupled equations: interior and exterior problems.
>
> 2. Apply a Laplace transformation (2.4) in time t.
>
> 3. Solve the ordinary differential equations in x.
>
> 4. Allow only "outgoing" waves by selecting the decaying solution as $x \to \pm\infty$.
>
> 5. Match Dirichlet and Neumann values at $x = x_l$, $x = x_r$.
>
> 6. Apply the inverse Laplace transformation.

For the IBVP on Ω with a DtN- or a NtD-TBC, existence and uniqueness of the solution has been proved (see, e.g., [9]).

2.2 An alternative formulation — the pole condition

The pole condition approach [106, 107] might be viewed as an alternative derivation of the TBC, which avoids step 3, the explicit solution of the ordinary differential equations in x, and yields an alternative local approximation of the TBC, see Section 3.6. It was developed by Schmidt, Hohage and Zschiedrich for Helmholtz problems on unbounded domains [76, 115]. Starting from the time-transformed exterior equation (2.5) a Laplace transformation is applied to the spatial variable x with covariable q

$$isW(q,s) + q^2 W(q,s) - q\hat{w}(x_r,s) - \partial_x \hat{w}(x_r,s) = V_r W(q,s). \tag{2.15}$$

Solving for $W(q,s)$ one obtains

$$W(q,s) = \underbrace{\frac{\hat{w}(x_r,s) + \frac{\partial_x \hat{w}(x_r,s)}{\sqrt[+]{-is+V_r}}}{2(q - \sqrt[+]{-is+V_r})}}_{T1} + \underbrace{\frac{\hat{w}(x_r,s) - \frac{\partial_x \hat{w}(x_r,s)}{\sqrt[+]{-is+V_r}}}{2(q + \sqrt[+]{-is+V_r})}}_{T2}, \tag{2.16}$$

where $T1$, $T2$ denote the two terms in the partial fraction decomposition of $W(q,s) = T1 + T2$.

In deriving the exact boundary condition (2.7) we used an asymptotic decay argument to discard the first term in (2.6). To obtain the same for the pole condition approach we use the following closely related argument: Since s lies in the right half plane $\sqrt[+]{-is+V_r}$ takes values in the fourth quadrant. Thus the terms $T1$ and $T2$ can be distinguished by the position of their poles w.r.t. q. Transforming back to space domain it can be seen that the term $T1$ corresponds to the term $A^+(s)e^{\sqrt[+]{-is+V_r}x}$ in (2.6), whereas $T2$ corresponds to $A^-(s)e^{-\sqrt[+]{-is+V_r}x}$. Thus one can exclude the term $T1$ by forcing W to be analytic w.r.t. q in some half-plane containing the fourth quadrant but not the second quadrant. This is equivalent to

$$\hat{w}(x_r,s) + \frac{\partial_x \hat{w}(x_r,s)}{\sqrt[+]{-is+V_r}} = 0,$$

which is condition (2.7). Following these arguments we make the following definition of the pole condition for the Schrödinger equation.

Definition 2.1. A solution $\hat{w}(x,s)$ of

$$is\hat{w} + \partial_x^2 \hat{w} = V_r \hat{w} \quad \text{for } x \in \Omega_r$$

satisfies the pole condition for the Schrödinger equation if, for all s with $\text{Re}\,s > 0$ fixed, its Laplace transform in the variable x has a holomorphic extension to some half-plane containing the fourth quadrant but not the second quadrant.

We have the following theorem.

Theorem 2.2. *If and only if a function w obeys the pole condition, then the transparent boundary condition*

$$\partial_x \hat{w}(x,s)\big|_{x=x_r} = - \sqrt[+]{-is + V_r}\, \hat{w}(x,s)\big|_{x=x_r}$$

holds.

While the continuous TBCs (2.1) fully solve the problem of confining the spatial domain to a bounded interval, their numerical discretization is not trivial at all and has attracted lots of attention. In the following subsections we will present different approaches to derive (semi)discrete TBCs and ABCs for the 1D Schrödinger equation (1.1).

Finally, we show in Fig. 2 the structure of the different derivation strategies explained in the following two sections. Note that the arrows in Fig. 2 stand for a certain close relation between the approaches; they do not mean 'can be derived from'.

2.3 Temporally discrete transparent boundary conditions

We consider the problem (1.1) discretized uniformly in time with the step size Δt by an A-stable multi-step method, cf. [69, Chapter V.1], and denote by u^n the approximation to $u(x,n\Delta t)$:

$$\frac{i}{\Delta t}\sum_{j=0}^{K} \alpha_j u^{n-j} = \sum_{j=0}^{K} \beta_j\left(-\partial_x^2 + V\right) u^{n-j}, \quad n \geq K. \tag{2.17}$$

Analogously to Step (1) of Section 2.1 we split the problem into interior and exterior problems (with respective solutions v^n and w^n). Instead of applying the Laplace transformation (Step (2)) w.r.t. t to equation (1.1), we apply a $\mathcal{Z}$-transformation (see Appendix B) to (2.17). The $\mathcal{Z}$-transformation of a sequence (u^n) is defined by

$$\mathcal{Z}(u^n) = \hat{u}(z) := \sum_{n=0}^{\infty} u^n z^{-n}, \quad z \in \mathbb{C}, \quad |z| > R(\mathcal{Z}(u^n)), \tag{2.18}$$

where $R(\mathcal{Z}(u^n))$ is the radius of convergence of the Laurent series $\mathcal{Z}(u^n)$.
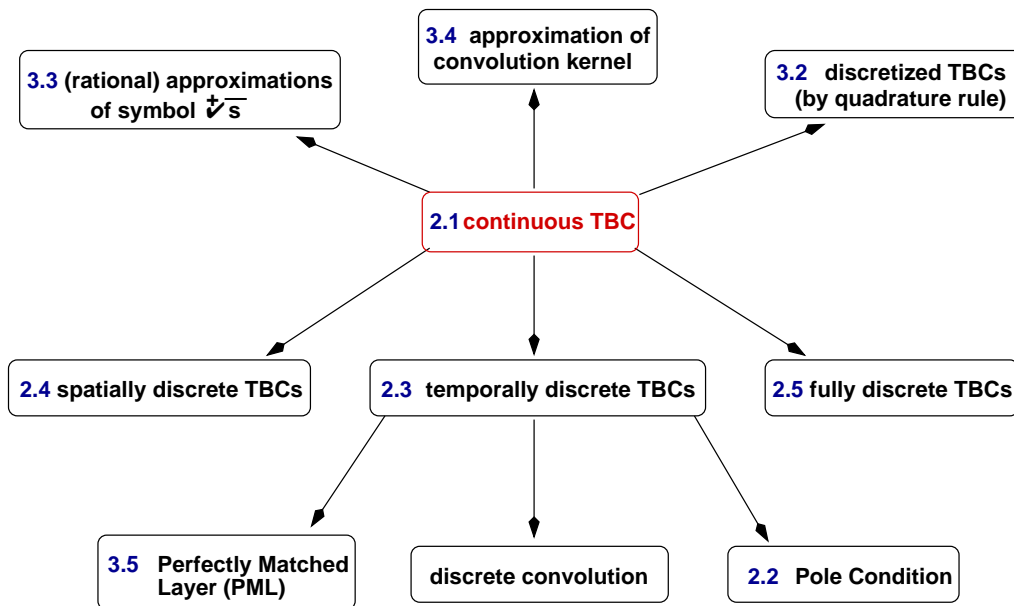
Figure 2: Different approaches to derive (semi)discrete TBCs and ABCs for the 1D Schrödinger equation (1.1).

The $\mathcal{Z}$-transformation of (2.17) yields the second order ordinary differential equation:

$$\left(\partial_x^2 + i\frac{\delta(z)}{\Delta t} - V_r\right)\hat{w}(z) = 0, \quad x > x_r, \tag{2.19}$$

where

$$\delta(z) = \left(\sum_{j=0}^{K}\alpha_j z^{K-j}\right) \bigg/ \left(\sum_{j=0}^{K}\beta_j z^{K-j}\right)$$

is the *generating function of the time integration scheme*. On top of the standard assumption $\mathrm{supp}(u^I) \subset [x_l, x_r]$ we made here the following assumption on the start-up procedure for the multi-step method (2.17):

$$\mathrm{supp}(u^j) \subset [x_l, x_r], \quad 0 \le j \le K-1.$$

Example 2.1. The *trapezoidal rule* discretization is given by

$$
\begin{aligned}
&i\frac{u^{n+1}-u^n}{\Delta t} = -\partial_x^2\frac{u^{n+1}+u^n}{2} + \frac{V^{n+1}(x)u^{n+1}+V^n(x)u^n}{2}, \quad x \in \mathcal{R}, \forall n \in \mathbb{N}_0,\\
&\lim_{|x|\to\infty} u^n(x) = 0, \quad \forall n \in \mathbb{N}_0,\\
&u^0 = u^I(x) \quad \text{given for } x \in \mathcal{R}.
\end{aligned}
\tag{2.20}
$$

This method is also known as the Crank-Nicolson scheme and its *generating function* is $\delta(z) = 2(z-1)/(z+1)$.

Example 2.2. For the implicit Euler method we have $\delta(z) = (z-1)/z$.

Eq. (2.19) is the starting point for deriving the TBC as well as several ABCs for (2.17). The semi-discrete TBC is obtained by solving the differential equation (2.19) (Step (3)). Its general solution is (cf. (2.6)):

$$\hat{w}(x,z) = A^+(z) e^{i \sqrt[+]{i\frac{\delta(z)}{\Delta t} - V_r} x} + A^-(z) e^{-i \sqrt[+]{i\frac{\delta(z)}{\Delta t} - V_r} x}, \quad x > x_r. \tag{2.21}$$

In order for u^n to lie in $L^2(]x_r, \infty[)$, A^- must vanish. This is due to the fact that δ maps $\{|z| > 1\}$ into the right half-plane $\{\operatorname{Re}(z) > 0\}$ (due to A-stability), and hence

$$\operatorname{Re}\left(-i \sqrt[+]{i\frac{\delta(z)}{\Delta t} - V_r}\right) > 0, \quad \forall |z| > 1. \tag{2.22}$$

Differentiating $\hat{w}(x,z)$ w.r.t. x leads to

$$\mathcal{Z}(\partial_x w^n)(z) = i \sqrt[+]{i\frac{\delta(z)}{\Delta t} - V_r} \, \mathcal{Z}(w^n)(z), \tag{2.23}$$

at $x = x_r$. An inverse $\mathcal{Z}$-transformation yields an expression for $\partial_x w^n(x_r)$ in terms of $w^k(x_r), 0 \le k \le n$. The resulting TBC is a discrete temporal convolution which depends on the generating function δ.

Resuming Example 2.1 we finally obtain for the interior problem

$$\begin{aligned} i\frac{v^{n+1}-v^n}{\Delta t} &= -\partial_x^2 \frac{v^{n+1}+v^n}{2} + \frac{V^{n+1}(x)v^{n+1}+V^n(x)v^n}{2}, \quad x \in \Omega, \forall n \in \mathbb{N}_0, \\ v^0(x) &= u^I(x), \quad x \in \Omega, \\ \partial_{\mathbf{n}} v^{n+1} &= \sum_{k=0}^{n+1} \psi_k^{(l,r)} v^{n+1-k}, \quad \text{at } x = x_l, x_r, \end{aligned} \tag{2.24}$$

where the weights $\psi_n^{(l,r)}$ are given by

$$\hat{\psi}(z) = \mathcal{Z}(\psi_n^{(l,r)})(z) = i \sqrt[+]{i\frac{\delta(z)}{\Delta t} - V_{l,r}}.$$

The weights ψ_n can be obtained either analytically or numerically, depending on δ and the potential $V_{l,r}$. In case of the trapezoidal rule and a vanishing potential, one gets explicitly the coefficients (see for example [9, 112–114, 131])

$$\begin{aligned} \psi_k &= -e^{-\frac{i\pi}{4}} \sqrt{\frac{2}{\Delta t}} (-1)^k \tilde{\psi}_k, \quad k \in \mathbb{N}_0, \\ (\tilde{\psi}_0, \tilde{\psi}_1, \tilde{\psi}_2, \tilde{\psi}_3, \tilde{\psi}_4, \tilde{\psi}_5, \cdots) &= \left(1, 1, \frac{1}{2}, \frac{1}{2}, \frac{1\cdot3}{2\cdot4}, \frac{1\cdot3}{2\cdot4}, \cdots\right). \end{aligned} \tag{2.25}$$

In a very similar way, the following formula can be derived for an approximation of the NtD map (2.10). From (2.23) one obtains

$$\mathcal{Z}(w^n)(z) = F\left(\frac{\delta(z)}{\Delta t}\right)\mathcal{Z}(\partial_x w^n)(z), \quad \text{with } F^{(r)}(s) = \frac{1}{i\sqrt[+]{is - V_r}} \tag{2.26}$$

which leads to

$$v^{n+1} = \sum_{k=0}^{n+1} \check{\psi}_k \partial_{\mathbf{n}} v^{n+1-k}, \quad \text{at } x = x_l, x_r. \tag{2.27}$$

In case the potential is 0 and the trapezoidal rule is used, these can be calculated analytically. One obtains

$$\check{\psi}_n = -e^{\frac{i\pi}{4}}\sqrt{\frac{\Delta t}{2}}\tilde{\psi}_k$$

with $\tilde{\psi}_n$ as in (2.25). This is a trapezoidal rule time discretization of the fractional integral operator of order $1/2$.

This is a special case of the convolution quadrature developed by Lubich [91, 92], where for the Laplace transform $F(s) = \mathcal{L}(f)(s)$ of the kernel $f(t)$ the convolution is approximated as

$$\int_0^{(n+1)\Delta t} f\big((n+1)\Delta t - \tau\big)\partial_{\mathbf{n}} v(\tau) \approx \sum_{k=0}^{n+1} \check{\psi}_k \partial_{\mathbf{n}} v^{n+1-k},$$

with weights defined by

$$\mathcal{Z}(\check{\psi}_n^{(l,r)})(z) = F^{(l,r)}\left(\frac{\delta(z)}{\Delta t}\right). \tag{2.28}$$

In the general case the weights have to be calculated numerically, which can be done efficiently and accurately using the Fast Fourier Transforms, see [92].

One advantage of the procedure of this subsection is that we can expect to obtain a stable, semi-discrete IBVP. The trapezoidal rule discretization of the Schrödinger equation on the real line is stable. Using the time discrete approximation of the convolution integral based on the trapezoidal rule, the result of the restricted problem coincides with the original problem inside the computational domain, so the method is unconditionally stable (cf. Theorems 3 and 4 in [9]).

Furthermore, when using an internal spatial discretization based on conforming finite elements, also the fully discrete scheme is unconditionally stable (cf. Section 3.4 in [9]).

Remark 2.7 (Time discrete pole condition)**.** As for the continuous case we can reformulate the transparent boundary condition as the pole condition, now for $\hat{w}(x,z)$ instead of $\hat{w}(x,s)$.

2.4 Spatially discrete transparent boundary conditions

Spatially discrete TBCs are obtained if instead of solving the ordinary differential equation (2.5) (Step (3)), a difference equation w.r.t. the spatial variable is solved.

Spatially semi-discrete TBCs are derived by Alonso-Mallo and Reguera in [4, 6] and by Lubich and Schädle in [93]. There, the Schrödinger equation (1.1) discretized in space using the standard second order difference quotient

$$D_x^2 u_j = \frac{u_{j-1} - 2u_j + u_{j+1}}{\Delta x^2} \tag{2.29}$$

is considered. This provides the following system of ordinary differential equations in time

$$\begin{aligned} i\partial_t u_j(t) &= -D_x^2 u_j(t) + V u_j(t), \quad j \in \mathbb{Z}, t > 0, \\ \lim_{|j| \to \infty} u_j(t) &= 0, \quad t > 0, \\ u_j(0) &= u^I(j\Delta x), \quad j \in \mathbb{Z}, \end{aligned} \tag{2.30}$$

where $x_j = x_l + j\Delta x$, $j \in \mathbb{Z}$ form a uniform grid and $u_j(t)$ denotes an approximation to $u(x_j, t)$. We choose Δx and J such that $x_J = x_r$. Again, we assume here for simplicity that V is constant.

As before the spatially discrete Schrödinger equation (2.30) is split into coupled interior and exterior problems (Step 1). Applying a Laplace transformation in time t (Step 2) to the exterior problems one obtains for the right exterior problem

$$is\hat{w}_j(s) + D_x^2 \hat{w}_j(s) = V_r \hat{w}_j(s), \quad j > J. \tag{2.31}$$

The solution to this difference equation is given as (cf. (2.6))

$$\hat{w}_j(s) = A^+(s)\chi^{j-J}(s) + A^-(s)\chi^{-(j-J)}(s), \quad j > J, \tag{2.32}$$

where $\chi(s)$, $\chi^{-1}(s)$ are the roots of the characteristic polynomial

$$X^2 - 2\left(1 - \Delta x^2(is - V_r)/2\right)X + 1 = 0. \tag{2.33}$$

Choosing

$$\chi(s) = 1 - \frac{\Delta x^2}{2}(is - V_r) + \sqrt[+]{\frac{\Delta x^2}{2}(is - V_r)\left(\frac{\Delta x^2}{2}(is - V_r) - 2\right)}, \tag{2.34}$$

A^- must vanish. From the coupling condition $\hat{w}_J = \hat{v}_J$ we obtain

$$A^+ = \hat{v}_J(s)$$

and hence the spatially discrete right TBC is

$$\hat{v}_{J-1}(s) = \chi^{-1}(s)\hat{v}_J(s).$$

The DtN operator at the right boundary is thus given by

$$\hat{v}_{J-1}(s) - \hat{v}_J(s) = \left(\chi^{-1}(s) - 1 \right) \hat{v}_J(s). \tag{2.35}$$

An analogous result holds for the left boundary.

Transforming back to the time-domain one obtains finally

$$
\begin{aligned}
\left(i\partial_t + D_x^2 \right) v_j(t) &= V(x_j,t)v_j(t), \quad j=0,\cdots,J, \ \ t\geq 0,\\
v_{J-1}(t) - v_J(t) &= \mathcal{L}^{-1} \left((\chi^{-1}(\cdot) - 1)\hat{v}_J(\cdot) \right)(t), \quad t\geq 0,\\
v_j(0) &= u^I(x_j), \qquad j=0,\cdots,J.
\end{aligned}
\tag{2.36}
$$

Spatially discrete NtD boundary conditions can be derived in a very similar way:

$$v_J(t) = \mathcal{L}^{-1} \left(\left(\chi^{-1}(\cdot) - 1 \right)^{-1} (\hat{v}_{J-1}(\cdot) - \hat{v}_J(\cdot)) \right)(t), \quad t\geq 0. \tag{2.37}$$

2.5 Fully discrete transparent boundary conditions

A combination of temporally and spatially discrete TBCs yields fully discrete TBCs for problem (2.2). While one could use here any spatial discretization (that is regular in the exterior domain), we consider here the example of second order finite differences, i.e.,

$$
\begin{aligned}
i\frac{u_j^{n+1} - u_j^n}{\Delta t} &= -D_x^2 \frac{u_j^{n+1} + u_j^n}{2} + \frac{V_j^{n+1} u_j^{n+1} + V_j^n u_j^n}{2}, \quad j\in\mathbb{Z}, \ n\in\mathbb{N}_0,\\
\lim_{|j|\to\infty} u_j^n &= 0, \quad n\in\mathbb{N}_0,\\
u_j^0 &= u^I(j\Delta x), \quad j\in\mathbb{Z},
\end{aligned}
\tag{2.38}
$$

where D_x^2 denotes the standard second order difference quotient (2.29) and $x_j = x_l + j\Delta x$, $j\in\mathbb{Z}$ is a uniform grid. The right artificial boundary is located at $x_J = x_l + J\Delta x = x_r$ and the left boundary at $x_0 = x_l$. Again we apply the $\mathcal{Z}$-transformation (2.18) and obtain, as a discrete analogue of (2.19) in the right exterior domain:

$$\left(D_x^2 + i\frac{\delta(z)}{\Delta t} - V_r \right) \hat{w}_j(z) = 0, \quad j > J. \tag{2.39}$$

This is a *second-order difference equation with constant coefficients* which reads explicitly

$$\hat{w}_{j+1}(z) - 2 \left(1 - \frac{\Delta x^2}{2} \left(i\frac{\delta(z)}{\Delta t} + V_r \right) \right) \hat{w}_j(z) + \hat{w}_{j-1}(z) = 0, \quad j > J. \tag{2.40}$$

Its general solution takes the form (cf. (2.32))

$$\hat{w}_j(z) = A^+(z)\chi^{j-J}(z) + A^-(z)\chi^{-(j-J)}(z), \quad j\geq J-1, \tag{2.41}$$

where $\chi(z)$ and $\chi(z)^{-1}$ are the roots of the quadratic equation (cf. (2.33)):

$$X^2 - 2\left(1 - \frac{\Delta x^2}{2}\left(i\frac{\delta(z)}{\Delta t} + V_r\right)\right)X + 1 = 0. \tag{2.42}$$

In order to have decaying solutions $\hat{w}_j(z)$ outside of the computational domain (i.e., for $j \to \infty$) we have to choose the branch of the square root such that $|\chi(z)| > 1$.

Finally we obtain the $\mathcal{Z}$-transformed right discrete TBC [15]:

$$\hat{u}_{J-1}(z) = \chi^{-1}(z)\hat{u}_J(z). \tag{2.43}$$

The transformed boundary kernel $\chi(z)$ is calculated as (cf. [15, 48, 49, 116]):

$$\chi(z) = 1 - \frac{\Delta x^2}{2}\left(i\frac{\delta(z)}{\Delta t} - V_r\right) + {}^+\!\!\sqrt{\frac{\Delta x^2}{2}\left(i\frac{\delta(z)}{\Delta t} - V_r\right)\left(\frac{\Delta x^2}{2}\left(i\frac{\delta(z)}{\Delta t} - V_r\right) - 2\right)}. \tag{2.44}$$

The inverse $\mathcal{Z}$-transform of χ then defines the convolution coefficients for the discrete TBCs:

$$(\chi_n) := \mathcal{Z}^{-1}(\chi(z)), \quad n \in \mathbb{N}_0.$$

Since the magnitude of χ_n does not decay as $n \to \infty$ (χ_n behaves like const$\cdot(-1)^n$ for large n), it is more convenient to use a modified formulation of the discrete TBCs (cf. [49]). We introduce

$$\hat{s}(z) := \frac{z+1}{z}\hat{\chi}(z), \text{ and } (s_n) = \mathcal{Z}^{-1}\{\hat{s}(z)\}, \tag{2.45}$$

which satisfy

$$s_0 = \chi_0, \quad s_n = \chi_n + \chi_{n-1} = \mathcal{O}\left(n^{-\frac{3}{2}}\right), \quad n \in \mathbb{N}. \tag{2.46}$$

The corresponding Laurent series of $\hat{s}(z)$ converges (and is continuous) for $|z| \geq 1$ because of the decay (2.46).

In physical space the right discrete TBC (written as DtN map) then reads (cf. [49, Thm. 3.8]):

$$u_J^n - u_{J-1}^n = -\sum_{k=1}^{n} s_{n-k}u_J^k + u_{J-1}^{n-1}, \quad n \in \mathbb{N}, \tag{2.47}$$

with the explicitly calculated convolution weights:

$$s_n = (-iR+\sigma)\delta_n^0 + (1+iR+\sigma)\delta_n^1 + \gamma e^{-in\varphi}\frac{P_n(\mu) - P_{n-2}(\mu)}{2n-1}, \tag{2.48}$$

$$\varphi = \arctan\frac{2R(\sigma+1)}{R^2 - 2\sigma - \sigma^2}, \quad \mu = \frac{R^2 + 2\sigma + \sigma^2}{\sqrt{(R^2+\sigma^2)(R^2+(\sigma+2)^2)}},$$

$$\sigma = \Delta x^2 V_r, \quad R = \frac{\Delta x^2}{\Delta t} \quad \gamma = i\sqrt[4]{(R^2+\sigma^2)(R^2+(\sigma+2)^2)}\,e^{i\varphi/2}.$$

Here P_n denotes the Legendre polynomials ($P_{-1} \equiv P_{-2} \equiv 0$), and δ_n^k is the Kronecker symbol.

In order to formulate the discrete TBC as in (2.43) it is necessary that the discrete initial condition vanishes at the two adjacent (spatial) grid points appearing in (2.43). Here, we chose to formulate the discrete TBC at the boundary of the computational interval and one grid point in the *interior*. Hence we have assumed that the initial condition satisfies

$$u_0^0 = u_1^0 = 0, \quad u_{J-1}^0 = u_J^0 = 0.$$

However, without any change to our subsequent analysis one could also prescribe the discrete TBC at $j = -1,0$ and at $j = J, J+1$, respectively. We remark that a strategy to overcome this restriction ($\text{supp}(u^I) \subset [x_l, x_r]$) can be found in [49, 54].

We remark that other interior discretization schemes for the Schrödinger equation could be used (e.g. a fourth order Numerov-type discretization [98]). Also, discrete TBCs for systems of Schrödinger equations [135], for discrete predictor-corrector Schrödinger-Poisson systems [51], for the case of a periodic potential at infinity [61] or a linear exterior potential [50] and for split-step methods [52, 53] were derived. Finally, in [136] it is shown how to extend these results on discrete TBCs for solving nonlinear Schrödinger equations.

Let us note that the limit $\Delta x \to 0$ of the discrete TBCs of Arnold and Ehrhardt [49] coincides with the temporally semi-discrete TBC of Schmidt and Deuflhard [112] and of Schädle, cf. [108].

3 Discretizations and approximations

In Section 2 we presented several versions of *exact* transparent boundary conditions. Theoretically they completely solve the problem of cutting off the unbounded exterior domain. However, for an efficient implementation the TBCs have to be discretized and/or approximated. To this end there exist three main approaches in the literature which we shall describe in this section: The first strategy consists in direct discretizations of the TBC by quadrature rule and is briefly reviewed in Section 3.2. In Section 3.3 we present approximations of the convolution in TBC based on rational approximations for the Fourier-symbol of the convolution operator. In Section 3.4 the convolution kernel is approximated by finite sums of exponentials. The approximations in 3.3 and 3.4 can be interpreted both in terms of discretization of the convolution and of approximations for the Fourier-symbol of the TBC kernel, but the derivations of the two approaches are distinctly different.

3.1 Space discretization

In the numerical experiments in Section 6 we will use second order finite differences (2.29) and finite elements of order 1 and 2 to discretize in space. While the Neumann data

is easily incorporated in a finite element setting, there are several ways of approximating $\partial_{\mathbf{n}}$ in the finite difference setting. Let Δx be the grid width, then a first order accurate approximation is given by

$$\partial_{\mathbf{n}}u(x_{l,r}) \approx \begin{cases} \dfrac{u(x_l)-u(x_l+\Delta x)}{\Delta x}, \\ \dfrac{u(x_r)-u(x_r-\Delta x)}{\Delta x}. \end{cases} \tag{3.1}$$

Second order accurate approximations are obtained with

$$\partial_{\mathbf{n}}u(x_{l,r}) \approx \begin{cases} \dfrac{u(x_l-\Delta x)-u(x_l+\Delta x)}{2\Delta x}, \\ \dfrac{u(x_r+\Delta x)-u(x_r-\Delta x)}{2\Delta x}, \end{cases} \tag{3.2}$$

or by using a correction term in (3.1)

$$\partial_{\mathbf{n}}u(x_{l,r}) \approx \begin{cases} \dfrac{u(x_l)-u(x_l+\Delta x)}{\Delta x} + \dfrac{\Delta x}{2}\partial_x^2 u(x_l), \\ \dfrac{u(x_r)-u(x_r-\Delta x)}{\Delta x} + \dfrac{\Delta x}{2}\partial_x^2 u(x_r). \end{cases} \tag{3.3}$$

Here for $\partial_x^2 u(x_{l,r})$ the PDE is inserted.

3.2 Discretizations of the convolution integrals by quadrature formulas

In Section 2.3 a very natural way to approximate the convolution integrals by convolution quadrature was presented. The convolution weights there were obtained by the same time-integration scheme that is used in the interior. However the first idea to incorporate the TBC in a numerical scheme is an *ad-hoc discretization*. This was done e.g. by Mayfield [96] and by Baskakov and Popov in [21]. For a more systematic discretization approach we refer to [73].

3.2.1 Discretization of Mayfield

Mayfield [96] proposed the approximation for the TBC in the form (2.10)

$$\int_0^{t_{n+1}} \frac{u_x(x_r,t_{n+1}-\tau)e^{-iV_r\tau}}{\sqrt{\tau}}d\tau$$

$$\approx \frac{1}{\Delta x}\sum_{k=0}^{n}(u_J^{n+1-k}-u_{J-1}^{n+1-k})e^{-iV_rk\Delta t}\int_{t_k}^{t_{k+1}}\frac{d\tau}{\sqrt{\tau}}$$

$$= \frac{2\sqrt{\Delta t}}{\Delta x}\sum_{k=0}^{n}\frac{(u_J^{n+1-k}-u_{J-1}^{n+1-k})e^{-iV_rk\Delta t}}{\sqrt{k+1}+\sqrt{k}}, \tag{3.4}$$

Figure 3: Discretized TBC of Mayfield: Stability regions.

where the left-point rectangular quadrature rule and (3.1) are used to discretize the normal derivative. This leads to the following *discretized TBC* for the Schrödinger equation:

$$u_J^{n+1} - u_{J-1}^{n+1} = \frac{\Delta x}{2B\sqrt{\Delta t}} u_J^{n+1} - \sum_{k=1}^{n} \left(u_J^{n+1-k} - u_{J-1}^{n+1-k} \right) \tilde{\ell}_k, \tag{3.5}$$

with

$$B = -\frac{1}{\sqrt{2\pi}} e^{i\frac{\pi}{4}}, \qquad \tilde{\ell}_k = \frac{e^{-iV_r k \Delta t}}{\sqrt{k+1} + \sqrt{k}}, \quad k = 1, 2, \cdots.$$

On the fully discrete level this BC is no longer perfectly transparent. Moreover, the resulting scheme for the IBVP exhibits a stability problem. With a homogeneous Dirichlet BC at $j=0$ and the discretized TBC (3.5), Mayfield obtained the following result:

Theorem 3.1 ([96]). *The numerical scheme consisting of the Crank-Nicolson/finite-differences in the interior domain $j=1,\cdots,J-1$ (cf. (2.38)) and the discretized TBC (3.5) is stable, if and only if*

$$4\pi \frac{\Delta t}{\Delta x^2} \in \bigcup_{j \in \mathbb{N}_0} \left[(2j+1)^{-2}, (2j)^{-2} \right]. \tag{3.6}$$

This shows that the chosen discretization of the TBC (3.5) destroys the unconditional stability of the underlying Crank-Nicolson scheme (2.38). The *stability regions* of Theorem 3.1 are illustrated in Fig. 3 ($c = 4\pi$) as dark areas. The light intervals are regions of instability.

3.2.2 Discretization of Baskakov and Popov

A similar strategy, but using a higher-order quadrature rule for the l.h.s. of (2.1) was introduced by Baskakov and Popov in [21] for $V_r = 0$. They used a piecewise linear approximation of the function $u(x_r, \tau)$ in the integral of the TBC (2.1). Using $u(x_r, 0) = 0$ yields

$$\int_0^{t_{n+1}} \frac{d}{dt} u(x_r, \tau) \frac{d\tau}{\sqrt{t_{n+1} - \tau}} \approx \frac{2}{\Delta t} \left(u_J^{n+1} - \sum_{k=1}^{n} \gamma_k u_J^{n+1-k} \right) \tag{3.7}$$

with the weights

$$\gamma_k = \frac{2}{(\sqrt{k+1} + \sqrt{k})(\sqrt{k} + \sqrt{k-1})(\sqrt{k+1} + \sqrt{k-1})}. \tag{3.8}$$

In [21] finite differences (2.29) are used together with (3.2).

Recently, Sun and Wu [124] analyzed the standard Crank-Nicolson scheme for the interior domain in conjunction with the above discrete convolution (3.7) extended to non-zero potential, but using (3.1) instead of (3.2). They proved the unique solvability of their algebraic system, unconditional stability and convergence with the order $\mathcal{O}(\Delta x^{3/2} + \Delta t^{3/2}\Delta x^{-1/2})$. Moreover, this approach typically induces less numerical reflections than the Mayfield-type discretization (3.5).

3.3 Rational approximations of the Fourier symbol

In pseudo differential calculus the Laplace transform of the kernel is identified with the Fourier symbol. Now we consider strategies that directly approximate the Fourier symbol by a rational function.

As we have seen, the fractional derivative operator $\partial_t^{1/2}$ in the continuous TBC is nonlocal in time. This is due to the non-polynomial nature of its Fourier symbol, which reads $\sqrt[+]{i\omega}$, where $\sqrt[+]{\cdot}$ denotes the branch of the square root with positive real part. In the spatially discrete case the Fourier symbol is given in (2.34). A rational approximation of these symbols, however, allows for a local in time treatment of the corresponding approximated convolution. For all of the subsequent methods some *a priori* information on the dominant wavenumber of the solution at the boundary is needed. Otherwise the reflection coefficient of outgoing waves can be unacceptably large.

3.3.1 Approaches of Bruneau-Di Menza, Szeftel, Shibata, and Kuska

Bruneau and Di Menza [27, 40] considered the *continuous* TBC in Fourier space (for its Laplace analogue cf. (2.7)):

$$\partial_x \hat{u}(x_r, \omega) = -e^{i\pi/4} \sqrt[+]{i\omega}\, \hat{u}(x_r, \omega). \tag{3.9}$$

and approximate the symbol $\sqrt[+]{i\omega}$ by a rational function

$$R_m(i\omega) = a_0^m + \sum_{k=1}^{m} \frac{a_k^m i\omega}{i\omega + d_k^m} = \sum_{k=0}^{m} a_k^m - \sum_{k=1}^{m} \frac{a_k^m d_k^m}{i\omega + d_k^m},$$

$$a_k^m > 0, \quad k = 0, \cdots, m, \quad d_k^m > 0, \quad k = 1, \cdots, m.$$

They require $R_m(i\omega)$ to interpolate $\sqrt[+]{i\omega}$ at $2m+1$ distinct points

$$\{\omega_0, (\pm i\omega_k)_{k=1,\cdots,m}\}, \quad \omega_k \in [0, \rho], \text{ and } \omega_{k+1} > \omega_k, \quad k = 0, \cdots, m,$$

for some $\rho > 0$. In order to compute the coefficients a_k^m and d_k^m, they define the set E_m of all rational functions $r(z) = P_m(z)/Q_m(z)$ (with deg $P_m = $ deg $Q_m = m$) which interpolate $\sqrt[+]{i\omega}$ on the previous family of points. Then, they choose $R_m \in E_m$ by minimizing $\|R_m(i\omega) - \sqrt[+]{i\omega}\|_{L^2(0,\rho)}$.

Thus, the approximation of (3.9) becomes

$$\partial_x \hat{u}(x_r,\omega) = -e^{i\pi/4} \left[\left(\sum_{k=0}^{m} a_k^m \right) \hat{u}(x_r,\omega) - \sum_{k=1}^{m} \frac{a_k^m d_k^m}{i\omega + d_k^m} \hat{u}(x_r,\omega) \right]. \qquad (3.10)$$

Following an idea of Lindmann [89], they introduce auxiliary functions $\varphi_k = \varphi_k(t)_{k=1,\cdots,m}$ at the boundary which satisfy

$$\frac{1}{i\omega + d_k^m} \hat{u}(x_r) = \hat{\varphi}_k, \quad k=1,\cdots,m.$$

After a Fourier inversion, φ_k satisfy the ordinary differential equation

$$\frac{d\varphi_k}{dt} + d_k^m \varphi_k = u(x_r,t), \quad \varphi_k(0) = 0, \quad k=1,\cdots,m.$$

Therefore, the boundary conditions become local in time and read

$$\begin{cases} \partial_{\mathbf{n}} u = -e^{-\frac{i\pi}{4}} \left[\left(\sum_{k=0}^{m} a_k^m \right) u - \sum_{k=1}^{m} a_k^m d_k^m \varphi_k \right], & \text{on } x=x_r, \ t>0, \\ \dfrac{d\varphi_k}{dt} + d_k^m \varphi_k = u(x_r,t), & t>0, \ k=1,\cdots,m, \\ \varphi_k(0) = 0, & t>0, \ k=1,\cdots,m. \end{cases} \qquad (3.11)$$

In [126], Szeftel also uses a rational approximation of $\sqrt[+]{i\omega}$ but proposes a different choice of coefficients. As a first attempt he considers the Padé approximation [20] leading to

$$a_0^m = 0, \quad a_k^m = \frac{1}{m \cos^2 \left(\frac{(2k+1)\pi}{4m} \right)}, \quad d_k^m = \tan^2 \left(\frac{(2k+1)\pi}{4m} \right). \qquad (3.12)$$

As an alternative he proposes to compute the coefficients of the rational approximation by optimizing the *reflection coefficient*

$$RC(\omega) = \frac{-\sqrt{\omega} - ia_0^m - i \displaystyle\sum_{k=1}^{m} \dfrac{a_k^m(-\omega)}{-\omega + d_k^m}}{\sqrt{\omega} - ia_0^m - i \displaystyle\sum_{k=1}^{m} \dfrac{a_k^m(-\omega)}{-\omega + d_k^m}}, \qquad (3.13)$$

where $\omega \in \mathcal{R}$ is again the Fourier-dual of t. The main difference with the Di Menza-Bruneau work is that Szeftel does not impose interpolation but only approximation.

The same idea of approximating the square root symbol by a rational function was also presented by Shibata [118] (linear approximation with two intersection points to choose) and Kuska [82] (1/1-Padé approximation about some dominant frequency ω_0 to choose). However, their subsequent discretizations (based on finite differences) are less systematic than in the papers [27, 40, 126]. Due to the low approximation order the numerical results are also inferior.

3.3.2 Approach of Fevens and Jiang

In [59] Fevens and Jiang propose the following family of ABCs:

$$\prod_{l=1}^{m}\left(i\frac{\partial}{\partial x}+a_l\right)u=0, \tag{3.14}$$

for any $m\in\mathbb{N}$. For the right BC all wave numbers a_l can be chosen arbitrarily positive (and negative for the left BC). From the shape $u=e^{i(kx-\omega t)}$ of a plane wave one sees that all waves with a wavenumber $k=a_l$ are perfectly absorbed at the boundary. The well-posedness for this class of (continuous) ABCs is established in [59].

Next we shall compare this approach to the rational approximations (cf. Section 3.3.1) of the dispersion relation of the Schrödinger equation (in the right exterior domain):

$$k=\sqrt[+]{\omega-V_r}. \tag{3.15}$$

Using the correspondence $i\partial_x\leftrightarrow-k$ in (3.14), along with $k^2=\omega-V_r$ for the even powers of k yields a (real valued) rational approximation to (3.15):

$$k=R(\omega).$$

With the low order choices $m=2$ or $m=3;a_1=a_2=a_3$ one recovers, respectively, the ABCs of Shibata [118] and of Kuska [82].

3.3.3 Approach of Alonso-Mallo and Reguera

Alonso-Mallo and Reguera [4, Section 2] extended the rational approximation of Section 3.3.1 for $\sqrt[+]{i\omega}$ to interpolating rational functions $q(z)=P_l(z)/Q_m(z)$. Here, P_l, Q_m are relatively prime polynomials of degree l and m respectively, such that $\sqrt[+]{z}$ is interpolated at $l+m+1$ nodes. This class of ABCs includes many of the previous ABCs from the literature (like [59,82,118]). However, for such continuous ABCs the authors of [4] showed that the resulting IBVP can only be well-posed if either $l=m$ or $l=m+1$. But the spatial semi-discretization may then still be weakly ill-posed, with increasing instabilities for higher order ABCs. In [5,7] Alonso-Mallo and Reguera considered the analogous rational approximations (switching here from $i\omega$ to s) for the square root function (2.34) of the spatially discrete TBC (2.35) written as:

$$r(\eta;\Delta x)=1-\frac{\Delta x^2}{2}\eta+\sqrt[+]{\frac{\Delta x^2}{2}\eta\left(\frac{\Delta x^2}{2}\eta-2\right)} \tag{3.16}$$

with the abbreviation $\eta=is-V_r$. In [4,6] $\chi^{-1}(s)$ in the TBCs (2.36) and (2.37) is approximated by a rational function. This reduces the evaluation of the convolution to solving ordinary differential equations (cf. (3.11)). Their *semi-discrete ABC of order* (l,m) has the form

$$r(\eta;\Delta x)\approx q(\eta;\Delta x)=\frac{P_l(\eta;\Delta x)}{Q_m(\eta;\Delta x)}. \tag{3.17}$$

Typically, it yields a higher absorption quality than the spatial discretization (by finite differences) of the continuous ABC in [4, Section 2].

If the dominant group velocity (or discrete wavenumber $\bar{\kappa}$) of the solution is known, then it is possible to choose the interpolatory nodes, such that a good absorption is achieved. This will now be explained for the right semi-discrete ABC of order (2,1):

$$\alpha_0 u_{J-1}(t) + \alpha_1 \frac{d}{dt} u_{J-1}(t) = \alpha_2 u_J(t) + \alpha_3 \frac{d}{dt} u_J(t) + \alpha_4 \frac{d^2}{dt^2} u_J(t), \tag{3.18}$$

with coefficients α_k depending on Δx and the four interpolatory nodes η_k, $k=1,\cdots,4$. The strategy is to choose the nodes such that $r(-\omega-V_r;\Delta x)-q(-\omega-V_r,\Delta x)$ is small when $\omega=\omega(\bar{\kappa})$, where $\omega(\kappa)$ is given by the dispersion relation

$$\omega(\kappa) = \frac{2(\cos\kappa-1)}{\Delta x^2} - V_r, \tag{3.19}$$

for the plane wave solution

$$u_j(t) = \exp\big(i(\kappa j + \omega(\kappa)t)\big), \quad j \in \mathbb{Z}. \tag{3.20}$$

If one of the nodes is chosen as $\eta_k = 2(1-\cos(\bar{\kappa}))/\Delta x^2$, then the plane wave (3.20) will clearly be totally absorbed [5].

The fully discrete problem of Alonso-Mallo and Reguera [5] (using an A-stable implicit Runge-Kutta method for the time integration) is still weakly unstable, with *increasing instabilities for higher order ABCs*.

3.4 Approximations of the convolution kernel by sums of exponentials

The transparent boundary conditions from Sections 2 and 3.2 are convolutions in time, either on a continuous level or on a time-discrete level. In order to obtain approximate TBCs that are local in time the convolution kernel is approximated by a sum of exponentials.

These approximations of the convolution kernel by sums of exponentials correspond to rational approximations of the Laplace transform of the kernel (cf. Section 3.3).

The transparent boundary conditions in (2.10) and (2.37) are convolutions of the Neumann data at the boundary with some kernel f

$$(f*\partial_\mathbf{n} u)(t) = \int_0^t f(t-\tau)\partial_\mathbf{n} u(\tau)d\tau. \tag{3.21}$$

For the continuous TBC the kernel function is

$$f(t) = \mathcal{L}^{-1}\left(\frac{1}{\sqrt{\cdot}}\right)(t) = \frac{1}{\sqrt{\pi t}},$$

while for the spatially discrete TBC the kernel function is

$$f(t) = \mathcal{L}^{-1}\left(\frac{1}{\hat{\chi}^{-1} - 1}\right)(t),$$

with χ given in (2.34). The TBCs in (2.8) and (2.36) are convolutions of the Dirichlet data $u(t)$ at the boundary with kernel functions

$$f(t) = \sqrt{t} \quad \text{and} \quad f(t) = \mathcal{L}^{-1}\left(\hat{\chi}^{-1} - 1\right)(t),$$

respectively. The time discretizations yield discrete convolutions

$$\sum_{k=1}^{n} w_{n-k} u^k$$

of the solution with convolution weights w_k. The weights are γ_k (3.8), $\tilde{\ell}_k$ (3.5), s_k (2.47), ψ_k (2.24), or $\hat{\psi}_k$ (2.27). The numerical effort to evaluate the convolution at time step t_n is $\mathcal{O}(n)$. Thus a naive implementation to evaluate the discrete convolution for $n = 1, \cdots, N$ is $\mathcal{O}(N^2)$, which can become prohibitive. In [70] Hairer, Lubich, and Schlichte developed a method to overcome this $\mathcal{O}(N^2)$ operation count, and reduced it to $\mathcal{O}(N(\log(N))^2)$ using FFT. However, the storage requirement is not reduced, it is still $\mathcal{O}(N)$.

3.4.1 Sum-of-exponential approximation of discrete convolution kernel

Using the discrete TBC (2.47) for calculations avoids any boundary reflections and it renders the fully discrete scheme unconditionally stable (just like the underlying Crank-Nicolson scheme). An approach to approximate the discrete convolution (2.47) allowing for a fast evaluation consists in approximating the kernel (2.48) by a finite sum (say m terms) of exponentials that *decay* with respect to time (cf. [18]). With this approximated kernel, the convolution can now be evaluated with a simple recurrence formula for m auxiliary terms and the numerical effort now stays constant in time. On the Laplace-transformed level this approximation amounts to replace the symbol $\hat{s}(z)$ of the convolution (cf. (2.45)) by a rational approximation. This approach hence resembles the methods of Section 3.3 — but on a time-discrete level. Such kind of trick has been proposed in [65] for the heat equation and in [120] for the continuous TBC in case of the 3D wave equation, and developed in [2, 38, 67, 121, 122] for various hyperbolic problems.

3.4.2 Local approximations — fast and oblivious convolution

In [93, 110] a fast and oblivious convolution algorithm is developed that allows to evaluate convolutions of the form (3.21). For equally spaced t_n, $n = 0, 1, \cdots, N$, the algorithm evaluates the convolution with $\mathcal{O}(N \log(N))$ operations requiring $\mathcal{O}(\log(N))$ memory. It requires $\mathcal{O}(\log(N))$ evaluations of the Laplace transform of the kernel and no evaluation of the kernel function f itself. The convolution integral from 0 to t is split as

$$\int_0^t f(t-\tau)u(\tau)d\tau = \sum_{\ell=1}^{L} \int_{t_{\ell-1}}^{t_\ell} f(t-\tau)u(\tau)d\tau,$$

where the t_ℓ are such that $[t-t_\ell,t-t_{\ell-1}] \subset [B^{\ell-1}\Delta t, 2B^\ell \Delta t]$ for some $B \geq 2$. For each ℓ a contour Γ_ℓ is chosen for the numerical inversion of the Laplace transform. Contour integrals are discretized using the trapezoidal rule:

$$\int_{t_{\ell-1}}^{t_\ell} f(t-\tau)u(\tau)d\tau = \int_{\Gamma_\ell} F(\lambda) \int_{t_{\ell-1}}^{t_\ell} e^{\lambda(t-\tau)}u(\tau)d\tau d\lambda$$

$$\approx \sum_{k=-K}^{K} F(\lambda_k)e^{\lambda_k(t-t_\ell)} \int_{t_{\ell-1}}^{t_\ell} e^{\lambda_k(t_\ell-\tau)}u(\tau)d\tau. \tag{3.22}$$

The values $t-\tau$ in (3.22), for $t_{\ell-1} \leq \tau \leq t_\ell$ lie in the approximation interval $[B^{\ell-1}\Delta t, 2B^\ell \Delta t]$. The length of this interval increases geometrically, whereas the ratio of its end-points is bounded by $2B$. In [90] it is explained how to choose Γ_ℓ, such that the error in the approximation (3.22) is $\mathcal{O}(\exp(-cK))$ independently of ℓ. The integral in (3.22)

$$\int_{t_{\ell-1}}^{t_\ell} e^{\lambda_k(t_\ell-\tau)}u(\tau)d\tau$$

is the solution $y(t_\ell)$ of the ordinary differential equation

$$y'(t)=\lambda_k y(t)+u(t), \quad y(t_{\ell-1})=0, \tag{3.23}$$

which is solved numerically. Instead of keeping the past values of $u(j\Delta t)$, $j=0,\cdots,n$ at the boundary, the solutions of (3.23) are kept. Only $L=\mathcal{O}(\log(N))$ different contours are required, each with a fixed number of quadrature nodes λ_k, $k=-K,\cdots,K$. This reduces the active memory to $\mathcal{O}(L)$. Thus the kernel is approximated *locally* by sums of exponentials $e^{\lambda_k t}$ including terms with $\text{Re}(\lambda_k)>0$, i.e., *not decaying* with respect to time. This approach allows to maintain a uniform relative approximation error of the convolution kernel.

3.4.3 Approximation of Jiang and Greengard

In [78] Jiang and Greengard derived a fast evaluation algorithm for the TBC of the Schrö-dinger equation which is a convolution in time with the singular kernel $1/\sqrt{\pi t}$. This approach was first developed by Greengard and Strain [65] for the heat kernel. Jiang and Greengard first split the convolution integral (2.1) or (2.10) into the *history part* $\int_0^{t-\Delta t}$ and the *local part* $\int_{t-\Delta t}^{t}$. The second term involves the singular part of the convolution and it is approximated directly using linear interpolation and "product integration" techniques [78, Lemma 9] suitable for square root singularities.

For the history part the kernel is approximated by a sum of exponentials, finally allowing for a recursive evaluation of the convolution (similar to Section 3.4.1). The standard formula

$$\mathcal{L}^{-1}\left(\frac{1}{\sqrt{\cdot}}\right)(t) = \frac{1}{\sqrt{\pi t}} = \frac{2}{\pi}\int_0^\infty e^{-s^2 t}ds \tag{3.24}$$

yields a representation of the integral kernel with infinitely many exponentials. Truncating the lower limit of this integral (3.24) at $t = p$ yields an *error bound* [78, Lemma 4]:

$$\left| \frac{2}{\pi} \int_p^\infty e^{-s^2 t} ds \right| = \frac{e^{-p^2 \Delta t}}{\sqrt{\pi t}}, \tag{3.25}$$

since $t \geq \Delta t > 0$ for the history term. For a fixed time step Δt this error of the history part can be made arbitrary small by choosing p sufficiently large. For the discretization of the history part, the integral (3.24) on $[0,p]$, a high-order Gauß-Legendre quadrature on a dyadic splitting of the interval $[0,2^j]$, cf. [78, Lemmas 5 and 6] is used, yielding a superposition of the exponentials.

As an advantage, this method is flexible; it can be coupled to an arbitrary interior discretization for the Schrödinger equation. Moreover, this approach can be generalized to higher-dimensional problems [77, 79].

3.5 The perfectly matched layer method

The perfectly matched layer method (PML) was invented by Bérenger [23] in 1994 as an absorbing boundary conditions for Maxwell's equations. Immediately it was realized by Chew and Weedon in [32] that it can be interpreted as a complex coordinate stretching. Collino [34] adapted the PML method to the paraxial wave equation. Later on, in [1, 88] the PML method using the complex coordinate stretching technique was generalized to more complicated settings. The Bérenger technique was applied by Zheng [133] to linear and nonlinear Schrödinger equations. Let us note that a brief construction of the PML for the Schrödinger equation can be found in [68, Section 3.3].

As the exterior domain is homogeneous, the $\mathcal{Z}$-transformed solution $\hat{u}(x,z)$ of (2.19) is analytic for $x \leq x_l$ and $x \geq x_r$, and $\hat{u}(x,z)$ has an analytic extension to the half planes $\operatorname{Re} x < x_l$, $\operatorname{Re} x > x_r$. We define

$$\gamma(x) := \begin{cases} x_l + (1+i\sigma)(x-x_l) & \text{for } x \leq x_l, \\ x & \text{for } x_l < x < x_r, \\ x_r + (1+i\sigma)(x-x_r) & \text{for } x \geq x_r, \end{cases}$$

and $\hat{u}_B(x) := \hat{u}(\gamma(x),z)$, with the damping factor $\sigma = 1$. Other choices of $\gamma(x)$ are possible and frequently used. Again $\hat{u}_B$ is decomposed as $\hat{v}_B \oplus \hat{w}_B$ according to the splitting into an interior and exterior domain problem. Note that $\hat{v}_B$ coincides with $\hat{v}$ by definition. The interface conditions are $\hat{v}_B(x_{l,r},z) = \hat{w}_B(x_{l,r},z)$ and $\partial_{\mathbf{n}}\hat{v}_B(x_{l,r},z) = -\partial_{\mathbf{n}}\hat{w}_B(x_{l,r},z)/\gamma'$. Here, $\gamma' = \pm(1+i\sigma)$ denotes the right-hand derivative of γ at x_l (and vice-versa at x_r). $\hat{v}_B$ and

$\hat{w}_B$ are the solutions of the following coupled BVP

$$
\begin{aligned}
&i\frac{\delta(z)}{\Delta t}\hat{v}_B = -\partial_x^2\hat{v}_B + V\hat{v}_B + f, \quad x \in [x_l, x_r], \\
&\partial_{\mathbf{n}}\hat{v}_B(x_{l,r}) = -\partial_{\mathbf{n}}\hat{w}_B(x_{l,r})/\gamma',
\end{aligned}
\tag{3.26}
$$

$$
\begin{aligned}
&i\frac{\delta(z)}{\Delta t}\hat{w}_B = -\frac{1}{(\gamma')^2}\partial_x^2\hat{w}_B + V_{l,r}\hat{w}_B, \quad x \in \Omega_l \cup \Omega_r, \\
&\hat{w}_B(x_{l,r}) = \hat{v}_B(x_{l,r}), \\
&\lim_{|x|\to\infty}\hat{w}_B = 0,
\end{aligned}
\tag{3.27}
$$

where the inhomogeneity $f = f[u^I, u^1, \cdots, u^{K-1}]$ depends on the K initial values of the multi-step method. The two fundamental solutions of (3.27) are

$$
\exp\left(i\gamma' \sqrt[+]{i\frac{\delta(z)}{\Delta t} - V_{l,r}}x\right) \quad \text{and} \quad \exp\left(-i\gamma' \sqrt[+]{i\frac{\delta(z)}{\Delta t} - V_{l,r}}x\right).
$$

In case of the trapezoidal rule approximation the real part of $\delta(z)/\Delta t$ is positive. Thus the square root term takes values in the first quadrant. Multiplying by $\gamma' = -i(1+i\sigma)$, we find that the second fundamental solution decays exponentially fast, while the first explodes exponentially. What is required now is some condition to eliminate the first fundamental solution. By imposing a homogeneous Dirichlet boundary condition at some distance from the boundary, the portion of the first fundamental solution in our solution can be made small. Thus we expect to obtain a reasonable approximation when replacing $\hat{w}_B$ in (3.26) by $\hat{w}_{PML}$ obtained from

$$
\begin{aligned}
&i\frac{\delta(z)}{\Delta t}\hat{w}_{PML} = -\frac{1}{(\gamma')^2}\partial_x^2\hat{w}_{PML} + V_{l,r}\hat{w}_{PML}, \quad x \in \widetilde{\Omega}_l \cup \widetilde{\Omega}_r, \\
&\hat{w}_{PML}(x_{l,r}) = \hat{v}_{PML}(x_{l,r}), \\
&\hat{w}_{PML}(x_{l,r} \pm \rho) = 0,
\end{aligned}
\tag{3.28}
$$

where $\widetilde{\Omega}_l = [x_l - \rho, x_l]$ and $\widetilde{\Omega}_r = [x_r, x_r + \rho]$ are the left and right layers, with a sufficiently large $\rho > 0$. With increasing thickness ρ of the layer the cut-off error gets exponentially small. As pointed out by Hagstrom in [68, Section 3.3], Eq. (3.28) can be interpreted in the following way: the system is simply made parabolic in the layer but increasing the damping factor σ corresponds to decreasing the diffusion coefficient which might lead to a boundary layer at the interface.

The PML method is temporally discrete. Reflections do not occur due to the complex coordinate transformation, but only due to the cut-off error introduced by replacing (3.27) by (3.28).

For completeness we include in the sequel a description of the PML algorithm.

The PML algorithm

Following an idea presented for the Helmholtz equation in [111, 137] we take

$$\gamma(x) = x_{l,r} + (1+i)(x - x_{l,r}) \quad \text{for } x \leq x_l \text{ and } x \geq x_r.$$

Then we adapt ρ and the spatial discretization inside the PML layer according to the pseudocode in Table 1. There, dx is the mesh width in the interior domain, eps is the expected error resulting from the interior discretization, $\lambda_{\texttt{max}}$ and $\lambda_{\texttt{min}}$ are the maximal and minimal wavelengths present in the problem. Note that the expected error eps can be deduced from the mesh width and minimal wavelength. From the algorithm a vector xi is obtained such that the mesh points in the right layer are given by $x_r + \texttt{xi(n)}$.

Table 1: Generating the PML.

```
let xi(1)=dx
n=1
dpml=dx
while −log(eps)/xi(n)>2∗π/λ_max do
      dpml=min(−2∗π∗xi(n)∗dx/log(eps)/λ_min,1.6∗dpml)
      xi(n+1)=xi(n)+max(dx,dpml)
      if xi(n+1)>1/eps
         return
      else
         n=n+1
      end
end while
```

The motivation for this choice of the PML is as follows. Suppose we have a minimal wavelength $\lambda_{\texttt{min}}$ in the interior. The corresponding wavenumber is $\kappa = 2\pi/\lambda_{\texttt{min}}$ and by the complex continuation this wave is damped by the factor $\exp(-\kappa\xi)$, where ξ is the distance from the boundary $x_{l,r}$. Introducing the function

$$\kappa_{\texttt{co},\epsilon}(\xi) = -\log(\epsilon)/\xi,$$

then we have for $\kappa > \kappa_{\texttt{co},\epsilon}$ and for $\xi > \xi'$ that waves are damped by a factor smaller than ϵ:

$$e^{-\kappa\xi} < e^{-\kappa_{\texttt{co},\epsilon}(\xi)\xi} = e^{\ln(\epsilon)} = \epsilon.$$

If this damping is sufficient, then for $\xi > \xi'$ only longer waves with wave lengths $2\pi/\kappa > 2\pi/\kappa_{\texttt{co},\epsilon}(\xi')$ need to be approximated for distances $\xi > \xi'$. As this approximation should be done with the same accuracy and as the accuracy is essentially determined by the

number of points per wave length, $\lambda_{\mathtt{min}}/\Delta x$, we are led to the *a priori* determination of the local mesh-width $\Delta x(\xi) = 2\pi/\kappa_{\mathtt{co},\epsilon}(\xi)$. Furthermore it is not sensible to take the local mesh-width in the PML smaller than in the interior. Also the mesh in the exterior should not become too anisotropic, therefore the local mesh-width `dpml` is bounded from below by `dx` and from above by 1.6 times the old mesh-width.

3.6 Approximations based on the pole condition

For the pole condition of Section 2.2, the analyticity of a function $W(q,s)$ for q in some half plane has to be verified. Numerically this is realized by the following technique. E.g. for $q_0 = -1+i$ the *Möbius transformation*

$$q \mapsto \tilde{q}(q) = \frac{q+q_0}{q-q_0} \tag{3.29}$$

maps the half plane below the bisecting line of the first and third quadrant to the unit disk. Thus, in the transformed variable $\tilde{q}$, W has to be analytic on the unit disk. This justifies the ansatz

$$W(q(\tilde{q}),s) = \tilde{W}(\tilde{q}) = \sum_{n=0}^{\infty} \hat{a}_n(s)\tilde{q}^n. \tag{3.30}$$

In the variable $\tilde{q}$ (2.15) reads

$$is\tilde{W}(\tilde{q},s) + \left(q_0\frac{\tilde{q}+1}{\tilde{q}-1}\right)^2 \tilde{W}(\tilde{q},s) - q_0\frac{\tilde{q}+1}{\tilde{q}-1}\hat{w}(x_r,s) - \partial_x\hat{w}(x_r,s) = V_r\tilde{W}(\tilde{q},s).$$

Multiplying by $(\tilde{q}-1)^2$, plugging in the ansatz (3.30), sorting for powers of $\tilde{q}$, comparing the coefficients and truncating the power series (3.30), yields the following equations for the coefficients $\hat{a}_n(s)$:

$$(is+q_0^2-V_r)\hat{a}_0 + q_0\hat{w}(x_r,s) - \partial_x\hat{w}(x_r,s) = 0,$$
$$4q_0^2\hat{a}_0 + (is+q_0^2-V_r)\hat{a}_1 + 2q_0\hat{w}(x_r,s) = 0,$$
$$4q_0^2\hat{a}_0 + (-is+3q_0^2+V_r)\hat{a}_1 + (is+q_0^2-V_r)\hat{a}_2 = 0,$$
$$(is+q_0^2-V_r)\hat{a}_k + (-2is+2q_0^2+2V_r)\hat{a}_{k-1} + (is+q_0^2-V_r)\hat{a}_{k-2} = 0.$$

Transforming back to time-domain one obtains a system of ODEs for the $a_n(t)$ that is coupled to the Dirichlet and Neumann data of the interior problem. Details can be found in [106,115]. Actually, the optimal choice of q_0 would be $i\sqrt{is-V_r}$, since this decouples the equations for the $a_n(t)$ yielding the continuous TBC. In practice, to avoid the evaluation of the pseudodifferential operator $\sqrt{i\partial_t - V_r}$, one rather uses $q_0 = (-1+i)\sqrt{\kappa}$ for some dominant frequency κ.

4   Extensions to two space dimensions

We have seen in the previous sections that many different approaches can be adopted for approximating the transparent boundary condition (TBC) involved in the one-dimensional case. The linear two-dimensional problem is much more complicated because the artificial boundary may have a quite general geometry. At this step and unlike the one-dimensional case, a strategy must be chosen to build the TBC or an approximation of this condition. In this situation, the exact TBC is a non-local pseudodifferential operator both in space and time. Therefore, even from the numerical point of view, the choice of the boundary condition plays an important role in the future approximation and algorithmic developments.

The next challenge is the numerical approximation. Like the one-dimensional case, accuracy and stability questions arise as well as the construction of fast algorithms to evaluate the different operators which must be approximated.

The aim of this section is to review the current developments regarding the above objectives.

4.1   Continuous transparent boundary conditions

A first approach to derive a continuous TBC set on a general artificial surface is outlined in [109]. Let us consider the 2D Schrödinger equation without potential

$$
\begin{aligned}
i\partial_t u + \Delta u &= 0, \quad (\mathbf{x},t) \in \mathcal{R}^2 \times \mathcal{R}^+, \\
u(\mathbf{x},0) &= u^I(\mathbf{x}), \quad \mathbf{x} \in \mathcal{R}^2.
\end{aligned}
\tag{4.1}
$$

As a first step one introduces an artificial boundary Γ cutting $\mathcal{R}^2$ into two non-overlapping parts: a bounded computational domain denoted by Ω (with boundary Γ) and its unbounded complement $\Omega^{\text{ext}} := \mathcal{R}^2 \backslash \overline{\Omega}$. Moreover, we assume that the initial data u^I is compactly supported in Ω. Similarly to Section 2.1, we can split problem (4.1) as a *transmission problem* between the two sub-domains Ω and Ω^{ext} using the field decomposition $L^2(\mathcal{R}^2) = L^2(\Omega) \oplus L^2(\Omega^{\text{ext}})$:

$$
\begin{cases}
i\partial_t v + \Delta v = 0, \quad (\mathbf{x},t) \in \Omega \times \mathcal{R}^+, \\
v(\mathbf{x},0) = u^I(\mathbf{x}), \quad \mathbf{x} \in \Omega, \\
v(\mathbf{x},t) = w(\mathbf{x},t), \quad (\mathbf{x},t) \in \Gamma \times \mathcal{R}^+,
\end{cases}
\tag{4.1a}
$$

and

$$
\begin{cases}
i\partial_t w + \Delta w = 0, \quad (\mathbf{x},t) \in \Omega^{\text{ext}} \times \mathcal{R}^+, \\
\partial_{\mathbf{n}} w(\mathbf{x},t) = \partial_{\mathbf{n}} v(\mathbf{x},t), \quad (\mathbf{x},t) \in \Gamma, \\
\lim_{|\mathbf{x}| \to +\infty} \sqrt{|\mathbf{x}|} \left(\nabla w \cdot \dfrac{\mathbf{x}}{|\mathbf{x}|} + e^{-i\frac{\pi}{4}} \partial_t^{\frac{1}{2}} w \right) = 0, \\
w(\mathbf{x},0) = 0, \quad \mathbf{x} \in \Omega^{\text{ext}}.
\end{cases}
\tag{4.2}
$$

Here, **n** is the outwardly directed unit normal vector to Γ. The *Sommerfeld-like radiation condition* is added to assure the uniqueness of the solution to the exterior problem and is classical for wave-like scattering problems.

As a second step we solve the exterior problem (4.2) in the time-Laplace domain by an integral equation formulation. In the sequel $\hat{v}$ and $\hat{w}$ shall denote the Laplace transform of the functions v and w, respectively. Then, (4.2) is reformulated as a Helmholtz-like equation for the wave field $\hat{w}$:

$$
\begin{aligned}
&(\Delta+k^2)\hat{w}(\mathbf{x},s)=0, \quad \mathbf{x}\in\Omega^{\text{ext}}, \\
&\partial_{\mathbf{n}}\hat{w}(\mathbf{x},s)=\partial_{\mathbf{n}}\hat{v}(\mathbf{x},s), \quad (\mathbf{x},s)\in\Gamma, \\
&\lim_{|\mathbf{x}|\to+\infty}\sqrt{|\mathbf{x}|}\left(\nabla\hat{w}(\mathbf{x},s)\cdot\frac{\mathbf{x}}{|\mathbf{x}|}-ik\hat{w}(\mathbf{x},s)\right)=0.
\end{aligned} \tag{4.3}
$$

The wave number k is defined by $k=\sqrt{is}$, with $\text{Re}(k)>0$. According to the theory of potential for the 2D Helmholtz equation [36], the Helmholtz integral representation formula of the exterior field is a superposition of the single- and double-layer potentials applied, respectively, to the trace and to the normal derivative of $\hat{w}$ on Γ. Making use of the trace theorems for these two potentials and using the Neumann data of problem (4.3), the integral representation of $\hat{w}$ on Γ reads

$$
\left(\frac{1}{2}I-M\right)\hat{w}(\mathbf{x},s)=L\partial_{\mathbf{n}}\hat{w}, \quad \mathbf{x}\in\Gamma.
$$

Here, I is the identity operator, L is the single-layer potential defined by

$$
L\varphi(\mathbf{x})=-\int_{\Gamma}G(\mathbf{x},\mathbf{y})\varphi(\mathbf{y})d\Gamma(\mathbf{y}), \quad \mathbf{x}\in\Gamma,
$$

and M is the double-layer potential given by

$$
M\varphi(\mathbf{x})=\int_{\Gamma}\partial_{\mathbf{n}}G(\mathbf{x},\mathbf{y})\varphi(\mathbf{y})d\Gamma(\mathbf{y}), \quad \mathbf{x}\in\Gamma,
$$

for a surface density φ. $G(\mathbf{x},\mathbf{y})=\frac{i}{4}H_0^{(1)}(k|\mathbf{x}-\mathbf{y}|)$ is the free-space Green kernel associated with the 2D Helmholtz operator. Transforming back to time-domain by using an inverse Laplace transform and the Dirichlet data from (4.1a) yields the following Dirichlet-to-Neumann map

$$
\partial_{\mathbf{n}}v=\mathcal{L}^{-1}\left(L^{-1}\left(\frac{1}{2}I-M\right)\hat{v}(\mathbf{x},\cdot)\right)(t), \quad \mathbf{x}\in\Gamma, \tag{4.4}
$$

and the Neumann-to-Dirichlet map

$$
v(\mathbf{x},t)=\mathcal{L}^{-1}\left(\left(\frac{1}{2}I-M\right)^{-1}L\partial_{\mathbf{n}}\hat{v}(\mathbf{x},\cdot)\right)(t), \quad \mathbf{x}\in\Gamma. \tag{4.5}
$$

Although (4.5) was already derived in [109], apparently it has not been used as a continuous exact boundary condition. Indeed, in [109, Section3], the author rather uses a time semi-discrete version of this condition in the special case of a circular boundary. This formulation of the exact Dirichlet-to-Neumann map is a composition of an inverse Laplace transform and spatial integral operators. As a consequence, numerically evaluating such an operator in a stable way is very difficult and costly (also in terms of memory requirements).

4.2 Continuous transparent and artificial boundary conditions

The previous derivation shows that there exists a close relation between the derivation of boundary conditions for the 2D Schrödinger equation and the Helmholtz equation after the application of a Laplace transform in the time-domain. This point of view has given rise to different adaptations of results available for the Helmholtz equation to Schrödinger equations.

One of the most popular techniques for the derivation of artificial boundary conditions for wave-like equations is based on the pioneering work of Engquist and Majda [57,58]. This approach leads to families of approximate (non-local and local) artificial boundary conditions for variable coefficients scalar equations and systems. One of its defects is that these conditions are not exact. On top of this loss of accuracy, stability of the resulting IBVP has to be checked on a case-to-case basis. We shall now review the results from this approach obtained for 2D Schrödinger equations. We present the following three cases with increasing numerical difficulties: a straight boundary, a circular boundary, and finally a generally curved and smooth convex boundary.

4.2.1 Straight artificial boundary

Let $\Omega = \mathcal{R}^+ \times \mathcal{R}$ be the right half-space. The artificial boundary is then $\Gamma = \{\mathbf{x} \in \mathcal{R}^2 | x_1 = 0\}$. We consider the IBVP

$$
\begin{cases}
(i\partial_t + \Delta)u = 0, & (\mathbf{x}, t) \in \Omega \times \mathcal{R}^+, \\
u(\mathbf{x}, 0) = u^I(\mathbf{x}), & \forall \mathbf{x} \in \Omega,
\end{cases}
\tag{4.6}
$$

and the initial data u^I is assumed to be compactly supported in Ω. For the construction of the exact or transparent BC we require that the restriction of the $\mathcal{R}^2$-Schrödinger solution to the right half-space coincides with the solution of (4.6) complemented with the exact BC. We apply the Laplace transform in time (with dual variable s) and the Fourier transform $\mathcal{F}$ in the x_2-direction (with dual variable ξ). This yields the following differential equation in the normal variable x_1 for the solution w of the Schrödinger equation in the left half-plane

$$
\left(\partial_{x_1}^2 + is - \xi^2\right)\mathcal{F}\hat{w}(x_1, \xi, s) = 0, \quad x_1 < 0,
\tag{4.7}
$$

where $\hat{w}$ is the Laplace transform of w. The solution to this homogeneous (elliptic or Helmholtz-type) differential equation (4.7) is given as the superposition of two waves

$$\mathcal{F}\hat{w}(x_1,\xi,s) = A^+(\xi,s)e^{i\lambda_1^+(\xi,s)x_1} + A^-(\xi,s)e^{i\lambda_1^-(\xi,s)x_1},$$

with $\lambda_1^\pm(\xi,s) = \mp\sqrt{is-\xi^2}$. If the point (x_2,t,ξ,ρ) lies in the *anisotropic M-cone*

$$\mathcal{E} := \left\{(x_2,t,\xi,\rho) \in \mathcal{R}^4, \rho+\xi^2 > 0\right\},$$

with $\rho = \text{Im}(s)$ and $\text{Re}(s) > 0$, then one can write the symbols $\lambda_1^\pm$ such that $\text{Im}(\lambda_1^\pm) = \mp\Psi(\xi,s)$, where $\Psi(\xi,s) = \text{Re}(s)/(\sqrt{2(-(\rho+\xi^2)+D)})$, setting $D = \sqrt{(\rho+\xi^2)^2+\text{Re}(s)^2}$. The function Ψ is strictly positive and smooth on $\mathcal{E}$. As a consequence, in order for $\mathcal{F}\hat{w}(.,\xi,s) \in L^2(\mathcal{R}^-)$ to hold, we require $A^- = 0$, and hence

$$\mathcal{F}\hat{w}(x_1,\xi,s) = A^+(\xi,s)e^{i\lambda_1^+(\xi,s)x_1}. \tag{4.8}$$

The part of the wave $\hat{w}$ at point (x_2,t,ξ,ρ) in $\mathcal{E}$ is exponentially decaying (as $x_1 \to -\infty$) and usually called *evanescent*. This zone is called the *M-quasi elliptic region* setting $M=(1,2)$ [8] using the notations introduced by Lascar [84]. The pair M is introduced to recall the different homogeneities of the dual variables s and ξ in the symbols $\lambda_1^\pm$ [8,84]. The points (x_2,t,ξ,ρ) in the cone

$$\mathcal{H} = \left\{(x_2,t,\xi,\rho), \rho+\xi^2 < 0\right\}$$

represent the propagative part of the wave. This zone is referred to as the *M-quasi hyperbolic part*. Finally, the complementary zone

$$\mathcal{G} = \left\{(x_2,t,\xi,\rho), \rho+\xi^2 = 0\right\}$$

corresponds to the rays propagating along the boundary (grazing waves). This region is called the *M-quasi glancing zone*. It is reduced to $\{(0,0,0,0)\}$ if the wave u is not tangentially incident to Γ.

   The exact boundary condition is easily deduced by applying the normal derivative operator ∂_{x_1} to (4.8) and choosing $x_1=0$, $\mathbf{n}=(-1,0)$ as the outwardly unit normal vector to the computational domain. The inverse Laplace-Fourier transform then yields

$$\partial_{\mathbf{n}}u + i\widetilde{\Lambda^+}(\partial_{x_2},\partial_t)u = 0, \quad \text{on } \Gamma \times \mathcal{R}^+, \tag{4.9}$$

with

$$\widetilde{\Lambda^+}(\partial_{x_2},\partial_t)w(0,x_2,t) = \frac{1}{(2\pi)^2 i}\int_{\gamma-i\infty}^{\gamma+i\infty}\int_{\mathcal{R}}\lambda_1^+(\xi,s)\mathcal{F}\hat{w}(0,\xi,s)e^{i\xi x_2+st}d\xi ds,$$

cf. [8]. Formally, this TBC operator may be written as

$$\widetilde{\Lambda^+}(\partial_{x_2},\partial_t) = -\sqrt{i\partial_t+\Delta_\Gamma} = e^{-3i\pi/4}\sqrt{\partial_t+(e^{-i\pi/4}\partial_{x_2})^2},$$

where Δ_Γ denotes the *surface Laplace-Beltrami operator* $\partial_{x_2}^2$. The TBC operator is defined as the square root of a surface Schrödinger operator on $\Gamma \times \mathcal{R}^+$ which is therefore *non-local* both in space and time.

¿From a numerical point of view, its implementation is computationally expensive and not obvious.

A way to obtain approximations of the TBC (4.9) is to consider that we are mostly interested in characterizing the high temporal frequencies of the wave field (since those wave components travel the fastest). This means that we assume that the only frequencies of interest are contained in $\mathcal{H}$ and satisfy the *high frequency assumption*: $|s|$ is large compared to ξ^2. The important point of this hypothesis is that local approximations of the symbol λ_1^+ w.r.t. the small parameter $\xi^2/|s|$ can be derived. In [15], Arnold proposed a first and second-order Taylor expansion of the symbol λ_1^+. The author obtains the following two artificial boundary conditions

$$(\partial_\mathbf{n} + e^{-i\pi/4}\partial_t^{\frac{1}{2}})u = 0, \quad \text{on } \Gamma \times \mathcal{R}^+, \tag{4.10}$$

and

$$(\partial_\mathbf{n} + e^{-i\pi/4}\partial_t^{\frac{1}{2}} - e^{i\pi/4}\frac{1}{2}\Delta_\Gamma I_t^{\frac{1}{2}})u = 0, \quad \text{on } \Gamma \times \mathcal{R}^+. \tag{4.11}$$

We remark that the exact solution u is hence approximated by another solution that we keep on denoting by u, for simplicity. Like in the one-dimensional case, $\partial_t^{1/2}$ and $I_t^{1/2}$ respectively denote the fractional derivative and integral operators of half-order

$$\partial_t^{\frac{1}{2}}\psi(t) = \frac{1}{\sqrt{\pi}}\frac{d}{dt}\int_0^t \frac{\psi(s)}{\sqrt{t-s}}ds, \quad I_t^{\frac{1}{2}}\psi(t) = \frac{1}{\sqrt{\pi}}\int_0^t \frac{\psi(s)}{\sqrt{t-s}}ds. \tag{4.12}$$

Although they are still non-local in time, these two approximate boundary conditions (also called *artificial* boundary conditions) are local in space. This is an important feature in numerical simulations since the sparse structure of the linear system arising from a finite-difference or finite-element approximation is preserved [12]. Indeed, the non-locality in time only appears in the inhomogeneity of the linear system, and any fast scheme developed for the one-dimensional case can be used to evaluate the fractional operators. The situation is more delicate when the boundary operator is non-local both in space and time. In this case the sparse matrix of the linear system typically gets additional entries due to the TBC.

Using (like in Section 3.3.1) a rational approximation of the square root,

$$\sqrt{z} \approx a_0 + \sum_{j=1}^m \frac{a_j z}{z+b_j}, \tag{4.13}$$

with $z = is - \xi^2$ and complex valued coefficients a_j and b_j yields again fully local boundary conditions — as an approximation of $\widetilde{\Lambda^+}$. The crucial point here is that this approximation can be reformulated in the space and time domain as a coupled system of differential

equations using Lindmann's trick [89]. Indeed, we can compute the normal derivative trace of u by

$$\partial_{\mathbf{n}} u = a_0 u + \sum_{j=1}^{m} a_j (i\partial_t + \Delta_\Gamma) \varphi_j,$$

with the auxiliary functions φ_j satisfying the surface Schrödinger equations

$$(i\partial_t + \Delta_\Gamma + b_j)\varphi_j = u, \quad \text{on } \mathcal{R} \times \mathcal{R}^+.$$

Since only partial differential operators are involved, this formulation is purely local. Di Menza [40–42] was the first to investigate this approach for the Schrödinger equation. In [125,126], Szeftel develops a deep analysis about the way of deriving suitable approximations using an optimization technique of the reflection coefficient in suitable, weighted spaces in the hyperbolic region. Problems related to well-posedness of the truncated initial boundary value problems are also stated in [125, 126]. Let us mention that much more developments have been done in the case of wave equations (see, e.g., the review papers by Hagstrom [67, 68] and also [14, 80, 97], where rational approximants valid in both the hyperbolic and elliptic zones are available). It could be useful to apply these recent developments also to Schrödinger-type equations.

In all of the situations discussed above, the authors consider the TBC just for the half space. In many practical simulations, however, such TBCs are imposed on a rectangular artificial boundary. Since this generates some reflections at the corners, suitable additional *corner conditions* should be added to avoid these reflections (cf. Collino [35] for corner conditions for wave-like equations). For the Schrödinger equation, however, no results exist on this topic so far.

4.2.2   The waveguide geometry

The 2D Schrödinger equation on the infinite strip $\mathcal{R} \times (0, Y)$ with homogeneous Dirichlet BCs at $y = 0$ and $y = Y$ has important applications for modeling the leads in quantum waveguides. The exact TBC at an artificial boundary (perpendicular to the channel) was derived in [22] under the assumption that the exterior potential V only depends on the transversal coordinate. Decomposing the wave function u into the (transversal) eigenfunctions of

$$[-\partial_y^2 + V(y)]\chi^m(y) = E^m \chi^m(y)$$

yields — for each mode u^m — the 1D TBC (2.1) pertaining to the potential E^m. Hence all the methods described for the 1D Schrödinger equation can be employed. Expanding the boundary data into eigenfunctions however makes the method non-local in space.

The PML method and the method based on the pole condition do not require a decomposition of the boundary data into eigenmodes of the Laplace-Beltrami operator. For the PML method a complex continuation in $\mathcal{R}$ can be used. For the pole condition a Lapalace transform in $\mathcal{R}$ can be used as long as the Laplace-Beltrami operator $[-\partial_y^2 + V(y)]$ is positive [106].

4.2.3 Circular artificial boundary

Since the problem of reflections at the corners is still unsolved for the Schrödinger equation, alternative strategies have been pursued. An obvious choice is to use circular artificial boundaries. As in the preceding subsection, the derivation of the TBC is based on the Laplace transform in time and Fourier series in space.

We assume that the *computational domain* is the disk

$$\Omega = D(0,R) \subset \mathcal{R}^2,$$

centered at the origin with radius R. The transient Schrödinger equation then reads in polar coordinates (r,θ):

$$iu_t + \frac{1}{r}(ru_r)_r + \frac{1}{r^2}u_{\theta\theta} - V(r,\theta,t)u = 0, \quad (r,\theta,t) \in \Omega \times \mathcal{R}^+, \tag{4.14a}$$

$$u(r,\theta,0) = u^I(r,\theta), \qquad \forall (r,\theta) \in \Omega, \tag{4.14b}$$

$$u(r,0,t) = u(r,2\pi,t), \qquad r > 0, t > 0, \tag{4.14c}$$

$$\lim_{r \to \infty} u(r,\theta,t) = 0, \qquad 0 < \theta < 2\pi, t > 0. \tag{4.14d}$$

If V is constant outside the computational domain Ω, the solution to the associated exterior Helmholtz-type system (in the Laplace domain) can be obtained by a series expansion in Hankel functions of the first kind. This yields the exact boundary condition as the *Dirichlet-to-Neumann map*

$$
\begin{aligned}
&\partial_\mathbf{n} u(R,\theta,t) \\
&= \frac{1}{2\pi} \sum_{m \in \mathbb{Z}} \mathcal{L}^{-1} \left(\sqrt{i \cdot - V} \frac{H_m^{(1)'}(\sqrt{i \cdot - V}R)}{H_m^{(1)}(\sqrt{i \cdot - V}R)} \int_0^{2\pi} \hat{u}(R,\phi,\cdot) e^{-im\phi} d\phi \right)(t) e^{im\theta}
\end{aligned}
\tag{4.15}
$$

on $\partial\Omega$ (cf. [10] for details, or [13] for an alternative derivation based on diagonalizing the integral operators in (4.4) on the discrete Fourier basis). As in the half space case, this boundary condition (4.15) is non-local in time and space. While this exact TBC has not been used intensively for Schrödinger-type equations, the development of fast and stable numerical schemes for (4.15) would be highly desirable.

In [72], the authors give a reformulation of this TBC which appears more practical for numerical implementations: There, the *s*-integral of the inverse Laplace transform in (4.15) is replaced by a convolution in time, with a convolution kernel again involving Bessel functions. Moreover, truncating the infinite sum over the Fourier modes yields satisfactory numerical results. Note that the extension to three dimensional space is given in [74].

4.2.4 General convex artificial boundary

As previously seen, transparent and artificial boundary conditions can be constructed easily for some simple geometries like the half space (vanishing curvature) or the disk

(constant curvature). Compared to the one-dimensional case, the additional ingredient was the Fourier transform in space. In the case of a general smooth boundary Γ, the derivation of the TBC is based on the local construction of the non-reflecting operator in a generalized coordinates system. This extension of the work of Engquist and Majda [57,58] was developed in [8,12]. Roughly speaking, the curved domain is mapped into the half-space. This implies that the resulting modified Schrödinger equation has variable coefficients making the classical Fourier analysis inapplicable. Indeed, the Fourier transform of this operator involves some convolutions difficult to manipulate from a computational viewpoint. Using pseudodifferential operators and the symbolic M-calculus (see [84] and Section 4.2.1) an asymptotic expansion of the total symbol of the non-reflecting operator outside the M-quasi glancing zone was computed in [8]. With an additional high-frequency expansion (w.r.t. the small parameter $|\xi|^2/|s|$) in the hyperbolic zone, the authors obtain the following local in space and non-local in time artificial boundary conditions:

Proposition 4.1. The Schrödinger equation with an artificial boundary condition of order $\frac{\ell}{2}$, with $\ell \in \{1, \cdots, 4\}$, is defined by the initial boundary value problem

$$\begin{cases} (i\partial_t + \Delta)u = 0, & (\mathbf{x}, t) \in \Omega \times \mathcal{R}^+, \\ \partial_\mathbf{n} u + T_{\frac{\ell}{2}} u = 0, & (\mathbf{x}, t) \in \Gamma \times \mathcal{R}^+, \\ u(\mathbf{x}, 0) = u^I(\mathbf{x}), & \mathbf{x} \in \Omega. \end{cases} \tag{4.16}$$

The operators $T_{\frac{\ell}{2}}, \ell \in \{1, \cdots, 4\}$ are pseudodifferential in time and differential in space, and they are given by

$$\begin{aligned} T_{\frac{1}{2}} u &= e^{-i\pi/4} \partial_t^{\frac{1}{2}} u, \quad T_1 u = T_{\frac{1}{2}} u + \frac{\kappa}{2} u, \quad \text{on } \Gamma \times \mathcal{R}^+, \\ T_{\frac{3}{2}} u &= T_1 u - e^{i\pi/4} \left(\frac{\kappa^2}{8} + \frac{1}{2} \Delta_\Gamma \right) I_t^{\frac{1}{2}} u, \quad \text{on } \Gamma \times \mathcal{R}^+, \\ T_2 u &= T_{\frac{3}{2}} u + i \left(\frac{\kappa^3}{8} + \frac{1}{2} \partial_\zeta (\kappa \partial_\zeta) + \frac{\Delta_\Gamma \kappa}{8} \right) I_t u, \quad \text{on } \Gamma \times \mathcal{R}^+. \end{aligned} \tag{4.17}$$

Here, the half-order fractional derivative and integral operators are given by the relations (4.12), and the Laplace-Beltrami operator is defined by $\Delta_\Gamma = \partial_\zeta^2$. $\kappa = \kappa(\zeta) \geq 0$ is the curvature of Γ and ζ its arc length parameter.

The numerical implementation of these conditions can be realized directly using for example a Crank-Nicolson scheme and the associated discretizations (2.24), (2.25), and (2.27) of the fractional derivatives and integral operators. Faster schemes like the ones proposed in the one-dimensional case could also be used, but this has not yet been addressed in the literature. Finally, the spatial discretization can be realized by finite elements (cf. [12] for details).

Besides of the construction of artificial BCs for variable coefficients Schrödinger equations, this pseudodifferential operator calculus approach also applies to the one-dimensional Schrödinger equation with a space and time dependent potential (cf. (2.14) and [11]).

In [125,126], Szeftel proposed some extensions of this approach to higher dimensions following the techniques introduced by Halpern and Rauch for the heat equation [71]. Moreover, rational approximations of the square root like in (4.13) are analyzed, leading to fully local artificial boundary conditions.

4.3 Fully discrete transparent boundary condition

4.3.1 The waveguide geometry

For the setting described in Section 4.2.2 the authors in [18] consider the analogous situation for a regular Crank-Nicolson, 5-point finite difference scheme in the exterior domain. For a constant exterior potential $V_{l,r}$, the wavefunction is now decomposed into the discrete Fourier modes $\chi_k^m = \sin(\pi km/K)$; $k,m = 1,\cdots,K-1$ with $K\Delta y = Y$. These modes u^m are again decoupled in the exterior domain, and each of them satisfies the 1D discrete transparent boundary condition (DTBC) (2.47) pertaining to the potential

$$V^m = V_{l,r} + \frac{1-\cos(\pi m/K)}{\Delta y^2}; \quad m = 1,\cdots,K-1.$$

An extension of such 2D DTBCs for a 9-point finite difference scheme (Numerov scheme) and quantum waveguide simulations are the topic of [117].

4.3.2 Circular geometry

In [19], the authors derive DTBCs for the fully discrete time-dependent Schrödinger equation, with a circle of radius R as computational domain (cf. Section 4.2.3). They consider a Crank-Nicolson finite difference scheme for the Schrödinger equation in polar coordinates (4.14), with the *radial offset grid points* $r_j = (j+\frac{1}{2})\Delta r$, the uniform angular grid points $\theta_k = k\Delta\theta$ ($K\Delta\theta = 2\pi$), and $t_n = n\Delta t$. Note that an offset grid is chosen to circumvent the singularity problem at the origin.

In order to reduce the problem to the simpler 1D case, a discrete Fourier transform in θ-direction yields the following scheme in the exterior domain $j \geq J-1$:

$$-\frac{i}{\Delta t}(u_j^{m,n+1} - u_j^{m,n})$$
$$= \frac{1}{r_j}\frac{1}{\Delta r_j}\left[\frac{r_{j+1/2}(u_{j+1}^{m,n+\frac{1}{2}} - u_j^{m,n+\frac{1}{2}})}{\Delta r_{j+1/2}} - \frac{r_{j-1/2}(u_j^{m,n+\frac{1}{2}} - u_{j-1}^{m,n+\frac{1}{2}})}{\Delta r_{j-1/2}}\right] - V_j^m u_j^{m,n+\frac{1}{2}},$$
$$V_j^m := V_R + \frac{1-\cos(2\pi m/K)}{r_j^2\Delta\theta^2}, \qquad 0 \leq m \leq K-1, \ n \geq 0.$$

As in Section 4.3.1 the modes u^m, $m=0,\cdots,K-1$ are independent of each other in the exterior domain $r \geq R$ since the potential V is constant there. Therefore, we continue the presentation for a separate mode (omitting the superscript m in the notation). For each fixed j we use the $\mathcal{Z}$-transform of the sequence $\{u_j^n\}$, $n \in \mathbb{N}_0$ and obtain the transformed exterior scheme:

$$-i\rho_j \delta(z)\hat{u}_j(z) = \frac{1}{r_j}\left[r_{j+1/2}\big(\hat{u}_{j+1}(z)-\hat{u}_j(z)\big)-r_{j-1/2}\frac{\Delta r_{j+1/2}}{\Delta r_{j-1/2}}\big(\hat{u}_j(z)-\hat{u}_{j-1}(z)\big)\right]$$
$$-\Delta r_j \Delta r_{j+1/2}V_j \hat{u}_j(z), \quad j \geq J-1, \tag{4.18}$$

with the mesh ratio $\rho_j = \Delta r_j \Delta r_{j+1/2}/\Delta t$ and $\delta(z)=2(z-1)/(z+1)$ denotes the generating function of the Crank-Nicolson method (cf. Example 2.1). This is a homogeneous second order difference equation

$$a_j \hat{u}_{j+1}(z)+b_j(z)\hat{u}_j(z)+c_j \hat{u}_{j-1}(z)=0, \quad j \geq J-1, \tag{4.19}$$

with the non-constant coefficients

$$a_j = \frac{r_{j+1/2}}{r_j}, \tag{4.20a}$$

$$b_j(z) = -\frac{1}{r_j}\left[r_{j+1/2}+r_{j-1/2}\frac{\Delta r_{j+1/2}}{\Delta r_{j-1/2}}\right]+i\rho_j \delta(z)-\Delta r_j \Delta r_{j+1/2}V_j, \tag{4.20b}$$

$$c_j = \frac{r_{j-1/2}}{r_j}\frac{\Delta r_{j+1/2}}{\Delta r_{j-1/2}}. \tag{4.20c}$$

For a regular radial grid and in the $j \to \infty$—limit this reduces to the 1D case of (2.42). Hence, the 1D DTBC (2.47) represents the limiting BC for large circles.

Just like in (2.43), the quotient

$$\hat{\omega}_j(z) = \frac{\hat{u}_j(z)}{\hat{u}_{j-1}(z)}$$

characterizes the $\mathcal{Z}$-transformed DTBC at $j=J$, if the decaying solution (as $j \to \infty$) of (4.19) is chosen. In contrast to the 1D case, $\hat{\omega}_j(z)$ is not known explicitly, but can be computed recursively from (4.19). For stability reasons

$$\hat{\omega}_\infty(z) := \lim_{j \to \infty} \hat{\omega}_j(z)$$

(known from (2.44)) serves as starting value at some sufficiently large index J_∞.

5   Nonlinear Schrödinger equations

Nonlinear Schrödinger equations [31, 123], both with local and nonlocal non-linearities are very important in many applications: optics, electromagnetism, plasma physics, etc.

Concerning the extension of TBCs, most work has been done on local non-linearities of the form

$$i\partial_t u + \partial_x^2 u + V(u)u = 0, \quad x \in \mathcal{R}, t > 0. \tag{5.1}$$

In this section we shall confine ourselves to the cubic nonlinear Schrödinger equation with $V(u) = q|u|^2$, $q \in \mathcal{R}$ which is the best studied example.

Different semi-discrete schemes can be used but the Crank-Nicolson [39]

$$i\frac{u^{n+1} - u^n}{\Delta t} + \partial_x^2 \frac{u^{n+1} + u^n}{2} + \frac{V(u^{n+1}) + V(u^n)}{2}\frac{u^{n+1} + u^n}{2} = 0, \tag{5.2}$$

and the Durán-Sanz-Serna [46]

$$i\frac{u^{n+1} - u^n}{\Delta t} + \partial_x^2 \frac{u^{n+1} + u^n}{2} + V\left(\frac{u^{n+1} + u^n}{2}\right)\frac{u^{n+1} + u^n}{2} = 0 \tag{5.3}$$

schemes are very popular.

5.1 Exact continuous TBC

In the recent paper [26], Boutet de Monvel *et al.* constructed the nonlinear Dirichlet-to-Neumann map associated with the one-dimensional, cubic nonlinear Schrödinger equation (NLS). Their approach is based on the inverse scattering theory which, of course, restricts this procedure to fully integrable systems (i.e., a cubic nonlinearity in the Schrödinger equation).

In [132], Zheng reformulates this TBC to make it more suitable for numerical approximations. This nonlinear TBC is defined through a set of nonlinear integro-differential equations. With $g_0(t) := u(x_r, t)$ and $g_1(t) := \partial_\mathbf{n} u(x_r, t)$ it reads

$$g_1(t) = g_0(t)M_2(t, t) - e^{-i\pi/4}\partial_\tau^{1/2} M_1(t, 2\tau - t)_{|\tau = t}. \tag{5.4}$$

The auxiliary functions $L_{1,2}(t, s)$, $M_{1,2}(t, s)$ satisfy the following hyperbolic system (linear for given g_0, g_1) on the cone $t \geq 0$, $|s| \leq t$:

$$
\begin{aligned}
&L_{1,t} - L_{1,s} = ig_1(t)L_2 + \alpha(t)M_1 + \beta(t)M_2, \\
&L_{2,t} + L_{2,s} = \frac{iq}{2}\bar{g}_1(t)L_1 - \alpha(t)M_2 - \frac{q}{2}\bar{\beta}(t)M_1, \\
&M_{1,t} - M_{1,s} = 2g_0(t)L_2 + ig_1(t)M_2, \\
&M_{2,t} + M_{2,s} = -q\bar{g}_0(t)L_1 + \frac{iq}{2}\bar{g}_1(t)M_1, \\
&\alpha(t) := \frac{q}{4}(\bar{g}_0 g_1 - \bar{g}_1 g_0), \qquad \beta(t) := \frac{i}{2}\left(\dot{g}_0 - \frac{iq}{2}|g_0|^2 g_0\right),
\end{aligned}
\tag{5.5}
$$

with the boundary conditions at $s = \pm t$:

$$
\begin{aligned}
&L_1(t, t) = \frac{i}{2}g_1(t), \qquad M_1(t, t) = g_0(t), \\
&L_2(t, -t) = M_2(t, -t) = 0.
\end{aligned}
$$

In [132], Zheng compares three schemes for the interior discretization of the NLS: the schemes (5.2) and (5.3), and the relaxation scheme of Besse in [24]. For the TBC a predictor-corrector scheme is employed. Moreover, the fractional derivative operator is discretized by the Baskakov-Popov scheme given in (3.7) and by scheme (2.24)-(2.25) — the latter being faster and more accurate. Finally, the resulting discretized nonlinear system is solved by a successive approximation method.

The numerical simulations (using a spatial finite element discretization) of propagating solitons show that this nonlinear and nonlocal TBC avoids any reflections at the boundary. However, there is no stability analysis of this scheme available yet.

5.2   Approximate continuous TBCs – the pseudodifferential operator approach

Concerning approximate continuous nonlinear TBCs we shall first discuss approaches based on the pseudodifferential operator calculus and then (in Section 5.3) a paradifferential operator approach. While the justification of the pseudodifferential approach requires C^∞-smoothness of u, the paradifferential approach also works for solutions with finite smoothness.

While the exact nonlinear TBC can be constructed for the cubic nonlinear Schrödinger equation, other nonlinearities require approximations in the TBC. Since the pseudodifferential operator calculus is *a priori* only developed for *linear*, variable coefficients equations, it will be applied to some linearized problems: Interpreting $V(u)$ in (5.1) as a potential, i.e., a varying coefficient for u (and ignoring for the moment its dependence on u) indeed yields good results for the nonlinear case.

In [11], the authors use a gauge change to handle the nonlinearity $V(u)u$. While [11] actually only deals with the cubic NLS, the very same approach applies to general nonlinearities, and this is a big advantage over the strategy from Section 5.1. The starting point is Remark 2.5 on time-dependent potentials V: For the linear equation the exact TBC can be obtained by a simple gauge change. Using this remark, the same strategy is considered for a time-spatial varying potential V. Then, using approximate factorization techniques and a fractional pseudodifferential operator calculus, a hierarchy of increasing order artificial boundary conditions is derived. Then, the potential is formally replaced by the nonlinearity $V(u)u$. For example, the second order nonlinear artificial boundary condition reads

$$\partial_{\mathbf{n}}u + e^{-i\pi/4}e^{i\mathbb{U}}\partial_t^{1/2}(e^{-i\mathbb{U}}u) + \frac{i}{4}\partial_{\mathbf{n}}(V(u))e^{i\mathbb{U}}I_t(e^{-i\mathbb{U}}u) = 0, \quad \text{at } \Gamma, \tag{5.6}$$

where I_t denotes the integration operator and $\mathbb{U}$ is given by

$$\mathbb{U}(x,t) = \int_0^t V(u(x,s))ds. \tag{5.7}$$

At the semi-discrete level, the two time discretization schemes (5.2) and (5.3) are considered. The fractional operators are discretized following (2.24)-(2.25). Stability results

are stated at the semi-discrete level for the simplest first-order condition but the problem remains open for the above second-order condition. Finally, a fixed point algorithm is applied to handle the nonlinearity. The spatial discretization is based on a finite element method.

Numerical simulations (soliton propagation and interaction of two solitons) show the efficiency of the approach, i.e., small numerical reflections. However, compared to the method of Zheng, these conditions only work well for sufficiently fast solitons. The main reason is that the underlying asymptotic expansion used to derive these conditions is valid at high frequencies.

A similar approach has been recently derived by Szeftel in [125,127,128] for a general nonlinear one-dimensional Schrödinger equation. He applies a pseudodifferential factorization directly to the linearized equation with the potential term Vu (i.e., without the gauge change in (5.6), (5.7)). This yields a hierarchy of artificial boundary conditions, and finally the nonlinearity $V(u)$ is plugged into the results. In the cubic case, for example, the second order BC reads

$$\partial_{\mathbf{n}}u + e^{-i\pi/4}\partial_t^{1/2}u - qe^{i\pi/4}\frac{|u|^2}{2}I_t^{1/2}u + q\frac{i}{4}\partial_{\mathbf{n}}(|u|^2)I_tu = 0, \quad \text{at } \Gamma. \tag{5.8}$$

At the semi-discrete level, the interior scheme is based on the Durán-Sanz-Serna scheme and a fixed point algorithm. The fractional operators are discretized again using (2.24)-(2.25). The numerical results are satisfactory, but the approach in [11] yields a better accuracy for the cubic NLS.

5.3 Approximate continuous TBCs – the paradifferential operator approach

A disadvantage of the pseudodifferential operator approach is the fact that the linearization of (5.1) bears a certain arbitrariness. This can be removed using the paralinearization of Bony [25]. His paradifferential calculus has been applied formally the first time in the context of artificial boundary conditions to the nonlinear viscous Burgers equation by Dubach [44]. He showed that, in some situations, an improved accuracy can be expected compared to a purely pseudodifferential approach. Szeftel recently introduced in a series of papers [125, 127, 128] a rigorous application of the paradifferential calculus to several nonlinear wave and Schrödinger equations. In almost all numerical examples of [128] the first order local, nonlinear ABC obtained with the paradifferential strategy yields better results than the ABC based on the pseudodifferential approach. However, the paradifferential strategy does not apply to the cubic NLS, since that nonlinearity involves both u and $\bar{u}$. Reference [127] extends the numerical comparison of the above two strategies to first and second order nonlocal, nonlinear ABC for the 1D Schrödinger equation with the nonlinearity $-u\partial_x u$. Again, the paradifferential ABCs yield better results — at second order, however, only for short time.

Even if the paradifferential method is very technical, it seems to provide a valuable future direction for simulating nonlinear equations including Schrödinger-type equations.

Finally, let us remark that there exists a recent completely different approach, the *Time Dependent Phase Filter* by Soffer and Stucchio [119]. In this method the NLS is solved on a sufficiently large domain (assuming that the nonlinearity is localized in this region) supplied with periodic boundary conditions that allow for a fast solution of the interior problem by spectral methods based on FFT.

6   Numerical examples

In this final section we shall use some benchmark problems for the linear Schrödinger equation in 1D to compare the numerical results from using the different approaches presented in the preceding Sections 2 and 3.

The wide diversity of the methods presented in this review paper leads us to select only some of them, trying to be as much thorough as possible by using the historical approaches (Baskakov-Popov, Shibata, Kuska,···) to the more recent ones (pole conditions,···). Let us denote by CNFE and CNFD the Crank-Nicolson finite elements methods and Crank-Nicolson finite differences methods, respectively. Each method is grouped into different families. The *Fevens-Jiang family* includes methods which use (3.14) as the origin of approximation. Next, the *square root approximation family* defines the methods which use (3.11). In the same spirit, the *Finite Differences family* and the *Finite Elements family* brought together methods which use finite differences or finite elements schemes in the computational domain. This separation into four basic groups allows on the one hand to identify in each family the advantages and the drawbacks of the methods, and on the other hand to understand if a family is more or less competitive compared to another one. The proposed designation is shown in Table 2. The optimized coefficients for the Szeftel method are given by

$$a_0^3 = 0.7269284, \quad a_1^3 = 2.142767, \quad a_2^3 = 5.742223, \quad a_3^3 = 46.58032,$$
$$d_1^3 = 6.906263, \quad d_2^3 = 65.82243, \quad d_3^3 = 1124.376.$$

For PML methods using finite elements the layer discretization and the layer thickness is chosen by the pseudocode given in Table 1 on Page 755. The parameters are $\text{eps} = 10^{-7}$, $\lambda_{\min} = 0.05$ and $\lambda_{\max} = 20$. For $\Delta x = 0.01$, i.e., $J = 1500$ grid points in the interior, this results in a layer with 94 grid points and a thickness of about 52.7.

Before discussing the numerical simulations, let us summarize the different types of errors expected for each method. Since a semi-discrete Crank-Nicolson scheme based on the trapezoidal rule is used, the error in time is $\mathcal{O}(\Delta t^2)$. The space discretization is done using the second order finite difference scheme (2.29) ($p = 1$) or using a finite element approximation with polynomials of order $p = 1, 2$. Let us remark that during the assembling process for $p = 2$, a simple elimination procedure could be performed on the elementary local matrices to only work with the extreme nodes of the finite elements. Therefore, the size of the linear system to solve would be the same for the linear and quadratic finite elements. The spatial L^2-error is $\mathcal{O}(\Delta x^{p+1})$. The global error resulting from the interior

Table 2: Implemented numerical methods.

Name	Methods
Fevens–Jiang family	
Shibata [118]	CNFD using (3.14) with $m = 2$
Kuska [82]	CNFD using (3.14) with $m = 3$
Fevens [59]	CNFD using (3.14) with $m = 4$
Approximation of the square root	
Di Menza [27]	CNFD using (3.11) with 27 coefficients
Padé [127]	CNFD using (3.12) with 20 coefficients
Szeftel [127]	CNFD using (3.11) with 4 optimized coefficients
Finite differences family	
Arnold–Ehrhardt [16]	CNFD using (2.47)–(2.48)
FD [9, 112, 113]	CNFD using (2.24) with convolution weights (2.25)
Baskakov–Popov [21]	CNFD using (3.7)
PML FD	CNFD using (3.28)
Pole FD [106]	CNFD using (2.16) with 20 coefficients
Finite elements family	
FEM 1, FEM 2 [9]	CNFE using (2.24) with convolutions weights (2.25) and finite elements of polynomial degree 1 and 2
PML FEM 1, PML FEM 2	CNFE using (3.28)
Pole FEM 1, Pole FEM 2 [106]	CNFE using (2.16) with 20 coefficients

discretization sums up to the order $\mathcal{O}(\Delta t^2) + \mathcal{O}(\Delta x^{p+1})$. The discretization error stemming from approximating the boundary condition (2.1) or (2.10) is considered separately for each method below. From a general point of view, this error can be written through a term C^{BC} which is equal to zero if a transparent Boundary Condition is considered and is strictly positive for an approximate boundary condition. Of course, C^{BC} depends on the considered boundary condition and from its tuning parameters like e.g. the order of the paraxial approximation or the size of the PML layer. Then, the global error of a scheme for a boundary condition is:

$$E(p, C^{BC}) = \mathcal{O}(\Delta t^2) + \mathcal{O}(\Delta x^{p+1}) + C^{BC}.$$

Being given a Boundary Condition, the value of C^{BC} can be observed in the next numerical tests by considering the limit of E as Δx and Δt tend both toward zero. More systematically, let us consider each boundary condition separately:

- For the Fevens-Jiang and approximation of the square-root families, second-order schemes in space and time are used. Moreover, we have an approximation error C^{BC} independent of the step sizes Δt and Δx. It is related to the way the approximation of the exact fractional derivative operator is made according to parameters values given in Table 2. This results in a general error $E(1, C^{BC})$.

- The fully discrete scheme of Arnold and Ehrhardt [16] described in Section 2.5 yields an error $E(1, 0)$ since it is an exact discrete condition.

- The **FEM p** method using (2.24) with finite elements for the space discretization does not produce any additional error term. The total error is then $E(p,0)$ since it is an exact boundary condition.

- The **FD** approach using finite differences with (2.24) for the space discretization have additional error terms. The normal derivative is approximated by (3.3) and the discrete interior solution is coupled to the continuous solution in the exterior domain. This will give rise to an additional error term of order $\mathcal{O}(\Delta x^2)$ [9,112,131] which leads globally to an error $E(1,0)$.

- In [124], Sun and Wu prove that the error of the Baskakov-Popov time discretization scheme [21] is $\mathcal{O}(\Delta x^{3/2} + \Delta t^{3/2} \Delta x^{-1/2})$ for the discretization (3.1). The second-order convergence is lost for stability reasons. In the present paper and in [21], the discretization (3.2) is used. It appears that the numerical error is: $ErrTf = \mathcal{O}(\Delta t^{3/2})$ and $ErrL_2 = \mathcal{O}(\Delta t^{3/2})$ for $\Delta t \to 0$ and $ErrTf = \mathcal{O}(\Delta x^2)$, $ErrL_2 = \mathcal{O}(\Delta x^2)$ for $\Delta x \to 0$ (see (6.3) for the errors definitions). Since it is an approximation of the transparent operator, we furthermore have $C^{BC} = 0$.

- The **PML** methods (3.28) using either finite differences (**PML FD**) or finite elements (**PML FEM**) show an error $\mathcal{O}(\exp(-c\rho))$ for some $c > 0$, independent of Δt and Δx setting the PML at a distance ρ. The total error is $E(1,C^{BC})$, with $C^{BC} = C^{BC}(\rho)$ which can be made small by increasing ρ.

- The **Pole** condition methods (2.16) using either finite differences (**Pole FD**) or finite elements (**Pole FEM**) [106] again show a truncation error independent of Δt and Δx introduced by truncating the power series (3.30). We use 20 coefficients in the experiments. Additionally the (**Pole FD**) methods suffer from an $\mathcal{O}(\Delta x^2)$ error term introduced by (3.3). The total error is $E(1,C^{BC})$, where C^{BC} can be made small by increasing the number of coefficients in the power series expansion.

6.1 Numerical Example 1: Free Schrödinger equation

As a first benchmark problem we consider the Schrödinger equation (1.1) with a vanishing potential $V \equiv 0$ and a *Gaussian initial condition*

$$u^I(x) = \sqrt[4]{\frac{2}{\pi}} \exp\left(-(x-x_c)^2 + ik_0(x-x_c)\right), \quad x \in \mathcal{R}. \tag{6.1}$$

For this simple example the *continuous solution* u_{ex} can be calculated explicitly:

$$u_{\text{ex}}(x,t) = \sqrt[4]{\frac{2}{\pi}} \sqrt{\frac{i}{-4t+i}} \exp\left(\frac{-i(x-x_c)^2 - k_0(x-x_c) + k_0^2 t}{-4t+i}\right), \tag{6.2}$$

$x \in \mathcal{R}$, $t > 0$. The computational domain is $\Omega_{int} =]-12,3[$, the Gaussian is centered around $x_c = -6$, the wave number is chosen to be $k_0 = 5$, and the final time of the simulation is
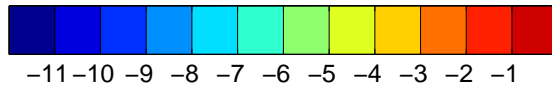
Figure 4: Colormap for log-contour plot.
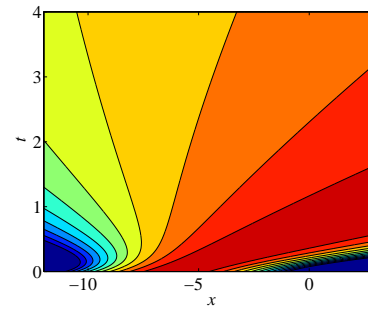
Figure 5: Example 1: Arnold-Ehrhardt.

fixed to $T_f = 4$. The initial Gaussian is cut-off close to the artificial boundary $x_l = -12$, $x_r = 3$. Since $|u^I(x_{l,r})| \approx 10^{-11}$ this has virtually no influence on the results.

Note that the high frequency of the solution needs a very good approximation of the fractional operator $\partial_t^{1/2}$ which allows to distinguish qualities and defaults of the different tested numerical methods described in Table 2.

6.1.1 Contour plots of the solutions

In this section we use $J = 1500$ grid points (i.e., $\Delta x = 10^{-2}$) for the spatial discretization and a time step $\Delta t = 10^{-3}$. To bring to the fore the unphysical numerical reflections linked to the different methods, we plot the contour of $\log_{10}(|u|)$. Indeed, the numerical reflections are too small to be visualized in a traditional contour plot. Using a *log-contour plot*, as some kind of 'zooming tool' allows to show small level of reflections. We use a common colormap for all contour plots figures (see Fig. 4).

The following figures show some unphysical reflections that are very small in magnitude compared to the discretization error (cf. Section 6.1.3) for the chosen parameters. Despite this fact, they yield some suitable guidance of what might be considered as a good artificial boundary condition. In Fig. 5 the contour plot of the solution for the fully discrete scheme of Arnold and Ehrhardt is presented. By construction there are no reflections at all from the discrete TBC, thus it serves as a *reference solution* for the other methods.

In the sequel we present the contour plots according to the group structure shown in Table 2. At the sight of the contour plots of the Fevens-Jiang family in Fig. 6, it is obvious that increasing the level m in (3.14) improves significantly the quality of the solution. Nevertheless, these methods, older than the other ones developed in this article, are less competitive.

The solutions built with a square root approximation shown in Fig. 7 are far better and also show a grading in the quality of the results. Note that the Bruneau-Di Menza method needs 27 coefficients to reach this level of reflection and for the Padé method (3.12) 20 coefficients are sufficient to obtain a good approximate solution. Let us also point out that the construction of the coefficients by minimization of the reflection coefficient (3.13) allows to highly reduce the numerical artefacts. Indeed, the Szeftel method only uses 3

(a) Shibata   (b) Kuska   (c) Fevens
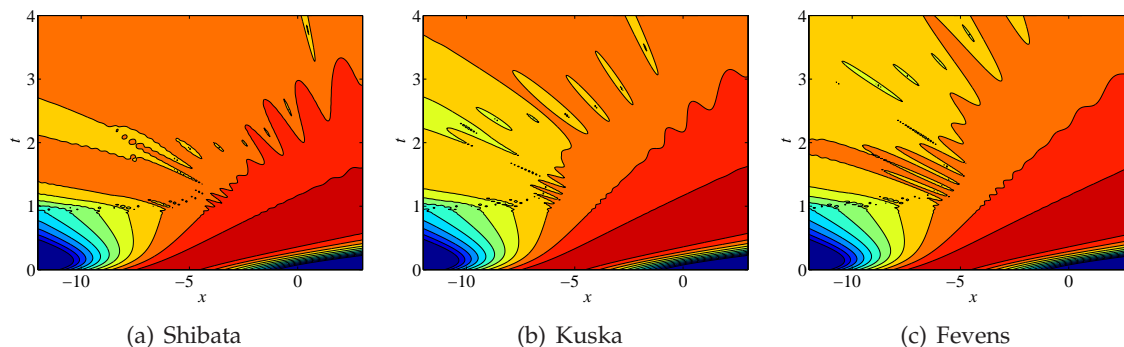
Figure 6: Example 1: Fevens-Jiang family.

(a) Di Menza   (b) Padé   (c) Szeftel
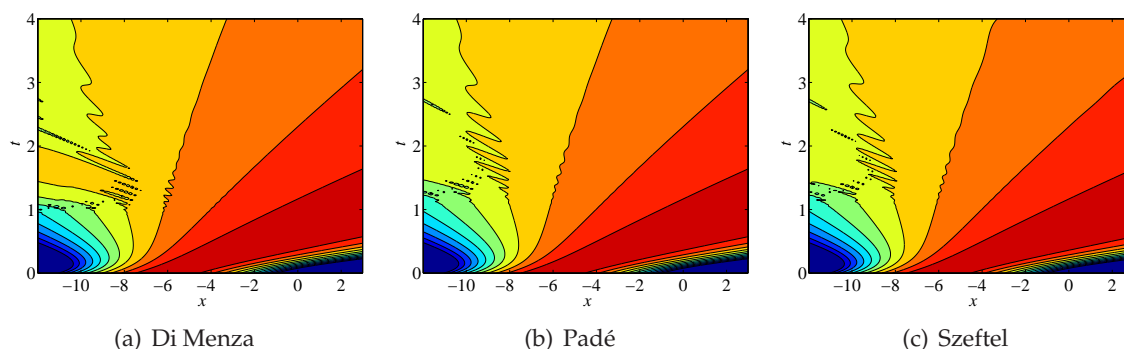
Figure 7: Example 1: Approximation of the square root.

coefficients following this rule. We remark that the accuracy within this group strongly depends on the chosen discretization parameters, e.g., there also exists parameters where the Szeftel approach with only 3 coefficients performs best (within this group).

Fig. 8 shows the results for the finite differences family and the worst result is the one arising from the Baskakov-Popov method. These (additional) artificial reflections in Fig. 8(b) must be attributed to the discretization of the convolution integral only, as the approximation used for the normal derivative for the Baskakov-Popov method and the FD method (Fig. 8(a)) are the same. The best results in this group, namely the two curves resulting from the FD and the Pole FD method (Fig. 8(d)), are indistinguishable. The PML FD using the most simple PML, with a fixed thickness ρ and a uniform discretization in the layer, yields a middle-rate outcome within this finite differences family.

Finally, Fig. 9 presents the contour plots when using finite elements in the computational domain. The methods using second order finite elements (Figs. 9(b), 9(d) and 9(f)) show no reflections. The FEM 1 (Fig. 9(a)) and Pole FEM 1 (Fig. 9(e)) methods shows an equal high accuracy. Compared to the other first order finite element methods the PML FEM 1 method (Fig. 9(c)) shows some slightly stronger reflections. The PML methods based on finite elements employ Algorithm 1 for the choice of the PML discretization.

(a) FD   (b) Baskakov-Popov

(c) PML FD   (d) Pole FD
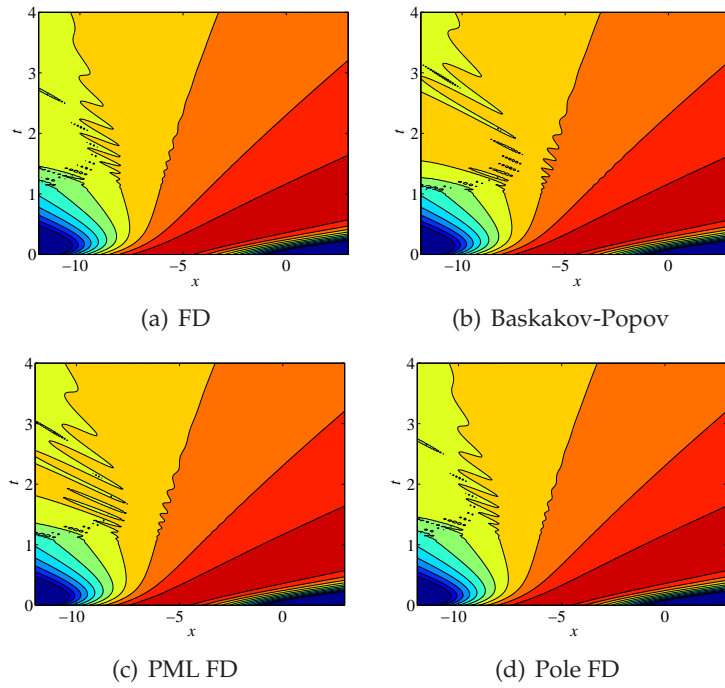
Figure 8: Example 1: Finite differences family

(a) FEM 1   (b) FEM 2   (c) PML FEM 1

(d) PML FEM 2   (e) Pole FEM 1   (f) Pole FEM 2
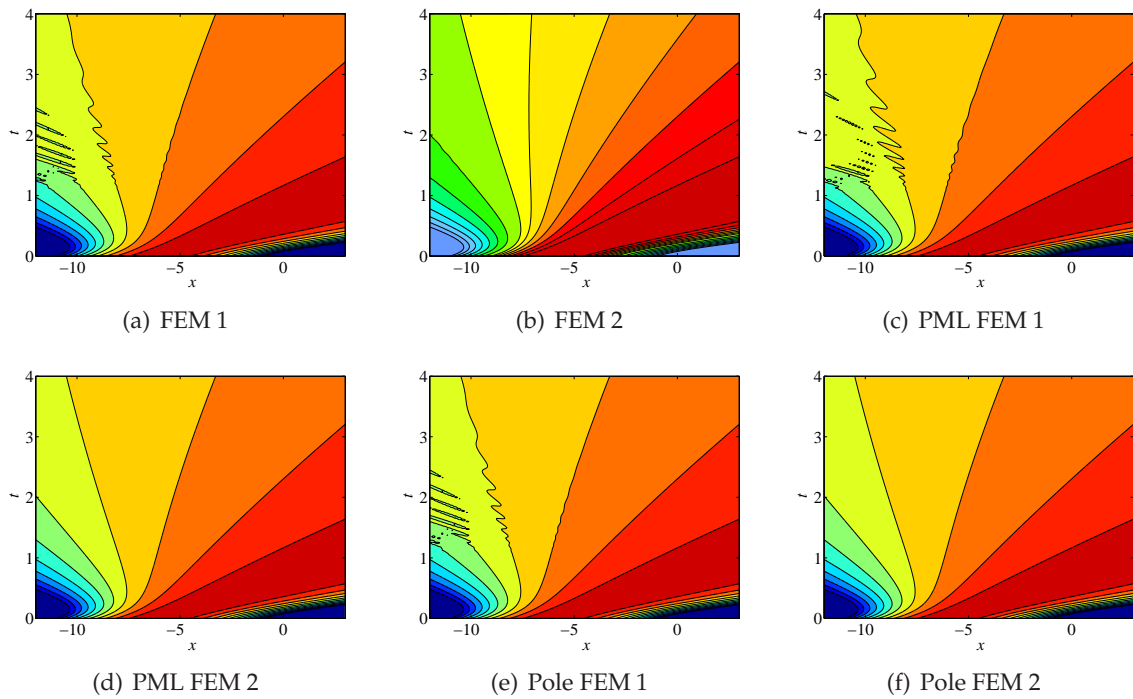
Figure 9: Example 1: Finite elements family.

The methods based on finite differences or finite elements are similar with a light advantage for the finite elements ones (see the comparison between FEM 1 — FD and Pole FEM 1 — Pole FD (Figs. 9(a), 8(a), 9(e), 8(d))). This fact can be attributed to the additional discretization error introduced by approximating the normal derivative.

6.1.2 Time evolution of the error

Figure 10: Symbols of the different methods.

Since we have the exact solution u_{ex} (6.2) at hand, we compute in the sequel e^n, the ℓ^2-error at $t = n\Delta t$ divided by the energy of the exact solution in the computational domain:

$$e^n = \|u_{\text{ex}}^n - u_{\text{num}}^n\|_2 / \|u_{\text{ex}}^n\|_2,$$

where the spatial ℓ^2-norm is given by

$$\|u^n\|_2^2 = \Delta x \sum_{j=1}^{J-1} |u_j^n|^2, \quad n \in \mathbb{N}_0.$$

Here, u_{num} denotes the numerical solution obtained by the selected method. We will call this the relative error. We identify each method with the help of the symbolic representation given in Fig. 10. The different methods realizing transparent boundary conditions are divided into *four groups*. The first three groups include all methods using finite differences in the interior domain and the fourth group consists of the methods that employ finite elements in the computational domain.

Fig. 11 shows the evolution of the spatial relative ℓ^2-error for all proposed methods of Table 2 in a logarithmic plot. For an easier comparison the Arnold-Ehrhardt method (solid line with circled markers) is again included in each subsequent plot. It is obvious from the Fig. 11 that the maximal ℓ^2-error is located around $t = 0.5$ is dominated by the discretization error (except for the
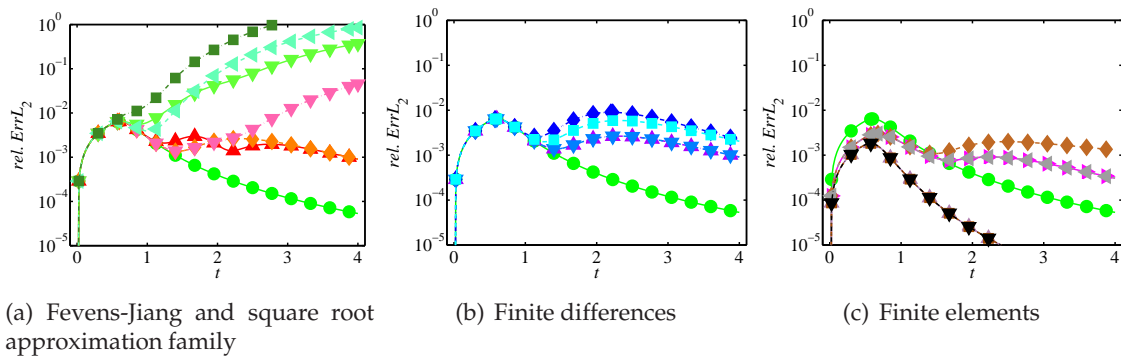
(a) Fevens-Jiang and square root approximation family

(b) Finite differences

(c) Finite elements

Figure 11: Example 1: Time evolution of the spatial ℓ^2-error divided by the ℓ^2-norm of the exact solution for various methods and the discretization: $J=1500$ spatial grid points ($\Delta x=0.01$) and a time step $\Delta t=10^{-3}$.

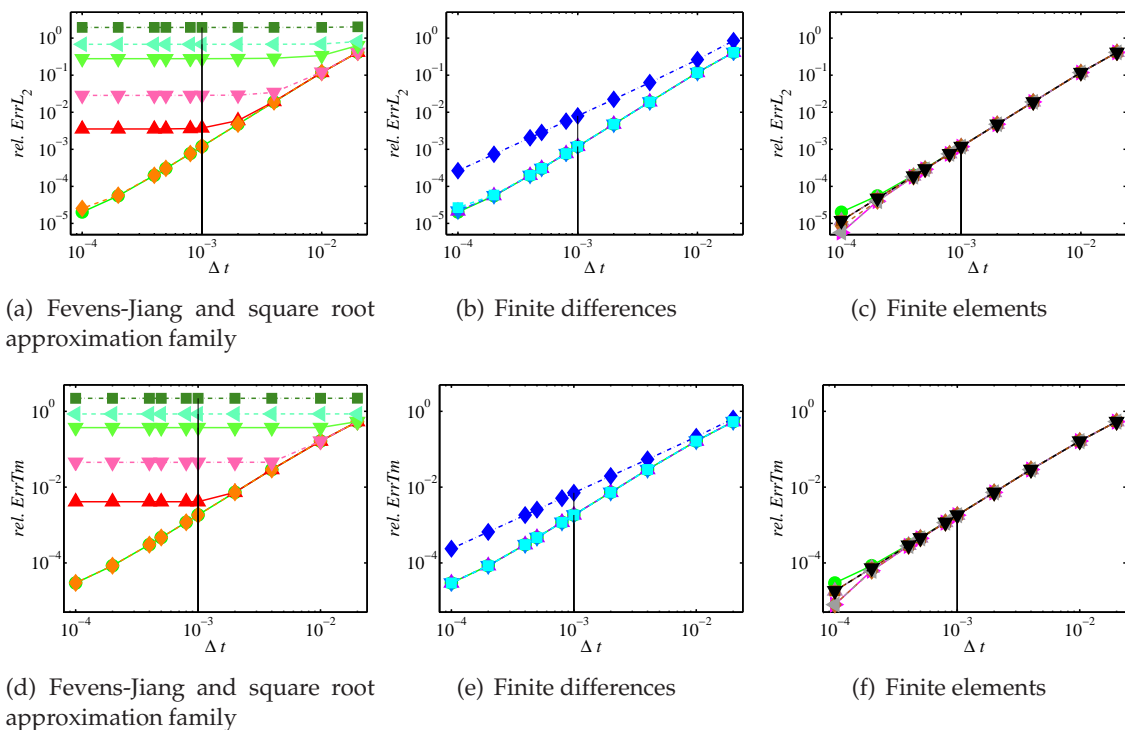(a) Fevens-Jiang and square root approximation family

(b) Finite differences

(c) Finite elements

(d) Fevens-Jiang and square root approximation family

(e) Finite differences

(f) Finite elements

Figure 12: Example 1: $rel.ErrL_2$ (a)-(c) and $ErrTm$ (d)-(f) vs. Δt for $\Delta x=4\cdot10^{-4}$.

Fevens-Jiang family). However, reducing the discretization error by choosing a much finer grid in space and/or time would lead to an unrealistic parameter setting for a 1D problem. For the behaviour of the error using smaller values of the step sizes Δx and Δt we refer to Section 6.1.3).

For all calculations the time step size is $\Delta t=10^{-3}$. The spatial discretization is done using $J=1500$ grid points, i.e., $\Delta x=0.01$.

Fig. 11(a) shows the evolution of the spatial relative ℓ^2-error for the methods of the Fevens-Jiang family. All these approaches yield strong reflections that have a magnitude according to the chosen parameter m in (3.14). One clearly observes in Fig. 11(a) that the square root approximation methods work better. Still there remains some deviation to the reference curve and especially the error for the Szeftel method shows a considerable increase in the long time. Fig. 11(b) confirms the findings from the preceding contour plots. The results arising from the Baskakov-Popov method are slightly worse than those obtained by the PML FD method. The best result in this finite difference group, are the time discrete FD method and the Pole FD method, that are indistinguishable. Finally, Fig. 11(c) shows the evolution of the ℓ^2-error for the methods using finite elements in the interior domain. The pairs Pole FEM 1 and FEM 1 coincide as well as Pole FEM 2 and FEM 2. Moreover, the maximum of the error curve of the FEM methods is clearly below the error curve of the Arnold-Ehrhardt method. The finite element methods of order two coincide. They outperform the other methods by far. In Section 6.1.3 the convergence of the methods will be analyzed more closely. The strongest reflections in this group arise from the PML FEM 1 implementation.

6.1.3 Convergence analysis

In order to illustrate the remarks at the beginning of this Section 6 about the order of convergence and to understand the influences of the step sizes Δt and Δx on the numerical solution quality, we perform different simulations for all the methods on different space-time meshes.

We decided to compute the following two *error functions*

$$rel.ErrTm = \max_{0<n<N} \|u_{\text{ex}}^n - u_{\text{num}}^n\|_2 / \|u_{\text{ex}}^n\|_2,$$

$$rel.ErrL_2 = \left(\Delta t \sum_{n=1}^{N} \|u_{\text{ex}}^n - u_{\text{num}}^n\|_2^2 / \|u_{\text{ex}}^n\|_2^2 \right)^{1/2}, \tag{6.3}$$

where $N\Delta t = T_f$. $rel.ErrTm$ is the maximal relative ℓ^2-error over all time levels n, $0<n<N$, and $rel.ErrL_2$ denotes the spatial and temporal ℓ^2-error scaled with the norm of the exact solution.

Fig. 12 shows the convergence of the methods w.r.t. the temporal step size Δt for fixed $\Delta x = 4 \cdot 10^{-4}$. Analogously, the Fig. 13 shows the convergence of the methods w.r.t. the spatial step size Δx for fixed $\Delta t = 10^{-4}$.

If the temporal ℓ^2-error $rel.ErrL_2$ is measured (Figs. 12 and 13 (a)-(d)) one observes in each case except for the method of Baskakov and Popov a $\mathcal{O}(\Delta x^{p+1})$ resp. $\mathcal{O}(\Delta t^2)$ behaviour. However, the error curves for the three methods of the Fevens-Jiang family in Figs. 12(a) and 13(a) exhibit a very early saturation and lead to a plateau, i.e., from a certain (quite coarse) discretization it is not possible to further reduce the error by reducing the step sizes. This is an inherent error in this group of methods. Furthermore, it can be deduced that the reflections due to the truncation are about $2 \cdot 10^{-2}$ for the Shibata method
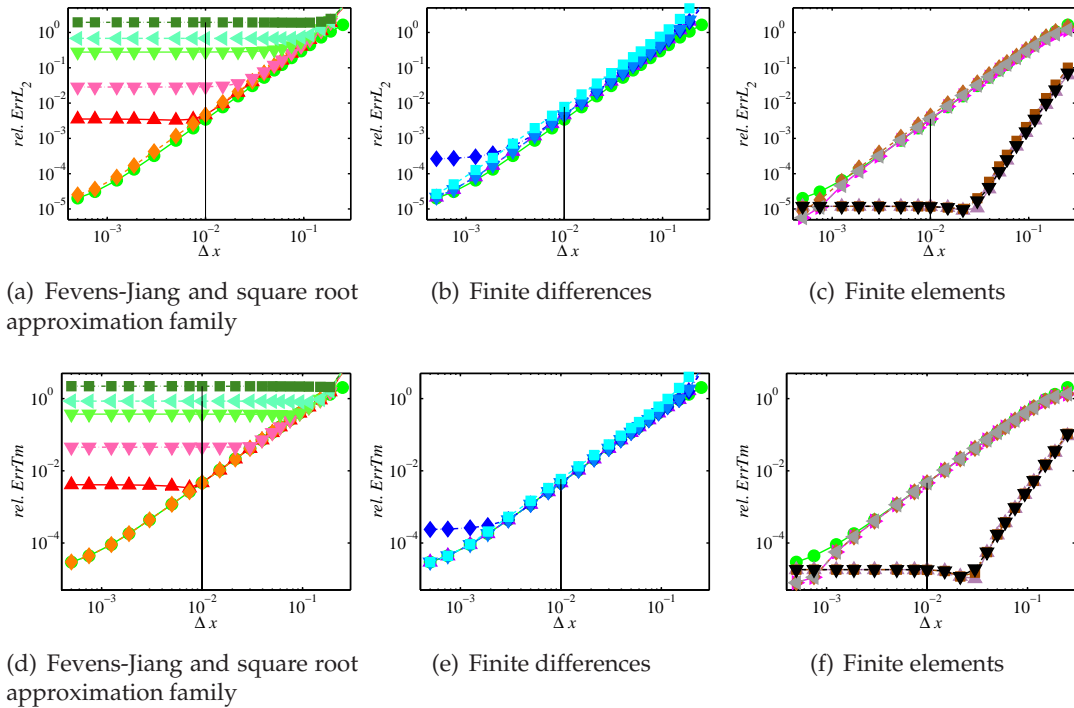
(a) Fevens-Jiang and square root approximation family

(b) Finite differences

(c) Finite elements

(d) Fevens-Jiang and square root approximation family

(e) Finite differences

(f) Finite elements

Figure 13: Example 1: $rel.ErrL_2$ (a)-(d) and $ErrTm$ (e)-(h) vs. Δx for $\Delta t = 10^{-4}$.

($m=2$), 10^{-2} for the Kuska method ($m=3$) and $8 \cdot 10^{-3}$ for the Fevens-Jiang method ($m=4$). The methods of the square root approximation group in Figs. 12(a) and 13(a) also show some saturation, but at a lower level. The truncation error of the Szeftel method is about $8 \cdot 10^{-4}$. Taking into account the fact that the Szeftel method uses 3 coefficients only, this is an excellent result. For the discretization parameters $\Delta t = 10^{-3}$ and $\Delta x = 10^{-2}$ the error for the Bruneau-Di Menza method saturates at about $2 \cdot 10^{-4}$, which can be attributed to the truncation. The thickness of the PML and the number of coefficients in the Pole condition and in the Padé approximation — in each case 20 coefficients are used — is too large to observe the truncation error. Fig. 12(c) shows a second order convergence for $\Delta t \to 0$, except for the Baskakov-Popov method, where a $\mathcal{O}(\Delta t^{3/2})$ behaviour is observed. Fig. 13(c) shows a $\mathcal{O}(\Delta x^2)$ convergence in the ℓ^2-error for the methods using linear finite elements, and a $\mathcal{O}(\Delta x^4)$ convergence for the ℓ^2-error for finite elements of degree 2. The FEM 2 methods perform better than expected.

6.1.4 Computational effort

Figs. 14 and 15 show the cpu time as a function of the number of time steps. For a fine spatial mesh, Fig. 14 ($J = 30000$ unknowns) the solution of the linear system is the most time consuming part of the algorithm. Hence, the different methods can hardly be distinguished. In Fig.15 where we chose a coarser mesh with 1500 grid points one can
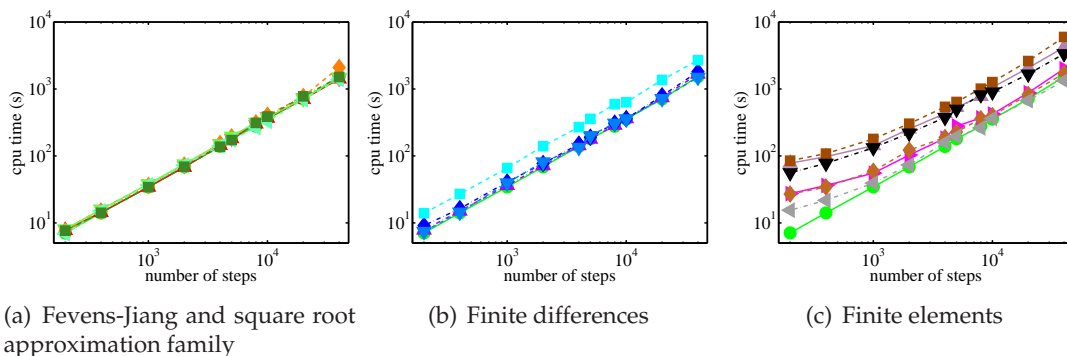
(a) Fevens-Jiang and square root approximation family

(b) Finite differences

(c) Finite elements

Figure 14: Example 1: Number of steps vs. cpu time for various methods using a fine grid, $\Delta x = 4 \cdot 10^{-4}$.

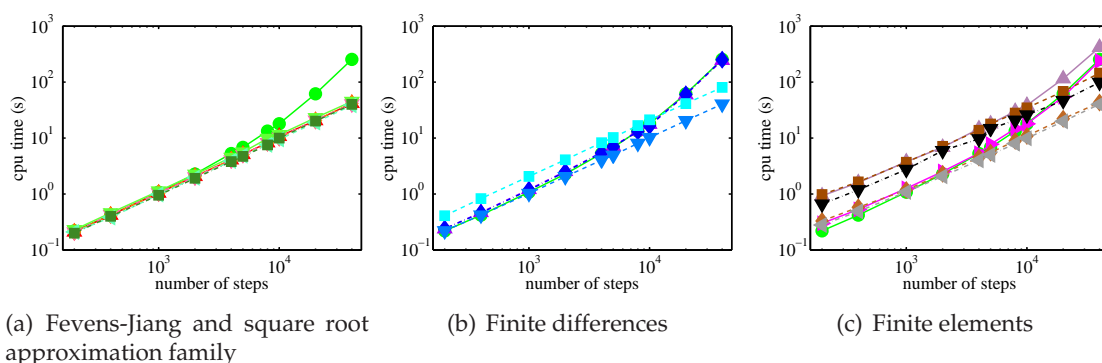(a) Fevens-Jiang and square root approximation family

(b) Finite differences

(c) Finite elements

Figure 15: Example 1: Number of steps vs. cpu time for various methods using $\Delta x = 0.01$.

(a) Fevens-Jiang and square root approximation family
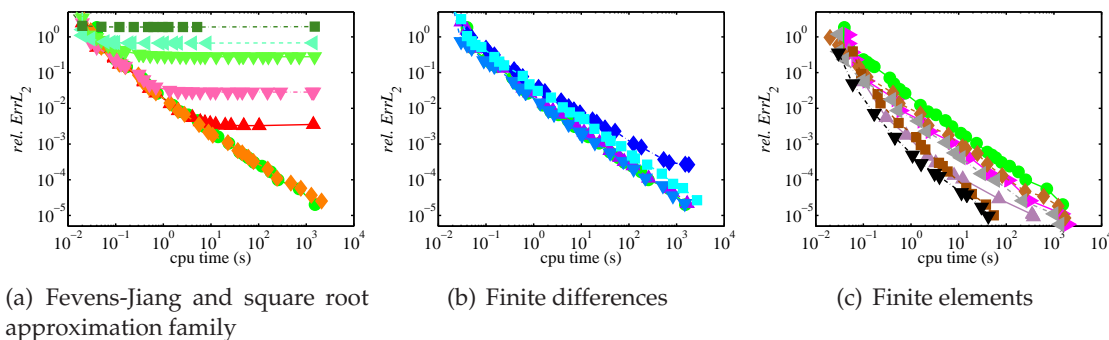
(b) Finite differences

(c) Finite elements

Figure 16: Example 1: Work precision diagrams. For $\Delta t = 2 \cdot 10^{-2}, \cdots, 1 \cdot 10^{-4}$ and $\Delta x = 0.2, \cdots, 4 \cdot 10^{-4}$, the smallest error obtained with the least cpu-time is shown.

clearly see that the Arnold-Ehrhardt, the FD, the FEM 1, FEM 2 and the Baskakov-Popov methods do not scale linearly in N and that the quadratic operation count of the direct convolution starts to dominate the computational costs. The comparatively high cpu time consumption of the PML FD method has to be attributed to the simple choice of the PML (linear damping, fixed layer thickness and uniform discretization). The results for PML
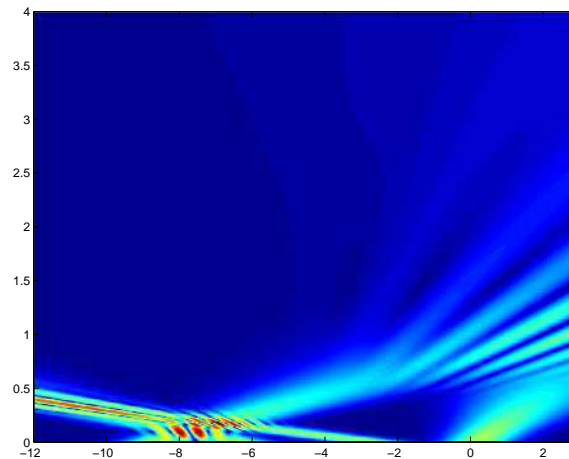
Figure 17: Example 2: Contour plot of exact solution.

FEM methods show that with a good choice of parameters, the PML method competes very well.

Fig. 16 shows the smallest error obtained at the minimal cost. For the Fevens-Jiang family Fig. 16 (a) the relative ℓ^2-error saturates at levels around 1. The saturation levels for Szeftel's and Di Menza's method in Fig. 16 (a) are much lower. The comparison of the methods based on finite elements with the finite difference method of Arnold-Ehrhardt in Fig. 16 (c) reveals that the FEM methods in general outperform the finite difference methods, and that the quadratic finite element methods are superior to linear finite element methods.

6.2 Numerical Example 2: Four Gaussian beams

Again the computational domain is chosen to be $\Omega_{int} =]-12,3[$ and the final time of simulation is $T_f = 4$. In order to point out some weakness of the Fevens-Jiang-type methods that are designed for one certain wave number we compute the evolution of four Gaussian beams of the form (6.1) centered at $x_c = -9, -6, -2, 0$, with the different wave numbers $k_0 = 5, -7, -12, 2$. The initial data is cut-off close to $x_l = -12$, $x_r = 3$ which does not influence the numerical results.

6.2.1 Contour plot of the solution

Fig. 17 shows a contour plot of the solution. It can be observed that we have two faster beams going to the left and two slower ones traveling to the right. Moreover, the two slow beams are crossing each other approximately at the right boundary $x_r = 3$.

6.2.2 Time evolution of error

The following Fig. 18 presents the evolution of the spatial ℓ^2-error for all proposed methods. For an easier comparison the Arnold-Ehrhardt method (solid line with circled mark-
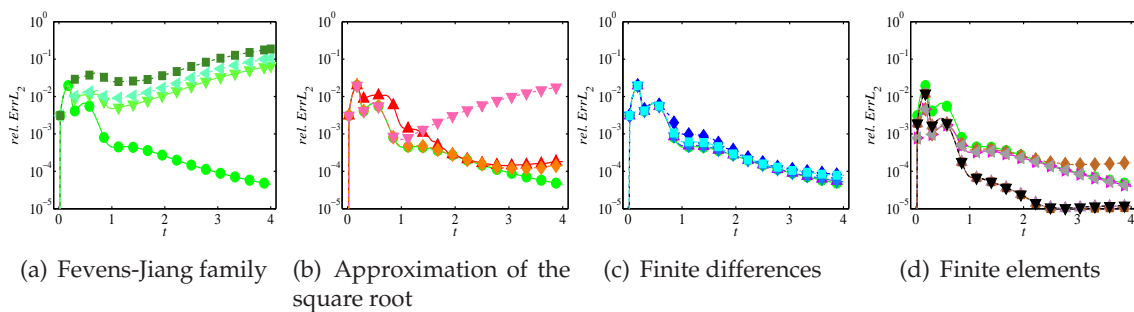
(a) Fevens-Jiang family   (b) Approximation of the   (c) Finite differences   (d) Finite elements
                              square root

Figure 18: Example 2: Time evolution of the spatial ℓ^2-error for the fixed discretization: $J = 1500$ spatial grid points and a time step $\Delta t = 10^{-3}$.
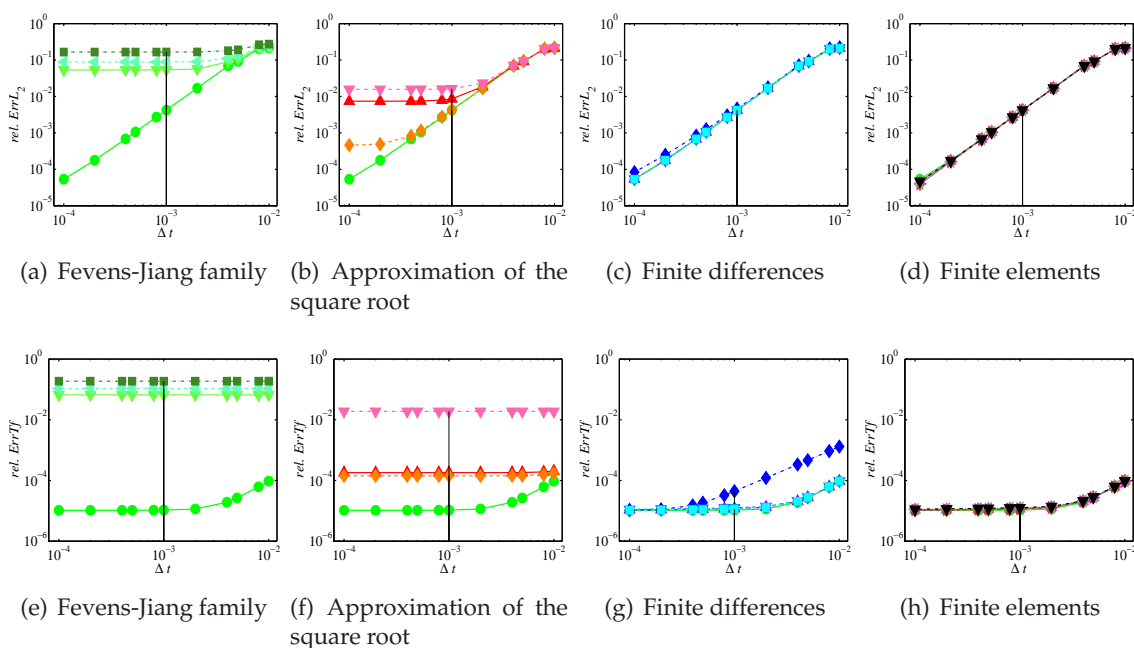

(a) Fevens-Jiang family   (b) Approximation of the   (c) Finite differences   (d) Finite elements
                              square root

(e) Fevens-Jiang family   (f) Approximation of the   (g) Finite differences   (h) Finite elements
                              square root

Figure 19: Example 2: $rel.ErrL_2$ (a)-(d), $ErrTf$ (e)-(h) vs. Δt for $\Delta x = 5 \cdot 10^{-4}$.

ers) is again included in each subsequent plot. Note that we have to take a single value for the modulus of the wave number for all three methods of the Fevens-Jiang family and the pole condition. We decided to choose the mean of the modulus, i.e., $k_0 = 6.5$.

It is obvious from the Fig. 18 that the maximal ℓ^2-error located around $t = 0.5$ is dominated by the discretization error (except for the Fevens-Jiang family).

The methods in subplot (a): Fevens-Jiang, Kuska and Shibata and the method of Szeftel all show strong reflections. This is due to the fact that they are tailored to be transparent for one k_0.
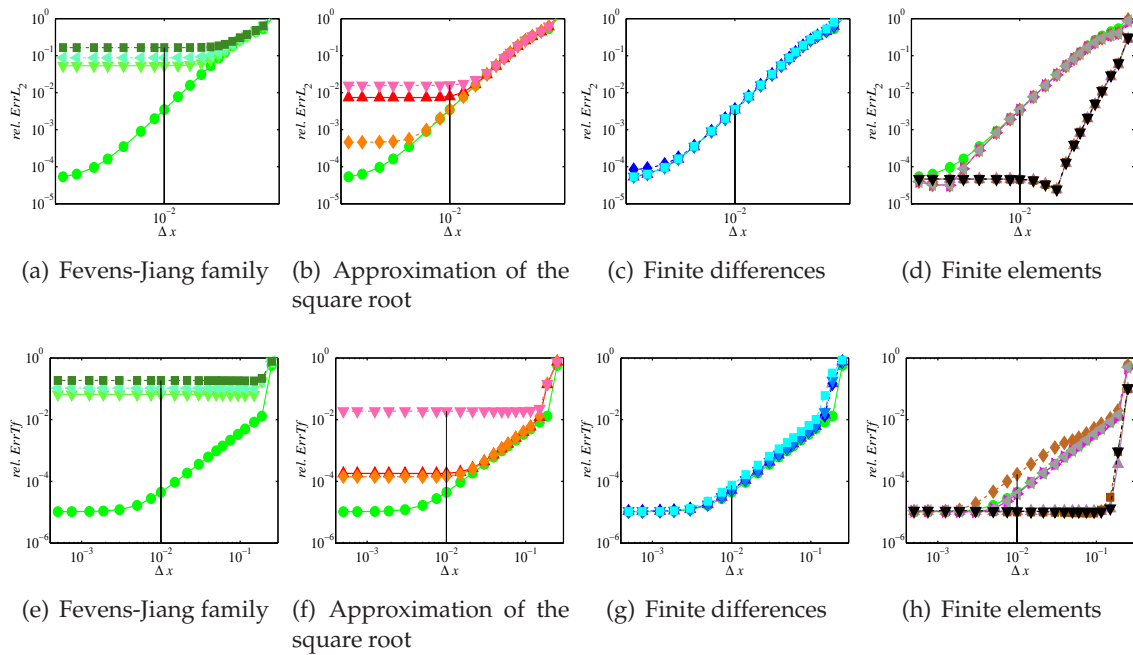
(a) Fevens-Jiang family   (b) Approximation of the square root   (c) Finite differences   (d) Finite elements

(e) Fevens-Jiang family   (f) Approximation of the square root   (g) Finite differences   (h) Finite elements

Figure 20: Example 2: $rel.ErrL_2$ (a)-(d) and $ErrTf$ (e)-(h) vs. Δx for $\Delta t = 10^{-4}$.

(a) Fevens-Jiang family   (b) Approximation of the square root   (c) Finite differences   (d) Finite elements
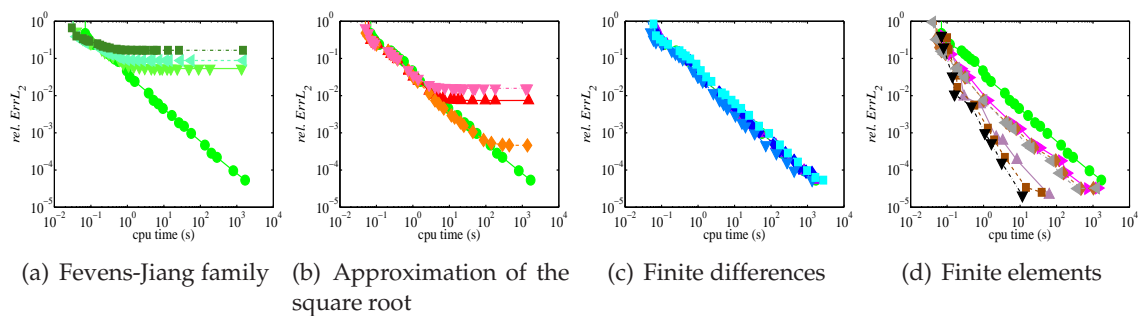
Figure 21: Example 2: Work precision diagrams. For $\Delta t = 2 \cdot 10^{-2}, \cdots, 1 \cdot 10^{-4}$ and $\Delta x = 0.2, \cdots, 4 \cdot 10^{-4}$, the smallest relative error obtained with the least cpu-time is shown.

6.2.3 Convergence analysis

Figs. 19 and 20 show the convergence of the methods w.r.t. the step sizes Δt and Δx. Here we computed the two *error functions*

$$rel.ErrTf = \|u_{\text{ex}}^N - u_{\text{num}}^N\|_2 / \|u^N\|_2,$$

$$rel.ErrL_2 = \left(\Delta t \sum_{n=1}^{N} \|u_{\text{ex}}^n - u_{\text{num}}^n\|_2^2 / \|u_{\text{ex}}^n\|_2 \right)^{1/2}, \tag{6.4}$$
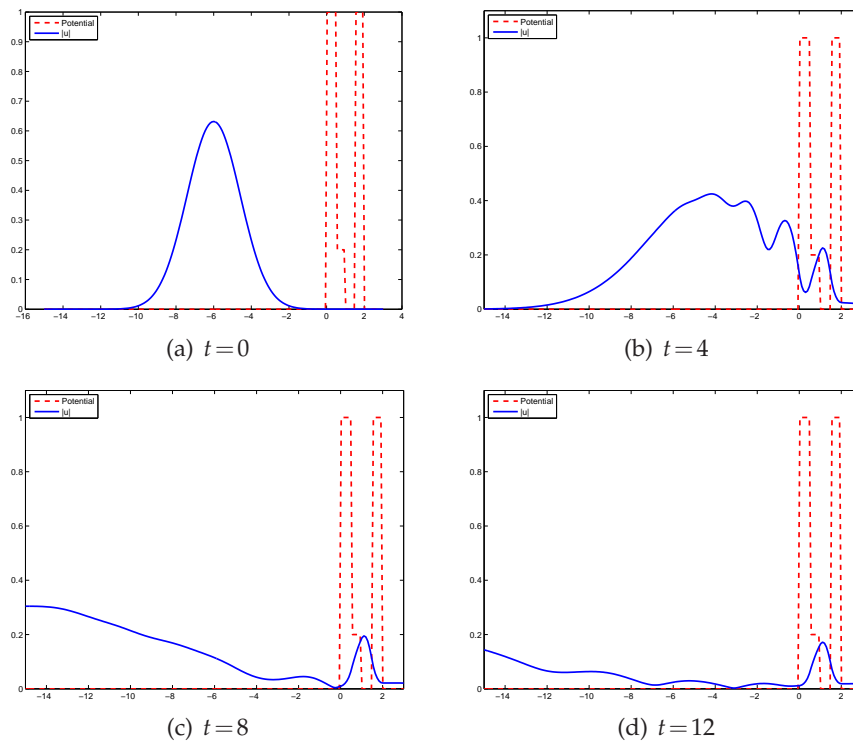
Figure 22: Example 3: Evolution of $|u|$, solution to Schrödinger equation with potential (6.5).

where $N\Delta t = T_f$. $rel.ErrTf$ is the relative ℓ^2-error at the final time T_f and $rel.ErrL_2$ denotes the spatial and temporal ℓ^2-error scaled with the norm of the exact solution.

If the relative ℓ^2-error $rel.ErrL_2$ is measured, one observes in each case an $\mathcal{O}(\Delta t^2)$ resp. $\mathcal{O}(\Delta x^2)$ behaviour. Fig. 19(d) shows the second order convergence for $\Delta t \rightarrow 0$. Fig. 20(d) shows a $\mathcal{O}(\Delta x^2)$ convergence in the ℓ^2-error for the methods using linear finite elements, and again a $\mathcal{O}(\Delta x^4)$ convergence, which is better than expected, for the ℓ^2-error for finite elements of degree 2. The FEM 2 method performs better than expected.

6.2.4 Computational effort

The plots showing cpu-time over the number of time-steps are identical to those for the Example 1. Fig. 21 shows the work precision diagrams for this example, the smallest error obtained at the minimal cost. The results are similar compared to ones obtained for Example 1. For the Fevens-Jiang family in Fig. 21(a), the relative ℓ^2-error saturates at levels above 0.1. This is due to the fact that the ℓ^2-norm of the exact solution does not tend to 0 as rapidly as in Example 1. The comparison of the methods based on finite elements with the finite difference method of Arnold-Ehrhardt in Fig. 21(d) again reveals, even more clearly in this example, that the FEM methods in general outperform the finite difference methods, and that the quadratic finite element methods are superior to linear finite element methods.
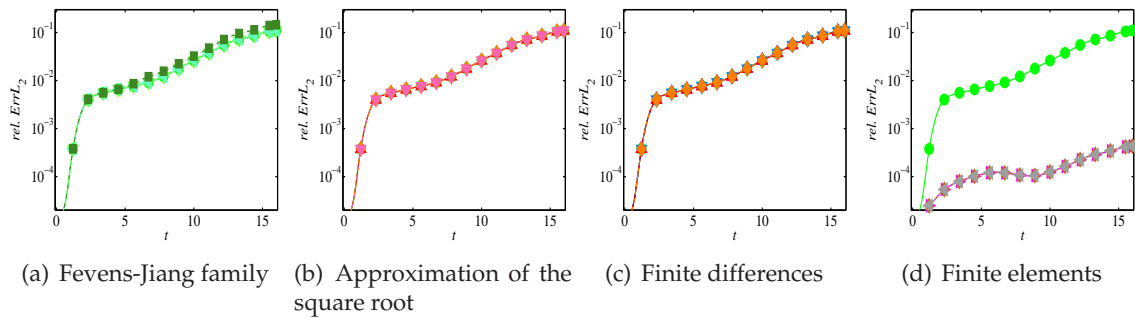
(a) Fevens-Jiang family   (b) Approximation of the square root   (c) Finite differences   (d) Finite elements

Figure 23: Example 3: Time evolution of the spatial relative ℓ^2-error for the fixed discretization: $J = 6.000$ spatial grid points $(\Delta x = 3 \cdot 10^{-3})$ and a time step $\Delta t = 10^{-3}$.
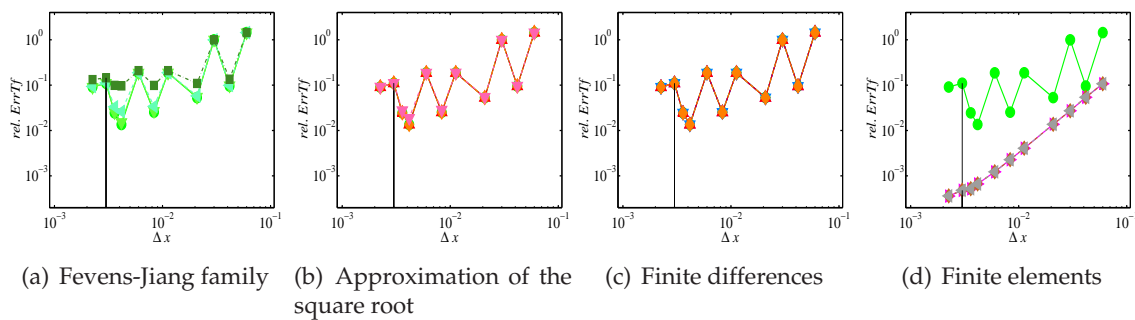

(a) Fevens-Jiang family   (b) Approximation of the square root   (c) Finite differences   (d) Finite elements

Figure 24: Example 2: Errors $rel.ErrTf$ (a)-(d) vs. Δx for $\Delta t = 2 \cdot 10^{-4}$.

6.3 Numerical Example 3: Application from quantum mechanics

Finally, in the last numerical example we want to present some practical application from quantum mechanics. Thus, we consider the Schrödinger equation with a *double barrier stepped quantum well* (DBSQW) potential, i.e., we consider the following equation

$$i\partial_t u = -\frac{1}{2}\partial_x^2 u + V(x,t)u, \quad x \in \mathcal{R}, t > 0,$$

$$V(x,t) = \begin{cases} 25/2 & x \in [0,0.5] \cup [1.5,2], \\ 5/2 & x \in (0.5,1), \\ 0 & \text{elsewhere}, \end{cases}$$

$$\lim_{|x|\to\infty} u(x,t) = 0,$$

$$u(x,0) = \sqrt[4]{\frac{2}{\pi\sigma^2}}\exp\left(-\frac{(x-x_c)^2}{\sigma^2} + ik_0(x-x_c)\right),$$

(6.5)

with the parameters $\sigma = 2$, $x_c = -6$, $k_0 = \sqrt{7}$, on the computational domain $\Omega_{int} = [-15,3]$.

This test is not a completely realistic test of quantum mechanics, but allows to see the trap particles in the potential hole. We plot the evolution of the modulus of the solution in
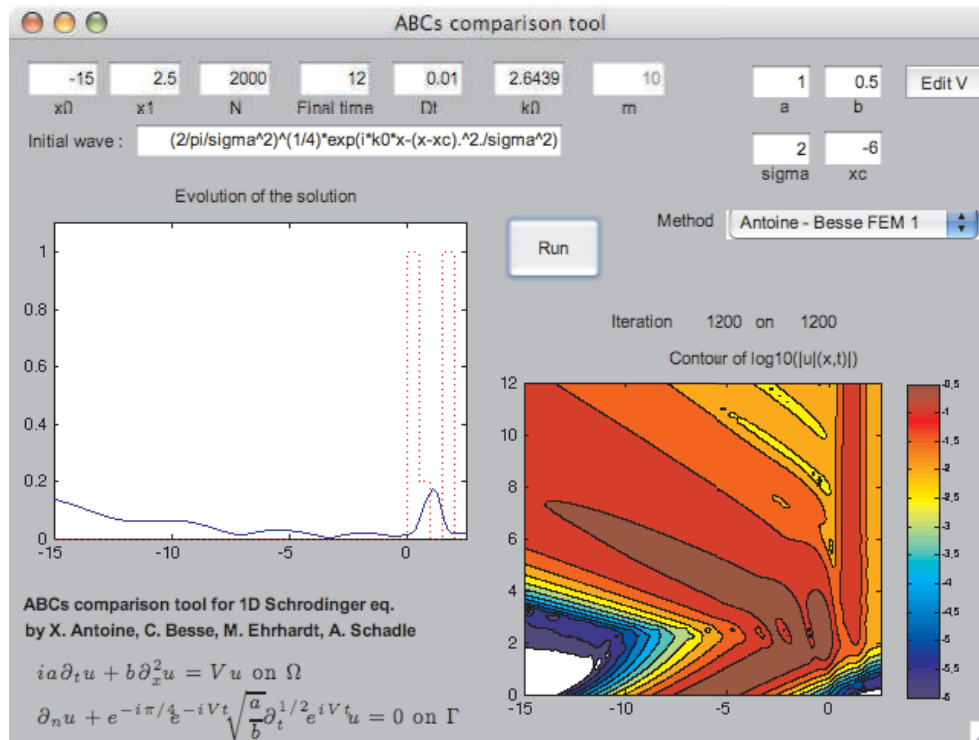
Figure 25: Screenshot of the Matlab software (Version 3) solver.

Fig. 22 for different values of the time t. We clearly see the wave captured in the potential hole.

Since we do not dispose of an exact explicit solution, we compute a reference solution by the FEM 2 scheme on the computational domain $[-18,6]$, with $J=16.000$ ($\Delta x = 1.5 \cdot 10^{-3}$) and $\Delta t = 10^{-4}$. The final time is $T_f = 16$.

In Fig. 23 we plot the evolution of the relative ℓ^2-error. There is a clear difference between the finite element and the finite difference methods. The later exhibit a much bigger error. This is due to the fact that in this example a non-smooth step function as potential is used. Therefore a reduction in the rate of convergence for the finite-difference approximation is observed as can be seen in Fig. 24.

Remark 6.1. There exists supplementary software (written in Matlab) with a graphical user interface. Currently it covers the following implementations of TBCs/ABCs: (FD, Arnold-Ehrhardt, Baskakov-Popov, Di Menza, Fevens-Jiang, Kuska, Pade, PML, PML-FEM, Pole Condition, Shibata, Szeftel). Fig. 25 shows a screen shot of the software (Version 3) solver.

This software can be downloaded from the authors' home pages or at the site
`http://www.tbc-review.de.vu`.

7   Conclusions

In this review we have presented several different techniques to solve numerically the time-dependent Schrödinger equation on unbounded domains. We discussed and compared several implementations of the classical transparent boundary condition and absorbing boundary conditions into finite difference and finite element discretizations. We mainly addressed the one-dimensional case but also touched upon the situation in two space dimensions and the cubic nonlinear case. Finally, we concluded with several numerical examples comparing the proposed boundary conditions w.r.t. different kind of errors and the cpu time. Moreover, we present a freely available graphical user interface (written in Matlab) covering most of the presented approaches.

8   Future research directions

The next natural step is to carry some of the ideas of the (semi-)discrete TBCs to the nonlinear case. We refer to the recent paper [136] for a first step in this direction. However, all previously used integral transform techniques does not work (in general) for nonlinear equations and thus a valuable research direction seems to use discrete multiple scales approaches instead in order to construct discrete ABCs for nonlinear evolution equations.

Future challenging problems for artificial boundary conditions will arise from high-dimensional problems (e.g. the Black-Scholes equation for the pricing of multi-asset American options) and from large nonlinear systems, possibly including different time scales (e.g. systems arising from climate modelling).

Acknowledgments

A   Appendix: Fractional operators

The integration of real order $p > 0$ of a function f, denoted by $I_t^p f(t)$, is given by the *Riemann-Liouville formula*

$$I_t^p f(t) = \frac{1}{\Gamma(p)} \int_0^t (t-\tau)^{p-1} f(\tau) d\tau, \tag{A.1}$$

where $\Gamma(z) = \int_0^{+\infty} e^{-t} t^{z-1} dz$ is the Gamma function. This definition allows to define the derivative $\partial_t^{k-\alpha} f(t)$ of order $k-\alpha > 0$ of a function f, with $k \in \mathbb{N}$ and $0 < \alpha \leq 1$:

$$\partial_t^{k-\alpha} f(t) = \frac{1}{\Gamma(\alpha)} \frac{d^k}{dt^k} \int_0^t (t-\tau)^{\alpha-1} f(\tau) d\tau. \tag{A.2}$$

Other approaches to define fractional derivatives are due to Grünwald-Letnikov or Caputo, e.g. Many properties of derivative operators can be extended from the integer to the non-integer case, like the Leibniz rule and the chain rule [103], e.g.

For our applications, the Laplace transform of fractional derivatives plays an important role:

$$F(s) = \mathcal{L}\{f(t); s\} = \int_0^{+\infty} e^{-st} f(t) dt, \quad s \in \mathbb{C}. \tag{A.3}$$

The existence of the above integral is linked to the property that f must be of exponential order. The original function f is recovered by the inverse Laplace transform

$$f(t) = \mathcal{L}^{-1}\{F(s); t\} = \int_{c-i\infty}^{c+i\infty} e^{-st} f(t) dt. \tag{A.4}$$

Here, $c = \mathrm{Re}(s) > c_0$, where c_0 lies in the right half plane of absolute convergence of the Laplace integral (A.3). Using the properties of the convolution $\star$ related to the Laplace transform, one gets

$$I_t^p f(t) = \frac{1}{\Gamma(p)} (t^{p-1} \star f)(t), \quad p > 0,$$

since $\mathcal{L}\{t^{p-1}; s\} = \Gamma(p) s^{-p}$. The Laplace transform of the Riemann-Liouville fractional derivative of order $p > 0$ satisfies

$$\mathcal{L}\{\partial_t^p f(t); s\} = s^p F(s) - \sum_{k=0}^{n-1} s^k [\partial_t^{p-k-1} f(t)]_{|t=0},$$

for $n-1 \leq p < n$.

B Appendix: $\mathcal{Z}$-transformation

One main tool of this work is the $\mathcal{Z}$-transformation [43] which is the discrete analogue of the Laplace-transformation. The $\mathcal{Z}$-transformation can be applied to the solution of linear difference equations in order to reduce the solutions of such equations into those of algebraic equations in the complex z-plane. In this paper we used it to solve the finite difference schemes in the exterior domains in order to construct the discrete TBCs in Sections 2.3 and 2.5.

Definition B.1 ($\mathcal{Z}$-transformation [43])**.** The formal connection between a sequence and a complex function given by the correspondence

$$\mathcal{Z}\{f_n\} = \hat{f}(z) := \sum_{n=0}^{\infty} f_n z^{-n}, \quad z \in \mathbb{C}, \quad |z| > R_{\hat{f}}, \tag{B.1}$$

is called $\mathcal{Z}$-transformation. The function $\hat{f}(z)$ is called $\mathcal{Z}$-transformation of the sequence $\{f_n\}$, $n = 0, 1, \cdots$ and $R_{\hat{f}} \geq 0$ denotes the radius of convergence.

The discrete analogue of the Differentiation Theorem for the Laplace transformation is the *shifting theorem*:

Theorem B.1 (Shifting Theorem [43])**.** *If the sequence* $\{f_n\}$ *is exponentially bounded, i.e., there exist* $C > 0$ *and* c_0 *such that*

$$|f_n| \leq C e^{c_0 n}, \qquad n = 0, 1, \cdots,$$

then the $\mathcal{Z}$-*transformation* $\hat{f}(z)$ *is given by the Laurent series* (B.1) *and for the shifted sequence* $\{g_n\}$ *with* $g_n = f_{n+1}$ *holds*

$$\mathcal{Z}\{f_{n+1}\} = z\hat{f}(z) - zf_0. \tag{B.2}$$

The initial values enter into the transformation of the shifted sequence. As a useful consequence of the shifting theorem we have:

$$\mathcal{Z}\{f_{n+1} \pm f_n\} = (z \pm 1)\hat{f}(z) - zf_0. \tag{B.3}$$

The discrete convolution $f_n * g_n$ of two sequences $\{f_n\}$, $\{g_n\}$, $n = 0, 1, \cdots$ is defined by $\sum_{k=0}^{n} f_k g_{n-k}$. For the $\mathcal{Z}$-transformation of a convolution of two sequences we formulate the following theorem:

Theorem B.2 (Convolution Theorem [43])**.** *If* $\hat{f}(z) = \mathcal{Z}\{f_n\}$ *exists for* $|z| > R_{\hat{f}} \geq 0$ *and* $\hat{g}(z) = \mathcal{Z}\{g_n\}$ *for* $|z| > R_{\hat{g}} \geq 0$, *then there also exists* $\mathcal{Z}\{f_n * g_n\}$ *for* $|z| > \max(R_{\hat{f}}, R_{\hat{g}})$ *with*

$$\mathcal{Z}\{f_n * g_n\} = \hat{f}(z)\hat{g}(z). \tag{B.4}$$

Note that (B.4) is nothing else but an expression for the Cauchy product of two power series. Finally, we present the *inverse $\mathcal{Z}$-transformation* which is essential for formulating the discrete TBCs in physical space.

Theorem B.3 (Inverse $\mathcal{Z}$-transformation [43])**.** *If* $\{f_n\}$ *is an exponentially bounded sequence and* $\hat{f}(z)$ *the corresponding* $\mathcal{Z}$-*transformation then the inverse* $\mathcal{Z}$-*transformation is given by*

$$f_n = \mathcal{Z}^{-1}\left\{\hat{f}(z)\right\} = \frac{1}{2\pi i} \oint_C \hat{f}(z) z^{n-1} dz, \qquad n = 0, 1, \cdots, \tag{B.5}$$

where C denotes a circle around the origin with sufficiently large radius.

The most important formula is the *inverse $\mathcal{Z}$-transformation of a product*:

$$\mathcal{Z}^{-1}\left\{\hat{f}(z)\hat{g}(z)\right\} = f_n * g_n = \sum_{k=0}^{n} f_k g_{n-k}. \tag{B.6}$$

References

[1] A. Ahland, D. Schulz and E. Voges, *Accurate mesh truncation for Schrödinger equations by a perfectly matched layer absorber: Application to the calculation of optical spectra*, Phys. Rev. B **60** (1999), 5109–5112.

[2] B. Alpert, L. Greengard and T. Hagstrom, *Rapid evaluation of nonreflecting boundary kernels for time–domain wave propagation*, SIAM J. Numer. Anal. **37** (2000), 1138–1164.

[3] B. Alpert, L. Greengard and T. Hagstrom, *Nonreflecting boundary conditions for the time-dependent wave equation*, J. Comput. Phys. **180** (2002), 270–296.

[4] I. Alonso–Mallo and N. Reguera, *Weak ill-posedness of spatial discretizations of absorbing boundary conditions for Schrödinger–type equations*, SIAM J. Numer. Anal. **40** (2002), 134–158.

[5] I. Alonso–Mallo and N. Reguera, *Discrete absorbing boundary conditions for Schrödinger–type equations. construction and error analysis*, SIAM J. Numer. Anal. **41** (2003), 1824–1850.

[6] I. Alonso–Mallo and N. Reguera, *Adaptive absorbing boundary conditions for Schrödinger–type equations*, in: Proceedings of the sixth international conference on mathematical and numerical aspects of wave propagation, WAVES 2003, Jyväskylä, Finland, Springer, 2003.

[7] I. Alonso–Mallo and N. Reguera, *Discrete absorbing boundary conditions for Schrödinger–type equations. Practical Implementation*, Math. Comp. **73** (2004), 127–142.

[8] X. Antoine and C. Besse, *Construction, structure and asymptotic approximations of a microdifferential transparent boundary condition for the linear Schrödinger equation*, J. Math. Pures Appl. IX. Sér. **80** (2001), 701–738.

[9] X. Antoine and C. Besse, *Unconditionally stable discretization schemes of non–reflecting boundary conditions for the one–dimensional Schrödinger equation*, J. Comput. Phys. **188** (2003), 157–175.

[10] X. Antoine and C. Besse, *Artificial boundary conditions for Schrödinger-type equations and their numerical approximation*, in: Advances in Scientific Computing and Applications, Y.Y. Lu, W.W. Sun and T. Tang Eds., Science Press, Beijing/New York, 2004, pp. 8–21.

[11] X. Antoine, C. Besse and S. Descombes, *Artificial boundary conditions for one-dimensional cubic nonlinear Schrödinger equations*, SIAM J. Numer. Anal. **43** (2006), 2272–2293.

[12] X. Antoine, C. Besse and V. Mouysset, *Numerical Schemes for the simulation of the two–dimensional Schrödinger equation using non–reflecting boundary conditions*, Math. Comp. **73** (2004), 1779–1799.

[13] X. Antoine and M. Darbas, *Alternative integral equations for the iterative solution of acoustic scattering problems*, Quat. J. Mech. Appl. Math. **58** (2005), 107–128.

[14] X. Antoine, M. Darbas and Y.Y. Lu, *An improved surface radiation condition for high–frequency acoustics scattering problems*, Comput. Meth. Appl. Mech. Eng. **195** (33-36) (2006), 4060-4074.

[15] A. Arnold, *Numerically absorbing boundary conditions for quantum evolution equations*, VLSI Design **6** (1998), 313–319.

[16] A. Arnold and M. Ehrhardt, *Discrete transparent boundary conditions for wide angle parabolic equations in underwater acoustics*, J. Comput. Phys. **145** (1998), 611–638.

[17] A. Arnold, *Mathematical concepts of open quantum boundary conditions*, Transp. Theory Stat. Phys. **30** (2001), 561–584.

[18] A. Arnold, M. Ehrhardt and I. Sofronov, *Discrete transparent boundary conditions for the Schrödinger equation: fast calculation, approximation, and stability*, Comm. Math. Sci. **1** (2003), 501–556

[19] A. Arnold, M. Ehrhardt, M. Schulte and I. Sofronov, *Discrete transparent boundary conditions for the Schrödinger equation on circular domains*, Preprint No. 41–2007 of the Institute of Mathematics, TU Berlin, November 2007.

[20] G.A. Baker, Jr., *Essentials of Padé Approximants*, Academic Press NY, San Francisco, London, 1975.

[21] V.A. Baskakov and A.V. Popov, *Implementation of transparent boundaries for numerical solution of the Schrödinger equation*, Wave Motion **14** (1991), 123–128.

[22] N. Ben Abdallah, F. Méhats and O. Pinaud, *On an open transient Schrödinger-Poisson system*, Math. Models Methods Appl. Sci. **15** (2005), 667–688.

[23] J.-P. Bérenger, *A perfectly matched layer for the absorption of electromagnetic waves*, J. Comput. Phys. **114** (1994), 185–200.

[24] C. Besse, *A relaxation scheme for the nonlinear Schrödinger equation*, SIAM J. Numer. Anal. **42** (3) (2004), 934–952.

[25] J.M. Bony, *Calcul symbolique et propagation des singularités pour les équations aux dérivées partielles non linéaires*, Ann. Sci. Ec. Norm. Sup. (4ème série) **14** (1981), 209–246.

[26] A. Boutet de Monvel, A.S. Fokas and D. Shepelsky, *Analysis of the global relation for the nonlinear Schrödinger equation on the half-line*, Lett. Math. Phys. **65** (2003), 199–212.

[27] C.H. Bruneau and L. Di Menza, *Conditions aux limites transparentes et artificielles pour l'équation de Schrödinger en dimension 1 d'espace*, C. R. Acad. Sci. Paris, Ser. I **320** (1995), 89–94.

[28] L. Burgnies, O. Vanbésien and D. Lippens, *Transient analysis of ballistic transport in stublike quantum waveguides*, Appl. Phys. Lett. **71** (1997), 803–805.

[29] N. Carjan, M. Rizea and D. Strottman, *Efficient numerical solution of the time–dependent Schrödinger equation for deep tunneling*, Roman. Reports Phys. **55** (2003), 555–579.

[30] H.S. Carslaw and J.C. Jaeger, *Conduction of heat in solids*, Clarendon Press, Oxford, UK, 1959.

[31] T. Cazenave, *An Introduction to Nonlinear Schrödinger Equations*, Textos de Métodos Matemáticos de Universidade Federal de Rio de Janeiro, 26, 1996.

[32] W. C. Chew and W. H. Weedon, *A 3-D Perfectly Matched Medium from modified Maxwell's equations with stretched coordinates*, Micro. Opt. Lett. **7** (13) (1994), 599–604.

[33] J.F. Claerbout, *Coarse grid calculation of waves in inhomogeneous media with application to delineation of complicated seismic structure*, Geophysics **35** (1970), 407–418.

[34] F. Collino, *Perfectly matched absorbing layers for the paraxial equations*, J. Comput. Phys. **131** (1997), 164–180.

[35] F. Collino, *High order absorbing boundary conditions for wave propagation models: straight line boundary and corner cases*, Second International Conference on Mathematical and Numerical Aspects of Wave Propagation (Newark, DE, 1993), 161–171, SIAM, Philadelphia, PA, 1993.

[36] D. Colton and R. Kress, *Integral Equation Methods in Scattering Theory*, Pure and Applied Mathematics (New York), A Wiley-Interscience Publication, John Wiley & Sons, Inc., New York, 1983.

[37] R.A. Dalrymple and P.A. Martin, *Perfect boundary conditions for parabolic water–wave models*, Proc. R. Soc. Lond. A **437** (1992), 41–54.

[38] A. Dedner, D. Kröner, I. Sofronov and M. Wesenberg, *Transparent boundary conditions for MHD simulations in stratified atmospheres*, J. Comput. Phys. **171** (2001), 448–478.

[39] M. Delfour, M. Fortin and G. Payre, *Finite-difference solutions of a nonlinear Schrödinger equation*, J. Comput. Phys. **44** (1981), 277–288.

[40] L. Di Menza, *Approximations numériques d'équations de Schrödinger non linéaires et de modèles associés*, Ph.D. thesis, Université Bordeaux I, 1995.

[41] L. Di Menza, *Absorbing boundary conditions on a hypersurface for the Schrödinger equation in a half–space*, Appl. Math. Lett. **9** (1996), 55–59.

[42] L. Di Menza, *Transparent and absorbing boundary conditions for the Schrödinger equation in a bounded domain*, Numer. Funct. Anal. Opt. **18** (1997), 759–775.

[43] G. Doetsch, *Anleitung zum praktischen Gebrauch der Laplace–Transformation und der Z–Transformation*, R. Oldenburg Verlag München, Wien, 3. Auflage 1967.

[44] E. Dubach, *Nonlinear artificial boundary conditions for the viscous Burgers equation*, Preprint 00/04, Laboratoire de Mathématiques Appliquées, Université de Pau et des Pays de l'Adour, France.

[45] J. Duque, *Solving time–dependent equations of Schrödinger–type using mapped infinite elements*, Int. J. Modern Phys. C **2** (2005), 309–316.

[46] A. Durán and J.M Sanz-Serna, *The numerical integration of relative equilibrium solutions. The nonlinear Schrödinger equation*, IMA J. Numer. Anal. **20** (2000), 235–261.

[47] M. Ehrhardt, *Discrete transparent boundary conditions for parabolic equations*, Z. Angew. Math. Mech. **77** (1997) S2, 543–544.

[48] M. Ehrhardt. *Discrete Artificial Boundary Conditions*, Ph.D. Thesis, Technische Universität Berlin, 2001.

[49] M. Ehrhardt and A. Arnold, *Discrete transparent boundary conditions for the Schrödinger equation*, Riv. Mat. Univ. Parma **6** (2001), 57–108.

[50] M. Ehrhardt and R.E. Mickens, *Solutions to the discrete Airy equation: Application to parabolic equation calculations*, J. Comput. Appl. Math. **172** (2004), 183–206.

[51] M. Ehrhardt and A. Zisowsky, *Fast calculation of energy and mass preserving solutions of Schrödinger-Poisson systems on unbounded domains*, J. Comput. Appl. Math. **187** (2006), 1–28.

[52] M. Ehrhardt and A. Zisowsky, *Nonlocal boundary conditions for higher–order parabolic equations*, Proc. Appl. Math. Mech. (PAMM) **6** (2006), 733–734.

[53] M. Ehrhardt and A. Zisowsky, *Discrete non–local boundary conditions for Split–Step Padé approximations of the one–way Helmholtz equation*, J. Comput. Appl. Math. **200** (2007), 471–490.

[54] M. Ehrhardt, *Discrete transparent boundary conditions for Schrödinger–type equations for non–compactly supported initial data*, Appl. Numer. Math. **58** (2008), 660–673.

[55] M. Ehrhardt and C. Zheng, *Exact artificial boundary conditions for problems with periodic structures*, (accepted for publication: J. Comput. Phys.)

[56] M. Ehrhardt, H. Han and C. Zheng, *Numerical solution of periodic structure problems with local defects*, Preprint No. 48–2007 of the Institute for Mathematics, TU Berlin, 2007. (submitted to: Commun. Comput. Phys.)

[57] B. Engquist and A. Majda, *Absorbing boundary conditions for the numerical simulation of waves*, Math. Comp. **31** (1977), 629–651.

[58] B. Engquist and A. Majda, *Radiation boundary conditions for acoustic and elastic wave calculations*, Comm. Pure Appl. Math. **32** (1979), 313–357.

[59] T. Fevens and H. Jiang, *Absorbing boundary conditions for the Schrödinger equation*, SIAM J. Sci. Comput. **21** (1999), 255–282.

[60] W.R. Frensley, *Boundary conditions for open quantum systems driven far from equilibrium*, Rev. Mod. Phys. **62** (1990), 745–791.

[61] H. Galicher, *Transparent boundary conditions for the one–dimensional Schrödinger equation with periodic potential at infinity*, submitted to: Commun. Math. Sci., 2007.

[62] D. Givoli, *Non-reflecting boundary conditions*, J. Comput. Phys. **94** (1991), 1–29.

[63] D. Givoli, *Numerical methods for problems in infinite domains*, Studies in Applied Mechanics **33**, Elsevier, 1992.

[64] D. Givoli, *High–order local non–reflecting boundary conditions: a review*, Wave Motion **39** (2004), 319–326

[65] L. Greengard and J. Strain, *A fast algorithm for the evaluation of heat potentials*, Comm. Pure Appl. Math. **43** (1990), 949–963.

[66] C.E. Grosch and S.A. Orszag, *Numerical solution of problems in unbounded regions: coordinate transforms*, J. Comput. Phys. **25** (1977), 273–296.

[67] T. Hagstrom, *Radiation boundary conditions for the numerical simulation of waves*, Acta Numerica **8** (1999), 47–106.

[68] T. Hagstrom, *New results on absorbing layers and radiation boundary conditions*, Topics in computational wave propagation, 1–42, Lect. Notes Comput. Sci. Eng. **31**, Springer, Berlin, 2003.

[69] E. Hairer and G. Wanner, *Solving ordinary differential equations II*, Springer Series in Computational Mathematics, Springer, Berlin, 1991.

[70] E. Hairer, Ch. Lubich, and M. Schlichte, *Fast numerical solution of nonlinear Volterra convolution equations*, SIAM J. Sci. Stat. Comput. **6** (1985), 532–541.

[71] L. Halpern and J. Rauch, *Absorbing boundary conditions for diffusion equations*, Numer. Math. **71** (1995), 185–224.

[72] H. Han and Z. Huang, *Exact artificial boundary conditions for Schrödinger equation in $\mathcal{R}^2$*, Comm. Math. Sci. **2** (2004), 79–94.

[73] H. Han, J. Jin and X. Wu, *A Finite–Difference method for the one–dimensional time–dependent Schrödinger equation on unbounded domain*, Comput. Math. Appl. **50** (2005), 1345–1362.

[74] H. Han, D. Yin and Z. Huang *Numerical solutions of Schrödinger equations in $\mathbb{R}^3$*, Numer. Meth. Partial Diff. Eqs. **23** (2006), 511–533.

[75] J.R. Hellums and W.R. Frensley, *Non–Markovian open–system boundary conditions for the time–dependent Schrödinger equation*, Phys. Rev. B **49** (1994), 2904–2906.

[76] T. Hohage, F. Schmidt, and L. Zschiedrich. Solving time-harmonic scattering problems based on the pole condition I: Theory. *SIAM J. Math. Anal.*, 35(1):183–210, 2003.

[77] S. Jiang, *Fast Evaluation of the Nonreflecting Boundary Conditions for the Schrödinger Equation*, Ph.D. thesis, Courant Institute of Mathematical Sciences, New York University, 2001.

[78] S. Jiang and L. Greengard, *Fast evaluation of nonreflecting boundary conditions for the Schrödinger equation in one dimension*, Comp. Math. Appl. **47** (2004), 955–966.

[79] S. Jiang and L. Greengard, *Efficient representation of nonreflecting boundary conditions for the time-dependent Schrödinger equation in two dimensions*, Comm. Pure Appl. Math. **61** (2007), 261–288.

[80] R. Kechroud, X. Antoine and A. Soulaïmani, *Numerical accuracy of a Padé-type non–reflecting boundary condition for the finite element solution of acoustic scattering problems at high–frequency*, Int. J. Numer. Methods Eng. **64** (2005), 1275–1302.

[81] R. Kosloff and D. Kosloff, *Absorbing boundaries for wave propagation problems*, J. Comput. Phys. **63** (1986), 363–376.

[82] J.-P. Kuska, *Absorbing boundary conditions for the Schrödinger equation on finite intervals*, Phys. Rev. B **46** (1992), 5000–5003.

[83] F. Ladouceur, *Boundaryless beam propagation*, Opt. Lett. **21** (1996), 4–5.

[84] R. Lascar, *Propagation des singularités des solutions d'équations pseudo–différentielles quasi-homogènes*, Ann. Inst. Fourier (Grenoble) **27** (1977), 79–123.

[85] M.F. Levy, *Non–local boundary conditions for radiowave propagation*, in: Third International Conference on Mathematical and Numerical Aspects of Wave Propagation Phenomena, Juan-les-Pins, France, 24-28 April 1995.

[86] M.F. Levy, *Transparent Boundary Conditions for Parabolic Equation Solutions of Radiowave Propagation Problems*, IEEE Trans. Antennas Propag. **45** (1997), 66–72.

[87] M.F. Levy, *Parabolic equation models for electromagnetic wave propagation*, IEE Electromagnetic Waves Series 45, 2000.

[88] M.F. Levy, *Perfectly matched layer truncation for parabolic wave equation models*, Proc. Roy. Soc.

Lond. A **457** (2001), 2609–2624.

[89] E.F. Lindmann, *Free-space boundary conditions for the time dependent wave equation*, J. Comput. Phys. **18** (1985), 16–78.

[90] M. López-Fernández, C. Palencia, and A. Schädle, *A spectral order method for inverting sectorial Laplace transforms*, SIAM J. Numer. Anal., 44 (2006), 1332–1350.

[91] C. Lubich, *Convolution quadrature and discretized operational calculus. I*, Numer. Math. **52** (1988), 129–145.

[92] C. Lubich, *Convolution quadrature and discretized operational calculus. II*, Numer. Math. **52** (1988), 413–425.

[93] C. Lubich and A. Schädle, *Fast convolution for non–reflecting boundary conditions*, SIAM J. Sci. Comput. **24** (2002), 161–182.

[94] A. Majda, and S. Osher, *Reflection of singularities at the boundary*, Comm. Pure Appl. Math. **28** (1975), 479–499.

[95] C.W. McCurdy, D.A. Homer and T.N. Resigno, *Time dependent approach to collisional ionization using exterior complex scaling*, Phys. Rev. A **65** (2002), 042714.

[96] B. Mayfield, *Non–local boundary conditions for the Schrödinger equation*, Ph.D. thesis, University of Rhode Island, Providence, RI, 1989.

[97] F.A. Milinazzo, C.A. Zala and G.H. Brooke, *Rational square–root approximations for parabolic equation algorithms*, J. Acoust. Soc. Am. **101** (1997), 760–766.

[98] C.A. Moyer, *Numerov extension of transparent boundary conditions for the Schrödinger equation in one dimension*, Amer. J. Phys. **72** (2004), 351–358.

[99] J.S. Papadakis, *Impedance formulation of the bottom boundary condition for the parabolic equation model in underwater acoustics*, NORDA Parabolic Equation Workshop, NORDA Tech. Note 143, 1982.

[100] J.S. Papadakis, *Exact nonreflecting Boundary Conditions for parabolic–type approximations in underwater acoustics* J. Comput. Acoust. **2** (1994), 83–98.

[101] J.S. Papadakis and E.T. Flouri, *A Neumann to Dirichlet map for the bottom boundary of a stratified sub–bottom region in parabolic approximation*, accepted for publication: J. Comput. Acoust.

[102] A. Pazy, *Semigroups of Linear Operators and Applications to Partial Differential Equations*, Springer, New York 1983.

[103] I. Podlubny, *Fractional differential equations. An introduction to fractional derivatives, fractional differential equations, to methods of their solution and some of their applications.* Mathematics in Science and Engineering, 198. Academic Press, Inc., San Diego, CA, 1999.

[104] M. Reed and B. Simon, *Methods of Modern Mathematical Physics II: Fourier Analysis, Self-adjointness*, Academic Press, San Diego 1975.

[105] L.F. Register, U. Ravaioli and K. Hess, *Numerical simulation of mesoscopic system with open boundaries using multidimensional time–dependent Schrödinger Equation*, J. Appl. Phys. **69** (1991), 7153–7158.

[106] D. Ruprecht, A. Schädle, F. Schmidt and L. Zschiedrich, *Transparent boundary conditions for time–dependent problems*, ZIB–Report 07–12, ZIB Berlin, May 2007. Note: accepted for publication in SIAM J. Sci. Comput.

[107] D. Ruprecht, A. Schädle, F. Schmidt, *Transparent boundary conditions – the pole condition approach*, Proceedings of Waves 2007, N. Biggs et.al. eds., 301-303, 2007.

[108] A. Schädle, *Numerische Behandlung transparenter Randbedingungen für die Schrödinger–Gleichung*, Masters Thesis, Universität Tübingen, 1998.

[109] A. Schädle, *Non–reflecting boundary conditions for the two dimensional Schrödinger equation*, Wave Motion **35** (2002), 181–188.

[110] A. Schädle, *Ein schneller Faltungsalgorithmus für nichtreflektierende Rand-bedingungen*, Ph.D. Thesis, Universität Tübingen, 2002.

[111] A. Schädle, L. Zschiedrich, S. Burger, R. Klose and F. Schmidt, *Domain Decomposition Method for Maxwell's Equations: Scattering of Periodic Structures*, J. Comput. Phys. **226** (2007), 477–493.

[112] F. Schmidt and P. Deuflhard, *Discrete transparent boundary conditions for the numerical solution of Fresnel's equation*, Comput. Math. Appl. **29** (1995), 53–76.

[113] F. Schmidt and D. Yevick, *Discrete transparent boundary conditions for Schrödinger–type equations*, J. Comput. Phys. **134** (1997), 96–107.

[114] F. Schmidt, *Construction of discrete transparent boundary conditions for Schrödinger–type equations*, Surv. Math. Ind. **9** (1999), 87–100.

[115] F. Schmidt, *A New Approach to Coupled Interior–Exterior Helmholtz–Type Problems: Theory and Algorithms*, Habilitation, Freie Universität Berlin, 2002.

[116] M. Schulte, *Transparente Randbedingungen für die Schrödinger Gleichung*, Diploma Thesis, Westfälische Wilhelms-Universität Münster, 2004.

[117] M. Schulte, A. Arnold, *Discrete transparent boundary conditions for the Schrödinger equation – a compact higher order scheme*, Kinetic and Related Models **1** (2008), 101–125.

[118] T. Shibata, *Absorbing boundary conditions for the finite–difference time–domain calculation of the one–dimensional Schrödinger equation*, Phys. Rev. B **43** (1991), 6760–6763.

[119] A. Soffer, C. Stucchio, *Absorbing boundaries for the nonlinear Schrödinger equation*, J. Comput. Phys. **225** (2007), 1218–1232.

[120] I.L. Sofronov, *Conditions for complete transparency on the sphere for the three–dimensional wave equation*, Russian Acad. Sci. Dokl. Math. **46** (1993), 397–401.

[121] I.L. Sofronov, *Artificial boundary conditions of absolute transparency for two- and three-dimensional external time–dependent scattering problems*, Euro. J. Appl. Math. **9** (1998), 561–588.

[122] I.L. Sofronov, *Non–reflecting inflow and outflow in wind tunnel for transonic time–accurate simulation*, J. Math. Anal. Appl. **221** (1998), 92–115.

[123] C. Sulem and P.-L. Sulem, *The nonlinear Schrödinger equation*, Applied mathematical sciences **139**, Springer, 1999.

[124] Z.-Z. Sun and X. Wu. *The stability and convergence of a difference scheme for the Schrödinger equation on an infinite domain by using artificial boundary conditions*, J. Comput. Phys. **214** (2006), 209–223.

[125] J. Szeftel, *Calcul Pseudodifférentiel et Paradifférentiel pour l'Etude de Conditions aux Limites Absorbantes et de Propriétés Qualitatives d'Equations aux Dérivées Partielles Non Linéaires*, Ph.D. Thesis, Université Paris, 2004.

[126] J. Szeftel, *Design of absorbing boundary conditions for Schrödinger equations in $\mathcal{R}^d$*, SIAM J. Numer. Anal. **42** (2004), 1527–1551.

[127] J. Szeftel, *Absorbing boundary conditions for one-dimensional nonlinear Schrödinger equations*, Numer. Math. **104** (2006), 103–127.

[128] J. Szeftel, *Absorbing boundary conditions for nonlinear scalar partial differential equations*, Comput. Methods Appl. Mech. Engrg. **195** (2006), 3760–3775.

[129] F.D. Tappert, *The parabolic approximation method*, in *Wave Propagation and Underwater Acoustics*, Lecture Notes in Physics 70, eds. J.B. Keller and J.S. Papadakis, Springer, New York, 1977, pp. 224–287.

[130] S.V. Tsynkov, *Numerical solution of problems on unbounded domains. A review*, Appl. Numer. Math. **27** (1998), 465–532.

[131] D. Yevick, T. Friese and F. Schmidt, *A comparison of transparent boundary conditions for the Fresnel equation*, J. Comput. Phys. **168** (2001), 433–444.

[132] C. Zheng, *Exact nonreflecting boundary conditions for one–dimensional cubic nonlinear Schrödinger equations*, J. Comput. Phys. **215** (2006), 552–565.

[133] C. Zheng, *A perfectly matched layer approach to the nonlinear Schrödinger wave equations*, J. Comput. Phys. **227** (2007), 537–556.

[134] C. Zheng, *An exact absorbing boundary conditions for the Schrödinger equation with sinusoidal potentials at infinity*, Commun. Comput. Phys. **3** (2008), 641–658.

[135] A. Zisowsky, *Discrete Transparent Boundary Conditions for Systems of Evolution Equations*, Ph.D. Thesis, Technische Universität Berlin, 2003.

[136] A. Zisowsky and M. Ehrhardt, *Discrete artificial boundary conditions for nonlinear Schrödinger equations*, Math. Comput. Modell. **47** (2008), 1264–1283.

[137] L. Zschiedrich, S. Burger, B. Kettner and F. Schmidt, *Advanced Finite Element Method for Nano–Resonators*, in: Physics and Simulation of Optoelectronic Devices XIV, M. Osinski, F. Henneberger and Y. Arakawa (eds), Proc. SPIE, **6115** (2006), 164–174.